

Propagation and Overturning of Localized Anelastic Internal Gravity Wavepackets

by

Alain Daniel Gervais

A thesis submitted in partial fulfillment of the requirements for the degree of

Master of Science

in

APPLIED MATHEMATICS

Department of Mathematical and Statistical Sciences
University of Alberta

© Alain Daniel Gervais, 2018

Abstract

As internal gravity wavepackets propagate upward in the atmosphere, their amplitude experiences exponential growth so that nonlinear effects influence their evolution. This thesis examines the weakly and fully nonlinear evolution, stability, and overturning of horizontally and vertically localized internal gravity wavepackets propagating in a stationary, non-rotating anelastic model atmosphere. The weakly nonlinear evolution is examined through the derivation of an expression for the flow induced by the propagating wavepacket, which is used to formulate a nonlinear Schrödinger equation. The induced flow is manifest as a long, hydrostatic disturbance qualitatively resembling a bow wake. The direction of this flow transitions from positive on the leading flank of the wavepacket to negative on the trailing flank. As such, we find that two-dimensional internal gravity wavepackets are always modulationally unstable. Consequently, enhanced amplitude growth is focused either on the leading or the trailing flank of the wavepacket. When combined with exponential amplitude growth predicted by linear theory, we anticipate that two-dimensional wavepackets will overturn either somewhat below or just above the overturning heights predicted by linear theory. The nonlinear Schrödinger equation is solved numerically, and its solutions are compared with the results of fully nonlinear simulations of the equations of motion to establish the validity of weakly nonlinear theory. Actual wave overturning heights are determined quantitatively from a range of fully nonlinear simulations.

Dedication

To Mamie, the strongest proponent for education I have ever known, who always took an interest in my research, and who optimistically requested a copy of this thesis knowing she would not be able read it before her passing.

Acknowledgments

First of all, I want to thank my parents, Paul and Joanne, who are my biggest supporters: for supporting my decision to pursue graduate studies, and for letting me live at home like a freeloader “as long as you’re a student”. I want to thank them and the rest of my family for their patience and understanding on those days when I was too busy with school work or research to spend time with them.

I would not have gotten far without the support of my supervisors. To Gordon, thank you for your infectious enthusiasm and love of applied PDEs that made me want to pursue my MSc in the first place; to Bruce, thank you for your patient guidance, and for praising my successes while helping me learn and grow from the challenges along the way. Thank you to the other members of the supervisory and examining committees for your time and interest in my research. The U of A is fortunate to have such excellent professors.

I want to thank Evan, one of my best bros since high school: back then it was a race to graduate with over 200 credits, if mostly for the bragging rights, but look at us now – finishing our masters and moving on to our PhDs. Oh and thanks for the coffee, beer, and perhaps too frequent supper hang-outs on Whyte Ave, or wherever the good food happened to be.

To my office mates Prachi and Curtis, thank you for your encouragement, advice, and for sharing your experiences as grad students when I was new at the whole grad school thing. Finally, thank you to everyone else who has had a positive impact on me over the past several years as a grad student and as an undergrad, all of whom have contributed to my success in some way (especially Jenn, Brian, and David from EAS).

This research was supported by the Natural Sciences and Engineering Research Council of Canada (NSERC).

Contents

List of Tables	vii
List of Figures	viii
1 Introduction	1
1.1 Motivation	1
1.2 Background	4
1.2.1 Some Introductory Concepts in Wave Theory	4
1.2.2 Review of Previous Research	5
2 Weakly Nonlinear Theory	12
2.1 Governing Equations	12
2.2 Wave-Induced Mean Flow	14
2.3 Schrödinger Equation for a Boussinesq Gas	23
2.4 Schrödinger Equation for an Anelastic Gas	28
3 Numerics	36
3.1 Fully Nonlinear Anelastic Solver	37
3.1.1 Discretization and Grid Generation	37
3.1.2 Initialization	38
3.1.2.1 Wave-Induced Mean Flow	39
3.1.3 Advection and Temporal Advancement	40
3.2 Weakly Nonlinear Anelastic Solver	42
3.2.1 Grid Generation	42

3.2.2	Initialization	43
3.2.3	Spatial and Temporal Advancement	43
3.2.4	Computation of the Wave-Induced Mean Flow	44
3.3	Quantitative Analysis Methods	45
4	Results and Comparison	48
4.1	Weakly Nonlinear Simulations	48
4.1.1	Effect of Oblique Dispersion Terms	56
4.1.2	Wave-Induced Mean Flow	58
4.1.3	Effect of Changing σ_x and H_ρ	62
4.2	Fully Nonlinear Simulations	66
4.2.1	Wave-Induced Mean Flow	68
4.3	Overturning Heights	75
5	Discussion and Conclusion	78
	Bibliography	82
A	Residue Theory Details	87
A.1	Problem Set-Up and Integration	87
A.2	Proof of Vanishing Arcs	92
A.3	Example: Bivariate Gaussian Amplitude Function	94
B	Derivation of the Transition Vertical Wavenumber	96
C	Discretization of Partial Derivatives	99

List of Tables

2.1	Polarization relations	17
2.2	Dispersion relation and its derivatives: Boussinesq gas	27
2.3	Dispersion relation and its derivatives: anelastic gas	33
3.1	Nondimensional coefficient values for the weakly nonlinear simulations	44

List of Figures

2.1	Illustrations of the wave-induced momentum field and vertical profiles	22
4.1	Snapshots of a weakly nonlinear wavepacket: $m = -0.4k$	49
4.2	Snapshots of a weakly nonlinear wavepacket: $m = -0.7k$	52
4.3	Snapshots of a weakly nonlinear wavepacket: $m = -1.4k$	54
4.4	Comparison: solutions of the nonlinear Schrödinger equation with and without oblique dispersion	57
4.5	Time series of the density-scaled wave-induced mean flow from weakly nonlinear simulations: $\sigma_x = 10k^{-1}$	59
4.6	Time series of the relative wave-induced momentum from weakly nonlinear simulations	61
4.7	Time series of the density-scaled wave-induced mean flow from weakly nonlinear simulations: $\sigma_x = 40k^{-1}$	63
4.8	Time series of the relative wave-induced momentum from weakly nonlinear simulations: comparison of $\sigma_x = 10k^{-1}$ and $\sigma_x = 40k^{-1}$	64
4.9	Time series of the relative wave-induced momentum from weakly nonlinear simulations: comparison of $\sigma_x = 10k^{-1}$ and $\sigma_x = 40k^{-1}$ with $H_\rho = 5k^{-1}$	65
4.10	Comparison: vertical displacement fields from weakly and fully nonlinear simulations	67
4.11	Comparison: weakly and fully nonlinear time series of the wave-induced mean flow for $\sigma_x = 10k^{-1}$	69

4.12 Comparison: weakly and fully nonlinear time series of the wave-induced mean flow for $\sigma_x = 40k^{-1}$	71
4.13 Summary of relative wave-induced momentum profiles with $H_\rho = 10k^{-1}$	72
4.14 Summary of relative wave-induced momentum profiles with $H_\rho = 5k^{-1}$	74
4.15 Overturning heights	76

Chapter 1

Introduction

1.1 Motivation

A (stably) stratified fluid is a fluid whose effective density decreases vertically. If the change is continuous, the fluid is called a continuously stratified fluid. Examples of stratified fluids include a liquid such as the ocean and a gas such as the atmosphere. In the ocean, the density depends primarily on the salinity and temperature, so that relatively warmer, fresher water overlies colder and more saline water. The density variations in the ocean are very small in comparison with the mean density (Vallis, 2006). Therefore, when considering such a fluid, it is common to apply the Boussinesq approximation in the equations of fluid motion, in which background density is treated as constant, except where it appears in the buoyancy term in the vertical momentum equation.

In the atmosphere, background pressure and density are greatest near sea level, and decrease to zero where the atmosphere transitions to outer space. The atmosphere is subdivided into layers, each characterized by its vertical temperature profile, with the boundaries between layers being approximately located where the temperature transitions from decreasing to increasing with height, or vice-versa. From the surface to approximately 10 km, the temperature decreases with height. Despite this, the colder fluid aloft does not necessarily descend so as to underlie warmer fluid, as in the ocean. This is due to compressibility: if cold air were to descend, higher pressure would compress the air and hence increase its temperature, assuming the entropy associated with the descending air is constant. Such a process is termed adiabatic, which means the warming is due to the mechanical energy of compression being

converted to thermal energy without loss to the environment. Likewise, if this process occurs in reverse, air rises adiabatically, and the resultant cooling is caused by expansion. An appropriate description of atmospheric stratification must take these thermodynamics into account. In particular, atmospheric stratification is conveniently described by the potential temperature, which is the temperature dry air would have if brought adiabatically to some reference pressure (Holton and Hakim, 2013). As such, in a stably stratified atmosphere, the potential temperature increases with height.

The basic behaviour of oscillations in stratified fluids is conceptualized with parcel theory. A parcel is a hypothetical fixed mass of fluid (whose volume is not necessarily constant). A vertically displaced fluid parcel will experience a buoyant restoring force that acts to return the parcel to its initial undisturbed (equilibrium) position. This concept is straightforwardly illustrated by considering, for example, a fluid parcel displaced upward from its initial position on an otherwise motionless water surface overlain by air: being surrounded by less dense fluid upon being displaced, gravity forces the parcel to descend toward its initial position. However, the parcel, having mass and therefore momentum, overshoots its equilibrium position at the water-air interface. Buoyancy forces then cause the parcel to rise again, and so on. This oscillation is referred to as a surface gravity wave (e.g. see Sutherland, 2010). When such a phenomenon occurs within a continuously stratified fluid, as opposed to on a fluid surface, the resulting oscillation is called an internal gravity wave. The natural frequency of the oscillation is called the buoyancy frequency (or Brunt-Väisälä frequency), and is denoted by N . An important qualitative difference between surface and internal gravity waves is that the latter are not restricted to propagate along the surface of constant effective density from which they originate.

Internal gravity waves propagate both horizontally and vertically within stratified fluids. In particular, upward-propagating waves in the atmosphere are of interest because they transport momentum upward (Holton and Hakim, 2013; Sutherland, 2010). As they propagate vertically within the atmosphere, their amplitude experiences exponential growth due to momentum conservation, owing to the atmosphere's approximately exponentially decreasing background density (Eliassen and Palm, 1961; Bretherton, 1966). Because the background density varies greatly over the total depth of the atmosphere, the Boussinesq approximation can be applied

only to small vertical scales over which waves can propagate (Dutton and Fichtl, 1969). The limitations imposed by this restriction motivated the development of several so-called anelastic approximations, the simplest of which—and that used in this thesis—is that of Ogura and Phillips (1962). This approximation models the exponential amplitude growth with height experienced by the waves, while also filtering sound waves from the equations of motion. (See Klein (2009) for a discussion and comparison of select anelastic-type models). Throughout this thesis, the exponential growth of waves with height will be referred to as “anelastic growth”. Once the wave amplitude becomes sufficiently large, the waves begin to overturn, meaning the waves carry denser fluid over less dense fluid. As the waves continue to propagate upward, overturning continues and the waves can eventually convectively break, thus irreversibly depositing their momentum to the ambient fluid (McFarlane, 1987).

One ongoing challenge is to incorporate the effects of momentum deposition by wave breaking into atmospheric general circulation models. Because internal gravity waves typically exist on too small a scale to be explicitly resolved by such models, it is necessary to apply parameterization schemes, which attempt to predict the effect of the breaking waves using only explicitly resolved variables (Holton and Hakim, 2013). Lindzen (1981) proposed that wave breaking generates turbulence that prevents further anelastic growth as the waves continue propagating vertically. It was anticipated that waves would thereafter continuously deposit their momentum in a layer approximately bounded below by their breaking height and bounded above by their critical level, which is the height at which the wave’s horizontal propagation speed is equal to the mean zonal (eastward) atmospheric wind. In particular, this approach used linear theory to estimate the wave breaking heights. Based on Lindzen’s conclusions, so-called gravity wave drag schemes were implemented in several general circulation models (Palmer et al., 1986; McFarlane, 1987; Scinocca and McFarlane, 2000). Their inclusion led to predictions of mean zonal winds and temperatures in the middle atmosphere that more closely resembled observations (McLandress, 1998).

Even if a wave has small amplitude initially, before reaching an overturning amplitude the wave may nonetheless grow to such an amplitude that linear theory ceases to predict its evolution correctly. The process of wave breaking is itself nonlinear. As such, Dosser and Sutherland (2011) (henceforth DS11) questioned whether it was appropriate to use linear

theory for the development of gravity wave drag schemes. In their study of one-dimensional (horizontally periodic, vertically localized, and spanwise-uniform) wavepackets, DS11 found that weakly nonlinear effects significantly altered wave breaking heights. Depending on the wavepacket’s initial frequency, the waves grew to overturning amplitudes and broke either well above or well below the heights predicted by linear theory.

In order eventually to improve gravity wave drag schemes, it is necessary to gain a more complete understanding of the processes that ultimately cause waves to grow to overturning amplitudes. The motivation behind the research presented herein is to understand the weakly nonlinear effects that dominate the evolution and overturning heights of two-dimensional (horizontally and vertically localized, and spanwise-uniform) anelastic wavepackets. As a non-trivial extension of the work of DS11, in this thesis the weakly and fully nonlinear dynamics of two-dimensional wavepackets is investigated. In particular, this is done through the derivation of weakly nonlinear equations, and the comparison of their numerical solutions with the results of fully nonlinear simulations. In doing so, the validity of weakly nonlinear theory is assessed.

1.2 Background

1.2.1 Some Introductory Concepts in Wave Theory

Much research on vertically propagating atmospheric internal gravity waves has focused on either monochromatic waves or horizontally periodic, vertically localized wavepackets. To facilitate the discussion throughout this thesis, here we briefly introduce these and key related concepts more formally. A monochromatic (plane) wave, whose structure is denoted by η , is conveniently expressed as a complex exponential

$$\eta(\mathbf{x}, t) = A_0 e^{i(\mathbf{k} \cdot \mathbf{x} - \omega t)}, \quad (1.1)$$

in which $A_0 \in \mathbb{C}$ is a constant that encodes the amplitude and phase of the wave, and η is understood to be the real part of the right-hand side expression. The one-, two-, or three-dimensional vector \mathbf{k} contains the wavenumbers in the x - and/or y - and/or z -directions. The wavenumber in any given direction is 2π divided by the wavelength in that direction. In this thesis, the wavenumber vector will always be $\mathbf{k} = (k, m) = 2\pi(\lambda_x^{-1}, \lambda_z^{-1})$, in which λ_x and

λ_x and λ_z are the wavelengths in the x - and z -directions, respectively. In (1.1), $\omega = \omega(\mathbf{k}) > 0$ is the frequency of the waves, which is conventionally taken to be positive to ensure the waves are forward-propagating in time. The expression for ω is given by the dispersion relation, which relates the wave's frequency to its wavenumber. From the dispersion relation are derived two important wave quantities: the phase velocity, $\mathbf{c}_p = (c_{p_x}, c_{p_z})$, whose components are the speed of propagation of points of constant phase in the x - and z -directions, respectively; and the group velocity, $\mathbf{c}_g = (c_{g_x}, c_{g_z})$, whose components are the speed at which the wave's energy is transported in the x - and z -directions, respectively. The phase and group velocities, respectively, are found using

$$\mathbf{c}_p = \frac{\omega}{|\mathbf{k}|^2} \mathbf{k} \quad \text{and} \quad \mathbf{c}_g = \left(\frac{\partial \omega}{\partial k_x}, \frac{\partial \omega}{\partial k_z} \right). \quad (1.2a,b)$$

Explicit expressions for the dispersion relation and group velocity are provided in Chapter 2.

Alternatively, quasi-monochromatic wavepackets are localized in one-, two-, or three dimensions, and their structure is expressed as

$$\eta(\mathbf{x}, t) = A_\eta(\mathbf{x}, t) e^{i(\mathbf{k} \cdot \mathbf{x} - \omega t)}, \quad (1.3)$$

in which the amplitude envelope function, $A_\eta : \mathbb{R}^2 \times \mathbb{R} \rightarrow \mathbb{C}$, describes the amplitude envelope of the waves. In this thesis examining two-dimensional wavepackets, the amplitude function depends spatially on x and z alone. In (1.3) as in (1.1), η is understood to be the real part of the right-hand side expression. As is the case for monochromatic waves, the phase and group velocities for waves within the wavepackets are likewise defined using (1.2a) and (1.2b), respectively. For wavepackets, the group velocity corresponds to the propagation speed and direction of the wavepacket.

1.2.2 Review of Previous Research

Many numerical studies have tended to focus on interactions between the waves and an existing background flow. In the first numerical study of its kind, Jones and Houghton (1971) found that the background flow, through momentum coupling with an upward-propagating wave, could be accelerated by wave breaking, hence modifying the critical level height, where the horizontal phase speed of the waves matched the background flow speed. Incorporating

the effects of background wind shear into a critical level-internal wave interaction model, Grimshaw (1975) found that small and large amplitude waves behaved qualitatively differently. In particular, waves with small initial amplitude narrowed and grew in maximum amplitude while approaching a critical level, dissipating thereafter. Conversely, initially large amplitude waves remained broad, grew to a smaller maximum amplitude than the initially small amplitude waves, and dissipated less rapidly after interacting with their critical level, compared to the initially small amplitude waves. For both initially small and initially large amplitude waves, decay resulted in a transfer of energy and momentum to the mean flow.

Fritts (1982) performed quasi-linear simulations of vertically propagating internal gravity waves generated from a shear layer. It was found that, by extracting energy from, then transporting energy through the shear layer, waves could significantly accelerate the mean flow above and below the shear layer.

Dunkerton (1981) found that linear, slowly varying, topographically forced waves in an anelastic atmosphere could spontaneously form descending regions of strong wind shear. Conversely, evolving self-acceleration effects were found by Fritts and Dunkerton (1984) to cause quasi-linear wavepackets to Doppler-shift their frequency to such an extent that the wavepacket could propagate well above its original critical level. Furthermore, Fritts and Dunkerton found qualitative differences between small and large amplitude wavepackets. In particular, the relatively smaller degree of self-acceleration and rate of vertical propagation near the wave front of the small amplitude wavepacket at early times caused the long-time evolution to proceed more slowly than their larger amplitude counterparts.

Even in the absence of pre-existing background flow, finite-amplitude internal gravity wavepackets induce a time-evolving mean flow as they propagate. This is analogous to the Stokes drift induced by surface waves on deep water. The Stokes drift is an order amplitude-squared correction to the horizontal velocity field that causes fluid parcels to advect further forward upon passage of a wave crest than backward upon passage of a trough. Hence there is a net movement of fluid in the direction of wave propagation (Stokes, 1847; Kundu et al., 2016).

Interactions between internal gravity waves and their induced flow have been shown to be the dominant mechanism governing the weakly nonlinear evolution of one-dimensional Boussinesq wavepackets (Sutherland, 2006a,b). An explicit equation for the mean flow, U_{1D} ,

induced by one-dimensional Boussinesq wavepackets, derived from the principle of wave action, has been known since Acheson (1976). (Wave action is a conserved analogue to wave energy, which is not conserved when background shear is present). Alternatively, Sutherland (2010) used conservation of momentum for quasi-monochromatic wavepackets to show that

$$U_{\text{1D}} = u_{\text{DF}} = \frac{\langle uw \rangle}{c_{gz}} = \frac{1}{2} N |\mathbf{k}| |A|^2. \quad (1.4)$$

Here, $\langle \cdot \rangle$ denotes the horizontal average over a period, u and w are the horizontal and vertical velocity fields of the waves, respectively, c_{gz} is the vertical group speed of the wavepacket, N is the buoyancy frequency, $\mathbf{k} = (k, m)$ is the wavenumber vector, and A is the vertical displacement amplitude, which depends on the vertical coordinate, z , and time, t , for one-dimensional waves. The subscript DF denotes that the wave-induced mean flow arises from the divergence of momentum flux per unit mass. The flow described by (1.4) is horizontally uniform, unidirectional, and vertically constrained to the vicinity of the amplitude envelope.

The corresponding expression for the flow induced by one-dimensional wavepackets in an anelastic gas was derived using Hamiltonian fluid mechanics by Scinocca and Shepherd (1992) and by DS11. Explicitly, the wave-induced mean flow (henceforth denoted by U with no subscripts) for one-dimensional wavepackets in an anelastic gas is given by

$$U = \frac{1}{2} N K |A|^2 e^{z/H_\rho}. \quad (1.5)$$

This differs in two ways from its Boussinesq counterpart, given by (1.4). The coefficient $K = (|\mathbf{k}|^2 + 1/4H_\rho^2)^{1/2}$ includes the anelastic correction term, $1/4H_\rho^2$, in which H_ρ is the density scale height or e -folding depth, which is the spatial distance over which the density decreases by a factor of e^{-1} . Also, the right-hand side of (1.5) contains the factor e^{z/H_ρ} , which models the anelastic growth with height experienced by the wave-induced mean flow as it translates vertically with the wavepacket into less dense ambient fluid.

For a two-dimensional (horizontally and vertically localized, and spanwise uniform) wavepacket, the amplitude envelope function depends on the horizontal coordinate, x , as well as on z and t . An explicit integral expression for the horizontal flow induced by two-dimensional wavepackets having Gaussian structure in the horizontal direction in a non-rotating Boussinesq fluid was derived by van den Bremer and Sutherland (2014) (henceforth vdBS14), and

is given by

$$u^{(2)}(\tilde{x}, \tilde{z}) = -\frac{1}{4}N \frac{km}{|\mathbf{k}|} \sigma_x \sigma_z \int_0^\infty \widehat{|A|^2} \mu^2 \sin(\mu \tilde{z} + \mu^2 c_{gz} |\tilde{x}|/N) d\mu. \quad (1.6)$$

Here, σ_x and σ_z are the horizontal and vertical extents, respectively, of the wavepacket; the caret denotes that $|A|^2$ is horizontally and vertically Fourier transformed; and $(\tilde{x}, \tilde{z}) = (x - c_{gx}t, z - c_{gz}t)$ are spatial coordinates in a frame of reference translating with the wavepacket at its group velocity. In the integrand of (1.6), the integration variable μ is the transform variable associated with z in Fourier space. The flow induced by a two-dimensional wavepacket in a Boussinesq fluid is qualitatively different than its one-dimensional counterpart, given by (1.4). Rather than being horizontally uniform and unidirectional, the two-dimensional horizontal induced flow, $u^{(2)}(\tilde{x}, \tilde{z})$, resembles a bow wake. Thus the induced flow is manifest as a long, hydrostatic wave, that propagates far horizontally and below an upward-propagating wavepacket. Crucially, in the flow described by (1.6), the flow direction changes sign from positive on the leading flank of the wavepacket to negative on the trailing flank, in agreement with the predictions of Bretherton (1969) (see also Akylas and Tabaei, 2005; Tabaei and Akylas, 2007).

A model describing the weakly nonlinear evolution of internal gravity wavepackets, as it depends upon the interactions between the waves and their induced mean flow, is the nonlinear Schrödinger equation. This partial differential equation describes the spatial and temporal evolution of the amplitude envelope of a moderately large amplitude wavepacket. The nonlinear Schrödinger equation for a one-dimensional wavepacket in a uniformly stratified (constant buoyancy frequency), non-rotating Boussinesq fluid with no background flow was derived by Akylas and Tabaei (2005). A special case, that furthermore explicitly includes the wavepacket's translation at its vertical group speed, was derived by Sutherland (2006b), and is given by

$$\partial_t A = -c_{gz} \partial_z A + i \frac{1}{2} \omega_{mm} \partial_{zz} A + \frac{1}{6} \omega_{mmm} \partial_{zzz} A - ikUA. \quad (1.7)$$

Here, $A = A(z, t)$ is the vertical displacement amplitude of the wavepacket, m is the vertical wavenumber, $c_{gz} = \partial\omega/\partial m$ is the vertical group speed, and $\omega_{mm} = \partial^2\omega/\partial m^2$ and $\omega_{mmm} = \partial^3\omega/\partial m^3$ are the constant coefficients respectively given by the second and third partial derivatives of the dispersion relation, $\omega = \omega(k, m)$, with respect to m . The rightmost term in

(1.7) is the nonlinear term, in which the wave-induced mean flow $U \propto |A|^2$ is given by (1.4). This describes the Doppler-shifting of the waves by the flow they induce. Numerical solutions of (1.7) showed that interactions between waves and their induced mean flow dominate the weakly nonlinear evolution of Boussinesq wavepackets.

The nonlinear Schrödinger equation corresponding to (1.7), but for one-dimensional wavepackets in an anelastic gas, was derived by DS11, and is given by

$$\partial_t A = -c_{gz} \partial_z A + i \frac{1}{2} \omega_{mm} \partial_{zz} A + \frac{1}{6} \partial_{mmm} A - ikUA + \frac{\omega^2}{2N^2 k H_\rho} (3mH_\rho - i)(\partial_z U)A, \quad (1.8)$$

in which U is the wave-induced mean flow, given by (1.5). Equation (1.8) describes the weakly nonlinear evolution of one-dimensional wavepackets in a uniformly stratified, non-rotating anelastic atmosphere. The primary difference between (1.8) and its Boussinesq counterpart (1.7) is the inclusion of the rightmost term that represents the interactions of the waves and the shear in their induced flow. Through numerical solutions of (1.8), DS11 concluded that the weakly nonlinear evolution of anelastic wavepackets is dominated by interactions between the waves and their induced mean flow.

In a study of three-dimensional wavepackets, Shrira (1981) derived a nonlinear Schrödinger equation for effectively two-dimensional Boussinesq wavepackets (not reproduced here, but elaborated on in §2.4). In particular, the nondimensionalization of the governing equations resulted in prescribing the relative order of magnitude of the nonlinear advection terms *a priori*. Separately, nonlinear Schrödinger equations for two- and three-dimensional wavepackets were derived by Akylas and Tabaei (2005) and Tabaei and Akylas (2007), respectively. However, relatively small amplitude waves were the focus of their numerically computed solutions.

Moderately large amplitude dispersive wavepackets exhibit the weakly nonlinear effects of modulational stability and instability, which cause the wavepackets either to broaden and decay in amplitude (modulational stability) or to narrow and grow in amplitude (modulational instability) at a faster rate than that predicted by linear theory. This instability arises in the solutions of the nonlinear Schrödinger equations for both Boussinesq and anelastic one-dimensional wavepackets due to interactions between the waves and their induced mean flow (Akylas and Tabaei, 2005; Sutherland, 2006b; Dosser and Sutherland, 2011). Whether in the Boussinesq or anelastic contexts, the wave-induced mean flow acts in a conceptually identical

manner: the frequency of the waves is Doppler-shifted by the induced flow, which results in a local change in vertical group speed, which in turn results in wave spreading (associated with modulational stability) or accumulation (associated with modulational instability). In particular, DS11 found that waves having initial frequency greater than that of waves with the fastest vertical group speed are modulationally unstable, and consequently, overturn at a height lower than that predicted by linear theory. Conversely, hydrostatic waves with frequency lower than that of waves with the fastest vertical group speed, are modulationally stable and propagate well beyond the height predicted by linear theory before overturning.

The key difference between the modulational stability properties of one- and two-dimensional Boussinesq waves is that two-dimensional wavepackets are always modulationally unstable. This result was first shown by Tabaei and Akylas (2007), who arrived at this result using a linear stability analysis. In this thesis we will show that this result extends to two-dimensional anelastic wavepackets and explore the consequences of modulational instability on the overturning heights of two-dimensional anelastic internal gravity wavepackets.

That a wavepacket is modulationally unstable is not sufficient to ensure that it will overturn. It is possible for such a wavepacket to exhibit the Fermi-Pasta-Ulam recurrence phenomenon (Fermi et al., 1974), in which an approximate equipartition of energy among the modes of vibration is followed by a return to the initial state. The first known documented observation of this phenomenon in the solution of the nonlinear Schrödinger equation in a hydrodynamic context was by Benjamin and Feir (1967) in their study of weakly nonlinear wavetrains on deep water (see also Lake et al., 1977). However, modulational stability and instability, arising through interactions between the waves and their induced mean flow, have emerged as the dominant mechanisms governing the weakly nonlinear evolution of one-dimensional wavepackets in a Boussinesq fluid (Sutherland, 2006a) and in an anelastic gas (DS11). In particular, DS11 credit the effects of higher-order linear and nonlinear dispersion, via the inclusion of third-order terms in their nonlinear Schrödinger equation, with preventing the onset of the Fermi-Pasta-Ulam recurrence. It is expected that, by similarly including higher-order terms in our nonlinear Schrödinger equation, modulational instability will likewise dominate the weakly nonlinear evolution of anelastic internal gravity wavepackets in two dimensions. This will be shown in the comparisons between the results of the weakly and

fully nonlinear simulations.

Even if a one-dimensional anelastic wavepacket evolves nonlinearly to the point of overturning, the actual turbulent process of wave breaking due to convective instability does not immediately occur (DS11). Where a wave overturns and advects denser fluid above less dense fluid, locally the fluid is negatively buoyant. Sutherland (2001) found that in such situations the oscillatory motion of a plane wave could restore stability to an unstable region if the wave’s period was shorter than the time scale for the growth of convective instability. The one-dimensional wavepackets studied by DS11 were eventually unable to stabilize the rapidly developing regions of intense negative buoyancy. Though not of primary interest, we will likewise show for two-dimensional wavepackets that there is a delay between wave overturning and breaking.

In Chapter 2 we first derive the expression for the horizontal flow induced by two-dimensional anelastic internal gravity wavepackets, analogous to (1.6). The nonlinear Schrödinger equation for two-dimensional wavepackets in a Boussinesq gas is then derived, followed immediately by the derivation of its anelastic counterpart. It is useful to derive the weakly nonlinear equations in this order, as the Boussinesq derivation will serve as a template for the anelastic derivation, and as a check on the algebra involved. The numerical methods used to solve the weakly and fully nonlinear anelastic equations are discussed in Chapter 3. The results of the weakly and fully nonlinear simulations are presented and compared in Chapter 4. Finally, in Chapter 5 we discuss the results with a particular emphasis on the discrepancies between the overturning heights recorded by our fully nonlinear simulations, the fully nonlinear simulations of one-dimensional anelastic wavepackets studied by DS11, and the overturning heights predicted by linear theory.¹

¹A condensed version of the work presented in Chapters 2, 3, 4, and 5 has been submitted to the Journal of the Atmospheric Sciences, and is currently under review: Gervais, A. D., G. E. Swaters, T. S. van den Bremer, and B. R. Sutherland. “Evolution and Stability of Two-Dimensional Anelastic Internal Gravity Wavepackets”.

Chapter 2

Weakly Nonlinear Theory

2.1 Governing Equations

The weakly nonlinear theory of two-dimensional (horizontally and vertically localized) internal gravity wavepackets in an anelastic gas involves the derivations of the nonlinear Schrödinger equations governing the evolution of a wavepacket amplitude envelope in first a Boussinesq then an anelastic gas. The former derivation will serve as a template for the latter and as a means of checking the algebra. The latter derivation will itself require the equation for the flow induced by the waves as they propagate. To enable the mathematical development of the weakly nonlinear theory, we first establish the starting point common to all of the derivations that follow.

The fully nonlinear, two-dimensional, non-rotating anelastic Euler equation for the conservation of momentum, including the buoyancy term (Ogura and Phillips, 1962; Lipps and Hemler, 1982), is given by

$$\frac{D\mathbf{u}}{Dt} = -\nabla\left(\frac{p}{\bar{\rho}}\right) + \frac{g}{\bar{\theta}}\theta\hat{\mathbf{e}}_z, \quad (2.1)$$

in which $\mathbf{u} = (u, w)$ is the velocity, p is the pressure, $\bar{\rho}$ is the background density, g is the acceleration due to gravity, and $\bar{\theta}$ and θ are the background and fluctuation potential temperatures, respectively. The operator $D/Dt = \partial_t + \mathbf{u} \cdot \nabla$ is the material derivative, and $\hat{\mathbf{e}}_z$ is the standard unit basis vector in the z -direction. Equation (2.1) states that the acceleration of a fluid is forced by horizontal and vertical pressure gradients and buoyancy.

Also included in the complete set of anelastic equations is a statement of conservation of

internal energy, expressed as

$$\frac{D\theta}{Dt} = -w \frac{d\bar{\theta}}{dz}, \quad (2.2)$$

in which the background potential temperature is defined by

$$\bar{\theta} = \bar{T} \left(\frac{\bar{p}}{p_0} \right)^{-\kappa}.$$

Here, \bar{T} is the background temperature, \bar{p} is the background pressure, p_0 is a reference pressure, and $\kappa \approx 2/7$. For simplicity we assume our model atmosphere is isothermal, that is, the ambient temperature $\bar{T} = T_0 = \theta_0$ is constant. Furthermore, we assume the background pressure and density decrease exponentially with height with an e -folding depth given by the density scale height. Explicitly, $H_\rho = -\bar{\rho}/(d\bar{\rho}/dz) = R_a T_0/g$, in which R_a is the ideal gas constant for dry air and the background density is

$$\bar{\rho} = \rho_0 e^{-z/H_\rho}. \quad (2.3)$$

The corresponding background potential temperature is

$$\bar{\theta} = \theta_0 e^{z/H_\theta}, \quad (2.4)$$

in which $H_\theta = H_\rho/\kappa$ is the potential temperature scale height. The squared buoyancy frequency is

$$N^2 = \frac{g}{\bar{\theta}} \frac{d\bar{\theta}}{dz} = \frac{g}{H_\theta}, \quad (2.5)$$

which is constant in our isothermal model atmosphere.

The final governing equation is the statement of mass conservation for an anelastic gas,

$$\nabla \cdot (\bar{\rho} \mathbf{u}) = 0. \quad (2.6)$$

Together, (2.1), (2.2), and (2.6) form the set of equations governing fluid motion in an anelastic gas. The condition given by (2.6) has the effect of filtering acoustic waves from the equations of motion. In addition to having negligible effect on wave dynamics on the physical scales of concern in this thesis, acoustic waves present numerical challenges due to their relatively fast propagation speed. By filtering such waves, numerically integrated solutions of the governing equations may use larger time steps while remaining numerically stable (Durrant, 2010).

The Boussinesq momentum equation is recovered from its anelastic counterpart by taking the so-called ‘‘Boussinesq limit’’ of (2.1). In this limit, the density scale height is allowed to become arbitrarily large. Taking $H_\rho \rightarrow \infty$ in (2.1) and (2.6) corresponds to setting the background density $\bar{\rho} \rightarrow \rho_0$ and potential temperature $\bar{\theta} \rightarrow \theta_0$ to constant characteristic values in the anelastic momentum and mass conservation equations, respectively, which yields

$$\rho_0 \frac{D\mathbf{u}}{Dt} = -\nabla p + g \frac{\rho_0}{\theta_0} \theta \hat{\mathbf{e}}_z; \quad (2.7)$$

$$\nabla \cdot \mathbf{u} = 0. \quad (2.8)$$

In the context of Boussinesq fluids, (2.8) is a consequence of the incompressibility condition. The Boussinesq internal energy equation remains identical to its anelastic counterpart, given by (2.2). The expression for squared buoyancy frequency also remains identical to its anelastic counterpart, given by (2.5).

2.2 Wave-Induced Mean Flow

The integral expression for the flow induced by two-dimensional Boussinesq internal gravity wavepackets, reproduced in (1.6), was derived by vdBS14. The extension of that work to waves in the model anelastic atmosphere described in the previous section is presented here and follows a similar approach as that of vdBS14. The governing equations for internal waves in an anelastic atmosphere are given by (2.1), (2.2), and (2.6). The first step is to re-cast the internal energy equation (2.2) in terms of vertical displacement ξ using the relation

$$\xi = -\theta/\bar{\theta}', \quad (2.9)$$

where $\bar{\theta}$ is the background potential temperature profile given by (2.4) and the prime denotes differentiation with respect to z . Rearranging (2.9) for fluctuation potential temperature and substituting the resulting expression into the internal energy equation (2.2) yields the equation for the evolution of vertical displacement,

$$\frac{D\xi}{Dt} = w - w\xi \frac{\bar{\theta}''}{\bar{\theta}'} \approx w. \quad (2.10)$$

The rightmost approximation holds assuming a mean potential temperature profile given by (2.4), which reveals that

$$\frac{\bar{\theta}''}{\bar{\theta}'} = \frac{\bar{\theta}}{H_\theta^2} \frac{H_\theta}{\bar{\theta}} = \frac{1}{H_\theta} \sim \frac{1}{10^5 \text{ m}},$$

using a typical value of H_θ for the atmosphere (Vallis, 2006). Hence the $w\xi(\bar{\theta}''/\bar{\theta}')$ term in (2.10) is found to be negligibly small.

The pressure terms are now eliminated by taking the curl of the momentum equation, the result of which is

$$\begin{aligned} \frac{D\zeta}{Dt} &= -\zeta(\nabla \cdot \mathbf{u}) - \frac{g}{\bar{\theta}} \partial_x \theta \\ &= -\zeta(\nabla \cdot \mathbf{u}) + N^2 \partial_x \xi. \end{aligned} \quad (2.11)$$

Here, $\zeta := (\partial_z u - \partial_x w) \cdot \hat{\mathbf{e}}_y$ is the spanwise vorticity, in which $\hat{\mathbf{e}}_y$ is the standard unit basis vector in the spanwise (y) direction, and the squared buoyancy frequency N^2 , given by (2.5), arises upon re-casting the potential temperature in terms of vertical displacement via (2.9). We combine the time derivative of (2.11) with the x -derivative of (2.10), and rearrange the result so that linear terms appear on the left-hand side and nonlinear terms appear on the right-hand side:

$$\partial_{tt}\zeta - N^2 \partial_x w = -\partial_t(\mathbf{u} \cdot \nabla \zeta) - N^2 \partial_x(\mathbf{u} \cdot \nabla \xi) - \partial_t(\zeta \nabla \cdot \mathbf{u}). \quad (2.12)$$

The mass-streamfunction, denoted by Ψ , is defined implicitly via (2.6) by the relations

$$u = -\frac{1}{\bar{\rho}} \partial_z \Psi \quad \text{and} \quad w = \frac{1}{\bar{\rho}} \partial_x \Psi. \quad (2.13\text{a,b})$$

Consequently, the spanwise vorticity is also expressed in terms of the mass-streamfunction as

$$\zeta = -\frac{1}{\bar{\rho}} \left[\nabla^2 \Psi + \frac{1}{H_\rho} \partial_z \Psi \right]. \quad (2.14)$$

Together, the relations (2.13a,b) and (2.14) allow us to express the left-hand side of (2.12) purely in terms of mass-streamfunction Ψ . After some manipulation the resulting partial differential equation is written as a linear operator \mathcal{L} acting on the mass-streamfunction on the left-hand side and the density-scaled divergence of a nonlinear vector \mathbf{F} on the right-hand

side, written explicitly as

$$\underbrace{\left[\partial_{tt} \left(\nabla^2 + \frac{1}{H_\rho} \partial_z \right) + N^2 \partial_{xx} \right]}_{:=\mathcal{L}} \Psi = \bar{\rho} \nabla \cdot \underbrace{\left[\partial_t(\mathbf{u}\zeta) + N^2 \partial_x(\mathbf{u}\xi) - \frac{N^2}{H_\rho} w \xi \hat{\mathbf{e}}_x \right]}_{:=\mathbf{F}}, \quad (2.15)$$

where $\hat{\mathbf{e}}_x$ is the standard unit basis vector in the x -direction. Together, equations (2.10) and (2.15) form the set of coupled equations governing ξ and Ψ . The set is closed by inclusion of the relations (2.13a,b) and (2.14).

In seeking a wave-like solution of (2.15), we first consider substituting into (2.15) a plane wave given in terms of the vertical displacement

$$\xi = A_0 e^{i\varphi + z/2H_\rho}, \quad (2.16)$$

where $\varphi = kx + mz - \omega t$ is the phase, the amplitude A_0 is constant, and the actual displacement is understood to be the real part of the right-hand side of (2.16). The remaining basic wave fields are given by the polarization relations in the centre column of Table 2.1. The expressions in the centre column of Table 2.1 are valid for plane waves (in which A is understood to be constant) and for quasi-monochromatic wavepackets (in which it is understood that $A = A(x, z, t)$). On the left-hand side of (2.15), derivatives with respect to time will manifest as factors of $-i\omega$, derivatives with respect to x will manifest as factors of ik , and derivatives with respect to z will manifest as factors of $im - \frac{1}{2H_\rho}$. Substituting a plane wave solution into the left-hand side of (2.15) together with the dispersion relation yields

$$\mathcal{L}\Psi \equiv 0.$$

Because we are interested in the mean forcing contributed by the divergence of \mathbf{F} , it is convenient to express (2.16) as

$$\xi = \frac{1}{2} A_0 e^{i\varphi + z/2H_\rho} + \text{c.c.},$$

in which we have explicitly included its complex conjugate, denoted by c.c., in order to compute the products on the right-hand side of (2.15). Taking the means of the products in \mathbf{F} amounts to retaining only terms in which $e^{\pm i2\varphi}$ does not appear. Computing the means reveals that $\overline{w\zeta} \equiv 0$ and $\overline{w\xi} \equiv 0$, a result of the fact that the vertical velocity is exactly 90°

Field (Amplitude)	$O(\alpha\epsilon^0)$	$O(\alpha\epsilon)$
Vertical displacement	$(A_\xi)_0^{(1)} = A$	$(A_\xi)_1^{(1)} = 0$
Mass-streamfunction	$(A_\Psi)_0^{(1)} = -\bar{\rho}\frac{\omega}{k}A$	$(A_\Psi)_1^{(1)} = -i\bar{\rho}\frac{N}{K^3}[kA_X + mA_Z]A$
Horizontal velocity	$(A_u)_0^{(1)} = \frac{\omega}{k}(im - \frac{1}{2H_\rho})A$	$(A_u)_1^{(1)} = \frac{N}{K^3}[ik(im - \frac{1}{2H_\rho})A_X + (K^2 - m^2 - \frac{im}{2H_\rho})AZ]$
Vertical velocity	$(A_w)_0^{(1)} = -i\omega A$	$(A_w)_1^{(1)} = \frac{N}{K^3}[(k^2 - K^2)A_X + kmA_Z]$
Vorticity	$(A_\zeta)_0^{(1)} = -NK A$	$(A_\zeta)_1^{(1)} = i\frac{N}{K}[kA_X + mA_Z]$

Table 2.1: Expressions for the amplitudes of various fields as they relate to the vertical displacement amplitude, at $O(\alpha\epsilon^0)$ (centre column) and at $O(\alpha\epsilon)$ (right column). The actual polarization relations are found by multiplying each amplitude function by $e^{i\varphi+z/2H_\rho}$, where $\varphi = kx + mz - \omega t$. In each expression, partial derivatives of A are denoted by subscripts, and $K = (k^2 + m^2 + 1/4H_\rho^2)^{1/2}$. If one considers a plane wave then A is constant and the polarization relations from linear theory are given by the centre column and all expressions in the right column are identically zero; if one considers a slowly varying two-dimensional wavepacket then $A = A(X, Z, T)$ in the centre and right columns.

out of phase with both the vorticity and the vertical displacement. Since A_0 is constant, the two (unique) remaining terms are

$$\overline{u\zeta} = \frac{1}{4} \frac{\omega}{k} \frac{NK}{H_\rho} A_0^2 e^{z/H_\rho} \quad \text{and} \quad \overline{u\xi} = -\frac{1}{4} \frac{\omega}{k} \frac{1}{H_\rho} A_0^2 e^{z/H_\rho}, \quad (2.17a,b)$$

which have retained functional dependence only on the vertical coordinate via the factor e^{z/H_ρ} . As such, substituting (2.17a,b) into \mathbf{F} readily shows that $\mathbf{F} = \mathbf{0}$. This is consistent with the fact that plane internal gravity waves are an exact solution to the fully nonlinear equations of motion, and that such waves do not induce a mean flow (Sutherland, 2010). We therefore pursue the following perturbation-theoretical approach to determine a solution in the form of a quasi-monochromatic wavepacket.

We first define “slow” variables in a frame of reference translating with the wavepacket at its horizontal and vertical group velocities:

$$X = \epsilon(x - c_{g_x}t), \quad Z = \epsilon(z - c_{g_z}t), \quad T = \epsilon^2t, \quad (2.18a,b,c)$$

in which $\epsilon = \epsilon_z = 1/(k\sigma_z) \approx \epsilon_x = 1/(k\sigma_x)$ is a nondimensional measure of inverse wavepacket extent, where we have set $\epsilon_x \approx \epsilon_z$ for simplicity.

Neglecting dispersion, that is, dependence on the variable T in the amplitude envelope function, we have at leading-order

$$\xi_0^{(1)} := A(X, Z)e^{i\varphi+z/2H_\rho},$$

where the superscript and subscript on $\xi_0^{(1)}$ denote the field's order in α and ϵ , respectively. Here, $\alpha = kA_0$ is a nondimensional measure of wavepacket amplitude. Substituting terms of $O(\alpha\epsilon^0)$, given in the centre column of Table 2.1, into the right-hand side of (2.15), we find that $\mathbf{F}_1^{(2)} = \mathbf{0}$ and hence $(\nabla \cdot \mathbf{F})_2^{(2)} = 0$ at this order. It is therefore necessary to include the first-order correction terms to the polarization relations in the right column of Table 2.1.

We write the perturbation expansions for each field as $\eta = \eta_0 + \epsilon\eta_1 + \epsilon^2\eta_2 + \dots$, where η is any wave field of interest. Furthermore, in order to close the set of polarization relations at first-order in ϵ it is necessary to impose the structure of one field. Somewhat arbitrarily, we impose the structure of the vertical displacement field, and so we set $\xi_n^{(1)} \equiv 0 \forall n \geq 1$. To obtain the remaining $O(\alpha\epsilon)$ fields we extract derivatives of the amplitude envelope function, noting that X - and Z -derivatives contribute one order in ϵ .

It is convenient to begin by finding the first-order correction to the mass-streamfunction using the relation $\partial_t \xi = w = \frac{1}{\rho} \partial_x \Psi$, the result of which is

$$- [c_{g_x} \partial_X A + c_{g_z} \partial_Z A] e^{i\varphi+z/2H\rho} = -\frac{\omega}{k} (\partial_X A) e^{i\varphi+z/2H\rho} + \frac{1}{\rho} ik \Psi_1. \quad (2.19)$$

Upon rearrangement and substitution of $c_{g_x} = N(K^2 - k^2)K^{-3}$ and $c_{g_z} = -NkmK^{-3}$ into (2.19) we find that

$$\Psi_1 = -i\bar{\rho} \frac{N}{K^3} [k\partial_X A + m\partial_Z A] e^{i\varphi+z/2H\rho}.$$

Now the remaining fields can be determined from

$$\Psi \approx \Psi_0 + \epsilon\Psi_1 = -\bar{\rho} \left[\frac{\omega}{k} A + i\epsilon \frac{N}{K^3} (k\partial_X A + m\partial_Z A) \right] e^{i\varphi+z/2H\rho}.$$

It is natural to proceed in determining u using (2.13a). Explicitly omitting the $O(\epsilon^2)$ terms arising from the second-order X - and Z -derivatives of the amplitude function, we have

$$u = -\frac{1}{\rho} \partial_z \Psi = \frac{\omega}{k} \left(im - \frac{1}{2H\rho} \right) A e^{i\varphi+z/2H\rho} + \epsilon \left[i \frac{Nk}{K^3} \left(im - \frac{1}{2H\rho} \right) \partial_X A + \left(i \frac{Nm}{K^3} \left(im - \frac{1}{2H\rho} \right) + \frac{\omega}{k} \right) \partial_Z A \right] e^{i\varphi+z/2H\rho}.$$

Similarly, we determine w using (2.13b). However, we retain the $O(\epsilon^2)$ terms for reasons that

will be made clear shortly. We find that

$$w = \frac{1}{\rho} \partial_x \Psi$$

$$= - \left\{ i\omega A + \epsilon \frac{N}{K^3} \left[(k^2 - K^2) \partial_X A + km \partial_Z A \right] + i\epsilon^2 \frac{N}{K^3} \left[k \partial_{XX} A + m \partial_{ZZ} A \right] \right\} e^{i\varphi + z/2H\rho}.$$

Having determined the expressions for u and w , we readily find that the expression for spanwise vorticity is

$$\zeta = \partial_z u - \partial_x w = \left[-NKA + \epsilon i \frac{N}{K} (k \partial_X A + m \partial_Z A) \right] e^{i\varphi + z/2H\rho},$$

where we have again explicitly omitted the $O(\epsilon^2)$ terms. We recover $u_0^{(1)}$, $w_0^{(1)}$, and $\zeta_0^{(1)}$ directly from the $O(\epsilon^0)$ parts of their respective perturbation expansions. Likewise $u_1^{(1)}$, $w_1^{(1)}$, and $\zeta_1^{(1)}$ are given by the $O(\epsilon)$ parts. The resulting $O(\alpha\epsilon)$ polarization relations are summarized in the right column of Table 2.1. The averages of the $O(\alpha^2\epsilon)$ fields are found by taking the product of the $O(\alpha\epsilon^0)$ and $O(\alpha\epsilon)$ fields, the results of which are

$$\begin{aligned} (\overline{u\zeta})_1^{(2)} &= \frac{1}{4} \epsilon \frac{N^2}{K^2} \left[2km \partial_X + (2m^2 - K^2) \partial_Z \right] |A|^2 e^{z/H\rho}; \\ (\overline{w\zeta})_1^{(2)} &= \frac{1}{4} \epsilon \frac{N^2}{K^2} \left[(K^2 - 2k^2) \partial_X - 2km \partial_Z \right] |A|^2 e^{z/H\rho}; \\ (\overline{u\xi})_1^{(2)} &= \frac{1}{4} \epsilon \frac{N}{K^3} \left[-km \partial_X + (K^2 - m^2) \partial_Z \right] |A|^2 e^{z/H\rho}; \\ (\overline{w\xi})_1^{(2)} &= \frac{1}{4} \epsilon \frac{N}{K^3} \left[-(K^2 - k^2) \partial_X + km \partial_Z \right] |A|^2 e^{z/H\rho}, \end{aligned}$$

where $|\cdot|$ denotes the modulus. That the rightmost term in \mathbf{F} has neither x -, z -, nor t -derivatives applied to it (as opposed to the first two terms in \mathbf{F}) suggests the need to include the contribution of $(\overline{w\xi})_2^{(2)}$. This is achieved using the product of the $w_2^{(1)}$ and $\xi_0^{(1)}$ fields, in which $w_2^{(1)}$ is recovered from the $O(\epsilon^2)$ part of the perturbation expansion for w . However, we remark that because the coefficient on $w_2^{(1)}$ is purely imaginary and the coefficient on $\xi_0^{(1)}$ is purely real, it follows that $(\overline{w\xi})_2^{(2)} \equiv 0$. Hence, substituting the $O(\alpha^2\epsilon)$ mean fields into \mathbf{F} , computing the divergence, and simplifying the resulting equation finally yields

$$(\nabla \cdot \mathbf{F})_3^{(2)} = -\frac{1}{4} \epsilon^3 \frac{N^3}{K^5} e^{z/H\rho} \mathcal{K} |A|^2, \quad (2.20)$$

where, for notational ease, the partial differential operator \mathcal{K} is defined as

$$\begin{aligned} \mathcal{K} := & km[3K^2 - 2k^2]\partial_{XXX} + \left[3m^4 - 4k^2m^2 - k^4 + 3(m^2 - k^2)\frac{1}{4H\rho^2}\right]\partial_{XXZ} \\ & - km[3K^2 + 2m^2 - 4k^2]\partial_{XZZ} + [2k^2m^2]\partial_{ZZZ} \\ & - \frac{1}{\epsilon H\rho}K^2[K^2 - k^2]\partial_{XX} + \frac{1}{\epsilon H\rho}[K^2km]\partial_{XZ}. \end{aligned} \quad (2.21)$$

In previous studies of Boussinesq wavepackets (Bretherton, 1969; Tabaei and Akylas, 2007; van den Bremer and Sutherland, 2014), the induced flow was found to be a horizontally long, hence hydrostatic wave. Assuming this result likewise holds for anelastic wavepackets, X -derivatives of $|A|^2$, acting through \mathcal{K} , are assumed to be negligibly small compared to the term with Z -derivatives alone (vdBS14). Hence

$$(\nabla \cdot \mathbf{F})_3^{(2)} \approx -\epsilon^3 \frac{N^3 k^2 m^2}{2 K^5} e^{z/H\rho} \partial_{ZZZ} |A(X, Z)|^2. \quad (2.22)$$

Following Bretherton (1969), vdBS14 approximated the X -dependent contribution to (2.22) as a Dirac delta function. In seeking an analytic solution, the wavepacket was subsequently prescribed to be a Gaussian. In contrast, we require only that the wavepacket satisfy sufficient differentiability and integrability properties in order to perform Fourier transforms later on. Otherwise we make no assumptions about the structure of the wavepacket amplitude envelope function. We denote such a generic vertical displacement amplitude function by $A := A_\xi = A_0 \mathcal{A}(\tilde{x}, \tilde{z}, t)$, where \mathcal{A} may be complex-valued and $\max_{\tilde{x}, \tilde{z}} |\mathcal{A}| = 1$ initially. Furthermore, we will write the following results in terms of the fast-scale variables translating at the group velocity of the wavepacket,

$$\tilde{x} = \frac{X}{\epsilon} = x - c_{g_x} t \quad \text{and} \quad \tilde{z} = \frac{Z}{\epsilon} = z - c_{g_z} t. \quad (2.23a,b)$$

Under this change of variables, the nonlinear forcing given by (2.22) is written

$$(\nabla \cdot \mathbf{F})_3^{(2)} \approx -\frac{1}{2} \frac{N^3 k^2 m^2}{K^5} A_0^2 e^{z/H\rho} \partial_{\tilde{z}\tilde{z}\tilde{z}} |\mathcal{A}(\tilde{x}, \tilde{z}, t)|^2,$$

in which we have explicitly re-introduced dependence on t in the amplitude function.

The operator \mathcal{L} , defined in (2.15), is re-cast in terms of \tilde{x} and \tilde{z} . Using the anticipated long wave response, the constituent operators in \mathcal{L} are consequently expressed as $\partial_{tt} \approx c_{g_z}^2 \partial_{\tilde{z}\tilde{z}}$

and $\partial_{\tilde{x}\tilde{x}} + \partial_{\tilde{z}\tilde{z}} \approx \partial_{\tilde{z}\tilde{z}}$ (vdBS14). Equation (2.15) thus reads

$$[c_{g_z}^2 \partial_{\tilde{z}\tilde{z}\tilde{z}\tilde{z}} + \frac{1}{H_\rho} c_{g_z}^2 \partial_{\tilde{z}\tilde{z}\tilde{z}} + N^2 \partial_{\tilde{x}\tilde{x}}] \Psi^{(2)} = -\frac{1}{2} \rho_0 \frac{N^3 k^2 m^2}{K^5} A_0^2 \partial_{\tilde{z}\tilde{z}\tilde{z}} |\mathcal{A}(\tilde{x}, \tilde{z}, t)|^2. \quad (2.24)$$

For an appropriate function η , we denote by a caret the (two-dimensional) Fourier transform of η , and we define the Fourier transform pair

$$\begin{aligned} \hat{\eta} &= \frac{1}{(2\pi)^2} \int_{\mathbb{R}^2} \eta e^{-i(\kappa\tilde{x} + \mu\tilde{z})} d\tilde{x} d\tilde{z}; \\ \eta &= \int_{\mathbb{R}^2} \hat{\eta} e^{i(\kappa\tilde{x} + \mu\tilde{z})} d\kappa d\mu. \end{aligned}$$

In Fourier space, on the left-hand side of (2.24) derivatives with respect to \tilde{x} are expressed as multiplicative factors of $i\kappa$ and derivatives with respect to \tilde{z} are similarly expressed as factors of $i\mu$. Taking the Fourier transform of (2.24) and rearranging yields the equation for mass-streamfunction in Fourier space,

$$\widehat{\Psi^{(2)}}(\kappa, \mu) = \frac{i}{2} \rho_0 \frac{N^3 k^2 m^2}{K^5} A_0^2 \frac{\mu^3 |\widehat{\mathcal{A}}|^2}{c_{g_z}^2 \mu^4 - i \frac{1}{H_\rho} c_{g_z}^2 \mu^3 - N^2 \kappa^2}. \quad (2.25)$$

The solution for the mass-streamfunction in real space is found by taking the inverse Fourier transform of (2.25). Upon rearranging the denominator in the integrand to factor N^2 out of the κ^2 term, this is given by

$$\Psi^{(2)} = \frac{i}{2} \rho_0 \frac{N k^2 m^2}{K^5} A_0^2 \int_{\mathbb{R}^2} \frac{\mu^3 |\widehat{\mathcal{A}}|^2 e^{i(\kappa\tilde{x} + \mu\tilde{z})}}{\frac{c_{g_z}^2}{N^2} [\mu^4 - i \frac{1}{H_\rho} \mu^3] - \kappa^2} d\kappa d\mu. \quad (2.26)$$

This equation can be explicitly integrated with respect to κ as was done by vdBS14 for Boussinesq wavepackets, their integral expression being equivalent to letting $H_\rho \rightarrow \infty$ in (2.26). Here, this task is non-trivial due to the presence of complex singularities in the integrand. The details of the integration of (2.26) are provided in Appendix A. In practice, when numerically solving the governing equations for two-dimensional wavepackets, it is more convenient instead to compute the wave-induced momentum, $\bar{\rho}u^{(2)}$, in Fourier space using (2.13a) and (2.25), so that

$$\widehat{\bar{\rho}u^{(2)}} = -\widehat{\partial_{\tilde{z}} \Psi^{(2)}} = -i\mu \widehat{\Psi^{(2)}} = \frac{1}{2} \rho_0 \frac{N k^2 m^2}{K^5} A_0^2 \frac{\mu^4 |\widehat{\mathcal{A}}|^2}{2C(\mu)} \left[\frac{1}{\kappa + C(\mu)} - \frac{1}{\kappa - C(\mu)} \right], \quad (2.27)$$

in which the function $C(\mu)$ is given by (A.2). The wave-induced momentum in real space is

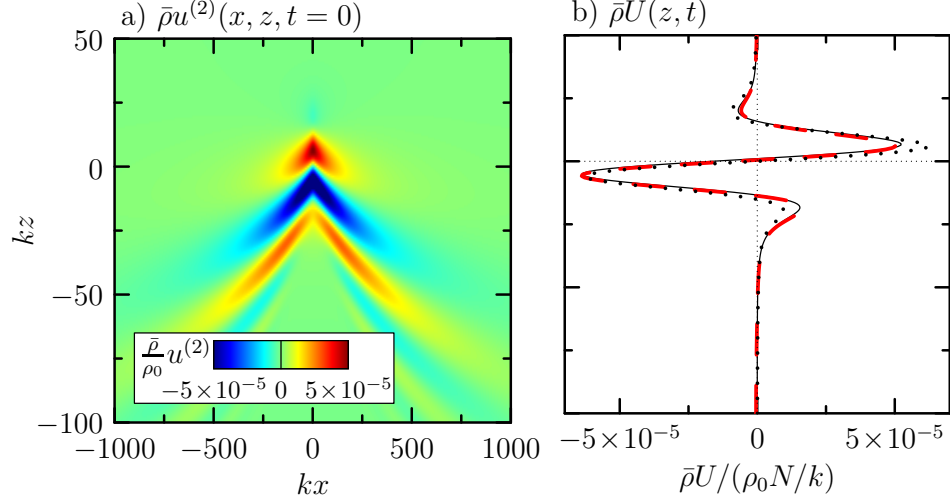


Figure 2.1: (a) Plot of wave-induced momentum, $\bar{\rho}u^{(2)}(x, z, 0)$, using the fast Fourier transform method detailed in §3.2.4. (b) Three vertical profiles of wave-induced momentum. The black solid curve is that extracted from the induced momentum field shown in (a); the dashed red profile is that computed using (A.16); the dotted black curve is that computed using (A.16) for an effectively Boussinesq gas, for which $H_\rho = 1000k^{-1}$.

found by horizontally and vertically inverse transforming (2.27), which yields

$$\bar{\rho}u^{(2)}(\tilde{x}, \tilde{z}) = \int_{\mathbb{R}^2} \widehat{\bar{\rho}u^{(2)}} e^{i(\kappa\tilde{x} + \mu\tilde{z})} d\kappa d\mu. \quad (2.28)$$

The wave-induced mean flow through the horizontal centre of the translating wavepacket, in fixed coordinates, is found using

$$U(z, t) = u^{(2)}(x = c_{g_x}t, z, t). \quad (2.29)$$

Details of the numerical procedures used to evaluate (2.28) and (2.29) are provided in §3.2.4.

For illustrative purposes, the initial horizontal momentum field, $\bar{\rho}u^{(2)}(x, z, 0)$, computed using (2.28), is shown in Fig. 2.1a. Qualitatively the induced long wave resembles a bow wake, predicted by Bretherton (1969) and shown for two-dimensional Boussinesq wavepackets by vdBS14 (c.f. figure 2 in that work). Fig. 2.1b shows three vertical profiles of the wave-induced momentum taken through the horizontal centre of the wavepacket (that is, through $\tilde{x} = x - c_{g_x}t = 0$). The solid black curve is the profile found by directly extracting the profile through $\tilde{x} = 0$ in Fig. 2.1a computed by applying fast Fourier transforms to (2.28). The dashed red curve is computed using $\tilde{x} = 0$ in the integral expression (A.16). That the curves overlap demonstrates the agreement between the results of the fast Fourier transform method detailed in §3.2.4 and the residue method detailed in Appendix A. The dotted black curve is

the profile computed for an effectively Boussinesq gas, using $H_\rho = 1000k^{-1}$ in (A.16). This demonstrates the qualitative similarities among the anelastic and Boussinesq wave-induced momentum profiles. In particular, the values are positive along the leading flank of the wavepacket and negative on the trailing flank, and approximately symmetric about $z = 0$. The magnitude of the anelastic induced momentum profile is smaller on the leading flank than on the trailing flank. However, it should be kept in mind that, due to anelastic effects, the wave-induced mean flow U will generally be of greater magnitude along the leading flank than along the trailing flank after dividing $\bar{\rho}U$ by the background density.

A key difference between the mean flows induced by one- and two-dimensional wavepackets is their order in α and ϵ . Crucially, in two dimensions $U \sim O(\alpha^2\epsilon)$, whereas in one dimension $U_{1D} \sim O(\alpha^2)$. In the next sections, these quantitative differences will be exploited in the derivations of the Boussinesq and anelastic weakly nonlinear governing equations.

2.3 Schrödinger Equation for a Boussinesq Gas

Before deriving the nonlinear Schrödinger equation for horizontally and vertically localized anelastic wavepackets, it is necessary to derive its Boussinesq analogue. Most importantly, this will serve as a template for deriving the anelastic nonlinear Schrödinger equation, and as a partial means of confirming its correctness. This derivation is closely based on the approach taken by Dosser (2010). We begin with the incompressible Euler equations for a Boussinesq gas given by (2.7), (2.2), and (2.8). However, we will explicitly write the velocity vector components in terms of “total” fields, which we denote by a subscript T . A total field is defined as the sum of background and fluctuation components. Explicitly, the total velocity fields are given by

$$\begin{aligned} u_T &= u(x, z, t) + U(z, t); \\ w_T &= w(x, z, t), \end{aligned}$$

in which $U(z, t)$ is the local wave-induced mean flow for a Boussinesq gas, found by taking $H_\rho \rightarrow \infty$ in (2.29). The vertical component of the induced flow field, W , is not included in the total vertical velocity field, w_T , under the hydrostatic approximation that $\|W\| \ll \|U\|$.

Expressed explicitly in terms of total fields, the momentum equation, internal energy equation, and incompressibility condition thus read, respectively

$$\rho_0 \frac{D\mathbf{u}_T}{Dt} = -\nabla p + \frac{g\rho_0}{\theta_0} \theta \hat{\mathbf{e}}_z; \quad (2.30a)$$

$$\frac{D\theta}{Dt} = -w_T \frac{d\bar{\theta}}{dz}; \quad (2.30b)$$

$$\nabla \cdot \mathbf{u}_T = 0, \quad (2.30c)$$

where $D/Dt = \partial_t + \mathbf{u}_T \cdot \nabla$ is the material derivative expressed in terms of total fields and the total velocity vector is $\mathbf{u}_T = (u_T, w_T)$.

We eliminate the pressure terms by taking the curl of the momentum equation (2.30a), which upon rearrangement yields

$$\rho_0 \frac{D\zeta_T}{Dt} = -\frac{g\rho_0}{\theta_0} \partial_x \theta, \quad (2.31)$$

in which the total spanwise vorticity is defined as

$$\zeta_T := (\nabla \times \mathbf{u}_T) \cdot \hat{\mathbf{e}}_y. \quad (2.32)$$

The incompressibility condition (2.30c) allows us to express the total velocity components as derivatives of the total streamfunction, ψ_T , given implicitly by the relations

$$u_T = -\partial_z \psi_T, \quad \text{and} \quad w_T = \partial_x \psi_T. \quad (2.33a,b)$$

Here, $\psi_T = \psi(x, z, t) + \bar{\psi}(z, t)$, in which $\bar{\psi}(z, t)$ is the $O(\alpha^2 \epsilon)$ induced streamfunction given by (2.26) in the limit $H_\rho \rightarrow \infty$ and evaluated at $\tilde{x} = 0$. The vorticity is related to the streamfunction by substituting the relations (2.33a,b) into the definition of ζ_T , which reveals that

$$\zeta_T = -\nabla^2 \psi_T.$$

Substituting this relation into (2.31), applying the incompressibility condition, expanding the material derivative, and explicitly separating the total velocity and streamfunction into their background and fluctuation components, then simplifying the resulting expression, yields

$$\partial_t \nabla^2 \psi - \partial_{tz} U + u \partial_x \nabla^2 \psi + U \partial_x \nabla^2 \psi + w \partial_z \nabla^2 \psi - w \partial_{zz} U = \frac{g}{\theta_0} \partial_x \theta, \quad (2.34)$$

in which we have identified that $\partial_z \bar{\psi} = -U$ using (2.33a).

We assume evolution of the wavepacket envelope function occurs on a much slower scale than that of the waves themselves. We hence re-introduce the slow variables X , Z , and T , defined in (2.18a,b,c), and express the fluctuation streamfunction and potential temperature in terms of the slow variables:

$$\psi = A_\psi(X, Z, T)e^{i\varphi}; \quad (2.35)$$

$$\theta = A_\theta(X, Z, T)e^{i\varphi}, \quad (2.36)$$

where $\varphi = kx + mz - \omega t$ is the phase, and it is understood that ψ and θ are the real parts of the right-hand sides of (2.35) and (2.36), respectively. Note that subscripts T denote partial derivatives with respect to the slow variable T . Under the change of variables, derivatives of any basic wave field $\eta = A_\eta(X, Z, T)e^{i\varphi}$ are given by

$$\partial_x \rightarrow \epsilon \partial_X + ik; \quad (2.37a)$$

$$\partial_z \rightarrow \epsilon \partial_Z + im; \quad (2.37b)$$

$$\partial_t \rightarrow \epsilon^2 \partial_T - \epsilon \mathbf{c}_g \cdot \nabla - i\omega, \quad (2.37c)$$

in which $\mathbf{c}_g = (c_{gx}, c_{gz})$ is the group velocity vector and, somewhat ambiguously, $\nabla = (\partial_X, \partial_Z)$ is henceforth understood to operate in terms of the slow variables.

Substituting (2.35) and (2.36) into (2.34), making the change of variables $(x, z, t) \rightarrow (X, Z, T)$ and extracting only terms contributing to wave-like motion (i.e. extracting only those terms containing the factor $e^{i\varphi}$) yields a partial differential equation in terms of a non-linear operator acting on the streamfunction amplitude on the left-hand side and a linear operator acting on the potential temperature amplitude on the right-hand side. Explicitly,

$$\begin{aligned} & \{(\epsilon^2 \nabla^2 + 2i\epsilon \mathbf{k} \cdot \nabla - |\mathbf{k}|^2)(\epsilon^2 \partial_T - \epsilon \mathbf{c}_g \cdot \nabla - i\omega + U[\epsilon \partial_X + ik]) - \epsilon^2(\epsilon \partial_X + ik)\partial_{ZZ}U\}A_\psi \\ & = \frac{g}{\theta_0}(\epsilon \partial_X + ik)A_\theta, \end{aligned} \quad (2.38)$$

in which $\mathbf{k} = (k, m)$ is the wavenumber vector, and $|\mathbf{k}| = (k^2 + m^2)^{1/2}$ is its Euclidean norm. We eliminate the dependence on the potential temperature by substituting (2.36) into the internal energy equation (2.30b), retaining only terms containing the factor $e^{i\varphi}$, and

multiplying both sides of the resulting equation by $(g/\theta_0)(\epsilon\partial_X + ik)$ to obtain

$$\frac{g}{\theta_0}(\epsilon^2\partial_T - \epsilon\mathbf{c}_g \cdot \nabla - i\omega + U[\epsilon\partial_X + ik])(\epsilon\partial_X + ik)A_\theta = -\frac{d\bar{\theta}}{dz} \frac{g}{\theta_0}(\epsilon\partial_X + ik)^2 A_\psi. \quad (2.39)$$

Applying the operator $(\epsilon^2\partial_T - \epsilon\mathbf{c}_g \cdot \nabla - i\omega + U[\epsilon\partial_X + ik])$ to both sides of (2.38) and equating the left-hand side of the resulting equation with the right-hand side of (2.39) finally yields a single equation for the evolution of the streamfunction amplitude at all orders in α and ϵ . Explicitly,

$$\begin{aligned} & (\epsilon^2\partial_T - \epsilon\mathbf{c}_g \cdot \nabla - i\omega + U[\epsilon\partial_X + ik]) \times \\ & \left\{ (\epsilon^2\partial_T - \epsilon\mathbf{c}_g \cdot \nabla - i\omega + U[\epsilon\partial_X + ik])(\epsilon^2\nabla^2 + 2i\epsilon\mathbf{k} \cdot \nabla - |\mathbf{k}|^2) - \epsilon^2[\epsilon\partial_X + ik]\partial_{ZZ}U \right\} A_\psi \\ & = -N^2(\epsilon^2\partial_{XX} + 2i\epsilon k\partial_X - k^2)A_\psi, \end{aligned} \quad (2.40)$$

in which $\alpha = A_0k$ is a nondimensional measure of wavepacket amplitude identical to that used in the derivation of the wave-induced mean flow. We now assume the streamfunction amplitude and the local wave-induced mean flow can be expanded in perturbation expansions of the forms $A_\psi = \alpha(B_0 + \alpha B_1 + \alpha^2 B_2 + \dots)$ and $U = \alpha^2\epsilon(V_0 + \alpha V_1 + \dots)$, respectively. Substituting these into (2.40), the nonlinear Schrödinger equation is derived by extracting $O(\alpha^r \epsilon^s)$ terms of the resulting equation up to and including combined order $r + s = 4$. Upon completion of this procedure, it will be assumed that $\alpha \sim \epsilon$ so that dispersion balances nonlinearity.

The $O(\alpha\epsilon^0)$ equation recovers the linear dispersion relation for internal gravity waves given in Table 2.2. The $O(\alpha^2) = O(\alpha^2\epsilon^0 + \alpha\epsilon)$ equation yields $0 = 0$ as a consequence of working in a frame of reference translating at the group velocity of the wavepacket. The $O(\alpha^3) = O(\alpha^3\epsilon^0 + \alpha^2\epsilon + \alpha\epsilon^2)$ equation yields the linear Schrödinger equation for two-dimensional wavepackets in a frame of reference translating at the wavepacket's group velocity,

$$\partial_T B_0 = i \left\{ \frac{1}{2}\omega_{kk}\partial_{XX} + \omega_{km}\partial_{XZ} + \frac{1}{2}\omega_{mm}\partial_{ZZ} \right\} B_0,$$

in which the subscripts on ω denote partial derivatives with respect to the wavenumber components. Before proceeding to computing the $O(\alpha^4) = O(\alpha^4\epsilon^0 + \alpha^3\epsilon + \alpha^2\epsilon^2 + \alpha\epsilon^3)$ equation, we remark that the $O(\alpha\epsilon^3)$ equation in particular contains mixed time-space derivative terms.

Dispersion relation and its derivatives	
$\omega = Nk/ \mathbf{k} $	$\omega_{kkk} = 3Nm^2(4k^2 - m^2)/ \mathbf{k} ^7$
$c_{g_x} = \omega_k = Nm^2/ \mathbf{k} ^3$	$\omega_{kkm} = 3Nkm(3m^2 - 2k^2)/ \mathbf{k} ^7$
$c_{g_z} = \omega_m = -Nkm/ \mathbf{k} ^3$	$\omega_{kmm} = -N(2k^4 - 11k^2m^2 + 2m^4)/ \mathbf{k} ^7$
$\omega_{kk} = -3Nkm^2/ \mathbf{k} ^5$	$\omega_{mmm} = 3Nkm(3k^2 - 2m^2)/ \mathbf{k} ^7$
$\omega_{km} = -Nm(m^2 - 2k^2)/ \mathbf{k} ^5$	
$\omega_{mm} = -Nk(k^2 - 2m^2)/ \mathbf{k} ^5$	

Table 2.2: Expressions for the linear dispersion relation, ω , and its derivatives up to third-order, for internal gravity waves in a Boussinesq gas. Here, $|\mathbf{k}| = (k^2 + m^2)^{1/2}$ in which k and m are the horizontal and vertical wavenumbers, respectively.

These mixed derivatives are eliminated by applying the following linear operation to the $O(\alpha\epsilon^2)$ equations:

$$\frac{1}{2i\omega|\mathbf{k}|^2} \left\{ O(\alpha\epsilon^3) + i\frac{1}{|\mathbf{k}|^2k}(2k^2 + m^2)\partial_X O(\alpha\epsilon^2) + i\frac{m}{|\mathbf{k}|^2}\partial_Z O(\alpha\epsilon^2) \right\}. \quad (2.41)$$

Taking slow spatial derivatives of the $O(\alpha\epsilon^2)$ equations raises those equations by one order in ϵ . The resulting combined $O(\alpha^4)$ equation is

$$\begin{aligned} \partial_T B_1 = & \left\{ \frac{1}{2}i\omega_{kk}\partial_{XX} + i\omega_{km}\partial_{XZ} + \frac{1}{2}i\omega_{mm}\partial_{ZZ} \right\} B_1 \\ & + \left\{ \frac{1}{6}\omega_{kkk}\partial_{XXX} + \frac{1}{2}\omega_{kkm}\partial_{XXZ} + \frac{1}{2}\omega_{kmm}\partial_{XZZ} + \frac{1}{6}\omega_{mmm}\partial_{ZZZ} \right\} B_0 - ikV_0B_0, \end{aligned}$$

which includes leading- and next-order linear dispersion terms and the nonlinear term representing the Doppler-shifting of the waves by their induced mean flow.

Finally, recombining all orders and returning to the fast-scale variables in a fixed frame of reference reveals the nonlinear Schrödinger equation for horizontally and vertically localized wavepackets in a Boussinesq gas,

$$\begin{aligned} \partial_t A_\psi = & -\left\{ \omega_k\partial_x + \omega_m\partial_z \right\} A_\psi + \left\{ \frac{1}{2}i\omega_{kk}\partial_{xx} + i\omega_{km}\partial_{xz} + \frac{1}{2}i\omega_{mm}\partial_{zz} \right\} A_\psi \\ & + \left\{ \frac{1}{6}\omega_{kkk}\partial_{xxx} + \frac{1}{2}\omega_{kkm}\partial_{xxz} + \frac{1}{2}\omega_{kmm}\partial_{xzz} + \frac{1}{6}\omega_{mmm}\partial_{zzz} \right\} A_\psi - ikUA_\psi, \end{aligned} \quad (2.42)$$

in which the subscripts on ω denote partial derivatives with respect to the horizontal and vertical wavenumbers k and m . The dispersion relation ω and its derivatives are summarized in Table 2.2.

The first set of braced terms on the right-hand side of (2.42) represents advection at the

wavepacket’s horizontal and vertical group speeds, respectively. The second and third sets of braced terms represent linear dispersion at leading- and second-order, respectively. The derivatives purely in x or z represent dispersion in their respective directions, whereas mixed spatial derivatives represent dispersion in neither the x - nor z -direction. We therefore refer to these as “oblique dispersion” terms. The inclusion of third-order derivative terms is necessary to balance the effects of dispersion with nonlinearity arising at $O(\alpha^2\epsilon)$ through interactions between the waves and their induced mean flow. Moreover, third-order derivative terms are necessary to capture the dispersion of waves traveling at the fastest horizontal and vertical group velocities, for which $\omega_{km} \approx 0$ and $\omega_{mm} \approx 0$, respectively (Sutherland, 2006b). The final term on the right-hand side represents the leading-order effects of nonlinearity through the interaction between the wavepacket and its induced mean flow $U = u^{(2)}(x = c_{g_x}t, z, t)$, in which $u^{(2)}$ is explicitly a function of time because A_ψ evolves in time according to (2.42).

In the limit as the wavepacket becomes arbitrarily long (i.e. as $\sigma_x \rightarrow \infty$), the wavepacket’s structure becomes uniform in the horizontal. Hence all terms containing at least one x -derivative vanish and the linear part of the resulting equation exactly recovers the linear part of the Boussinesq nonlinear Schrödinger equation derived by Sutherland (2006b) for horizontally periodic, vertically localized wavepackets (c.f. equations 2.10 and 2.11 in that work). The wave-induced mean flow U does not recover its one-dimensional analogue, given by (1.4), because the induced flows in one and two dimensions are qualitatively different (Tabaei and Akylas, 2007; van den Bremer and Sutherland, 2018).

2.4 Schrödinger Equation for an Anelastic Gas

Having established the expression for the flow induced by horizontally and vertically localized wavepackets in an anelastic gas, and the Boussinesq nonlinear Schrödinger equation modeling the interactions between the waves and their induced flow, we are now able to derive the nonlinear Schrödinger equation that models the evolution of horizontally and vertically localized wavepackets in an anelastic gas. In the following derivation, we assume a background density profile described by (2.3). We begin with the incompressible Euler equations for an anelastic gas, given by (2.1), (2.2), and (2.6). Following the approach taken in the derivation of the

Boussinesq nonlinear Schrödinger equation, we write the velocity vector components in terms of the total fields, given by

$$u_T = u(x, z, t) + U(z, t);$$

$$w_T = w(x, z, t),$$

in which $U(z, t)$ is the local wave-induced mean flow given by (2.29). By the hydrostatic approximation, $\|W\| \ll \|U\|$, where W is the vertical component of the induced flow field. Hence W is not included in the total vertical velocity field, w_T . Expressed explicitly in terms of total fields, the momentum equation, internal energy equation, and anelastic condition thus read, respectively

$$\frac{D\mathbf{u}_T}{Dt} = -\nabla\left(\frac{p}{\bar{\rho}}\right) + \frac{g}{\bar{\theta}}\hat{\mathbf{e}}_z; \quad (2.43a)$$

$$\frac{D\theta}{Dt} = -w_T\frac{d\bar{\theta}}{dz}; \quad (2.43b)$$

$$\nabla \cdot (\bar{\rho}\mathbf{u}_T) = 0, \quad (2.43c)$$

where $D/Dt = \partial_t + \mathbf{u}_T \cdot \nabla$ is the material derivative expressed in terms of total fields and the total velocity vector is $\mathbf{u}_T = (u_T, w_T)$.

The pressure terms are eliminated by taking the curl of the momentum equation (2.43a), which, upon rearrangement, yields

$$\frac{D\zeta_T}{Dt} = -(\nabla \cdot \mathbf{u}_T)\zeta_T - \frac{g}{\bar{\theta}}\partial_x\theta, \quad (2.44)$$

where ζ_T is the total spanwise vorticity, defined as in (2.32).

The anelastic condition (2.43c) allows us to express the total velocity components as density-normalized derivatives of the total mass-streamfunction, Ψ_T , given by the relations

$$u_T = -\frac{1}{\bar{\rho}}\partial_z\Psi_T, \quad \text{and} \quad w_T = \frac{1}{\bar{\rho}}\partial_x\Psi_T. \quad (2.45a,b)$$

Here, $\Psi_T = \Psi(x, z, t) + \bar{\Psi}(z, t)$, in which $\bar{\Psi}(z, t)$ is the $O(\alpha^2\epsilon)$ induced mass-streamfunction, given by (2.26), evaluated at $\tilde{x} = 0$. The total spanwise vorticity is related to the mass-

streamfunction by substituting the relations (2.45a,b) into ζ_T , which yields

$$\zeta_T = -\frac{1}{\bar{\rho}} \left[\nabla^2 \Psi_T + \frac{1}{H_\rho} \partial_z \Psi_T \right]. \quad (2.46)$$

The anelastic condition $\nabla \cdot (\bar{\rho} \mathbf{u}_T) = 0$ is equivalently stated as $\nabla \cdot \mathbf{u}_T = w_T/H_\rho$. Substituting this and (2.46) into (2.44) yields

$$\frac{D}{Dt} \left\{ \frac{1}{\bar{\rho}} \left[\nabla^2 \Psi_T + \frac{1}{H_\rho} \partial_z \Psi_T \right] \right\} = -\frac{w_T}{H_\rho} \left[\frac{1}{\bar{\rho}} \left(\nabla^2 \Psi_T + \frac{1}{H_\rho} \partial_z \Psi_T \right) \right] + \frac{g}{\theta} \partial_x \theta.$$

Expanding the material derivative, multiplying both sides of the resulting equation by $\bar{\rho}$, and explicitly separating the total velocity and mass-streamfunction fields into their background and fluctuation components, yields a nonlinear equation involving Ψ , $\bar{\Psi}$, u , U , and w on the left-hand side and θ on the right-hand side. Applying the relations (2.45a,b) to the fluctuation components of \mathbf{u}_T , and identifying that $\partial_z \bar{\Psi} = -\bar{\rho}U$ using (2.45a), the equation can be re-written purely in terms of the fluctuation mass-streamfunction Ψ and the wave-induced mean flow U on the left-hand side and the fluctuation potential temperature θ on the right-hand side. Explicitly,

$$\begin{aligned} \partial_t \nabla^2 \Psi - \bar{\rho} \partial_{tz} U + \frac{1}{H_\rho} \partial_{tz} \Psi - \frac{1}{\bar{\rho}} \partial_z \Psi \partial_x \nabla^2 \Psi - \frac{1}{\bar{\rho} H_\rho} \partial_z \Psi \partial_{xz} \Psi + U \partial_x \nabla^2 \Psi + \frac{1}{H_\rho} U \partial_{xz} \Psi \\ + \frac{2}{\bar{\rho} H_\rho} \partial_x \Psi \nabla^2 \Psi + \frac{2}{\bar{\rho} H_\rho^2} \partial_x \Psi \partial_z \Psi + \frac{1}{\bar{\rho}} \partial_x \Psi \partial_z \nabla^2 \Psi - \partial_x \Psi \partial_{zz} U + \frac{1}{\bar{\rho} H_\rho} \partial_x \Psi \partial_{zz} \Psi \\ = N^2 \bar{\rho} \left(\frac{d\bar{\theta}}{dz} \right)^{-1} \partial_x \theta, \end{aligned} \quad (2.47)$$

in which we have used the definition of the squared buoyancy frequency for an anelastic gas, given by (2.5), on the right-hand side of (2.47).

Because we are working with wavepackets, it is reasonable to assume that the amplitude envelope function evolves much more slowly than the waves themselves, and hence we re-introduce the slow-scale variables X , Z , and T , as defined in (2.18a,b,c). Explicitly expressed in terms of the slow variables, the fluctuation mass-streamfunction and potential temperature fields are

$$\Psi = A_\Psi(X, Z, T) e^{i\varphi - z/2H_\rho}, \quad (2.48)$$

$$\theta = A_\theta(X, Z, T) e^{i\varphi - z/2H_\rho}, \quad (2.49)$$

where $\varphi = kx + mz - \omega t$ is the phase, and it is understood that Ψ and θ are the real parts of the right-hand sides of (2.48) and (2.49), respectively. Note that subscripts T now denote partial derivatives with respect to the slow time variable T . Under this change of variables, derivatives of any basic wave field $\eta = A_\eta(X, Z, T)e^{i\varphi - z/2H_\rho}$ are given by

$$\partial_x \rightarrow \epsilon \partial_X + ik; \quad (2.50a)$$

$$\partial_z \rightarrow \epsilon \partial_Z + im - 1/(2H_\rho); \quad (2.50b)$$

$$\partial_t \rightarrow \epsilon^2 \partial_T - \epsilon \mathbf{c}_g \cdot \nabla - i\omega, \quad (2.50c)$$

in which $\mathbf{c}_g = (c_{g_x}, c_{g_z})$ is the group velocity vector and $\nabla = (\partial_X, \partial_Z)$ is understood to operate in terms of the slow variables.

Substituting (2.48) and (2.49) into (2.47), making the change of variables $(x, z, t) \rightarrow (X, Z, T)$, and extracting only terms containing the factor $e^{i\varphi}$ yields a partial differential equation in terms of a nonlinear operator acting on the mass-streamfunction amplitude on the left-hand side and a linear operator acting on the potential temperature amplitude on the right-hand side. Explicitly,

$$\begin{aligned} \mathcal{N}_U(\epsilon^2 \nabla^2 + 2i\mathbf{k} \cdot \nabla - K^2)A_\Psi - (\epsilon^2 \partial_{ZZ} U + \epsilon \frac{1}{H_\rho} \partial_Z U)(\epsilon \partial_X + ik)A_\Psi \\ = N^2 \bar{\rho} \left(\frac{d\bar{\theta}}{dz} \right)^{-1} (\epsilon \partial_X + ik)A_\theta, \end{aligned} \quad (2.51)$$

in which $K^2 = |\mathbf{k}|^2 + 1/(4H_\rho^2)$ and we have defined the nonlinear partial differential operator

$$\mathcal{N}_U := \epsilon^2 \partial_T - \epsilon \mathbf{c}_g \cdot \nabla - i\omega + U[\epsilon \partial_X + ik]$$

for notational convenience. We eliminate the dependence on the potential temperature using a similar procedure as in the derivation of the nonlinear Schrödinger equation for a Boussinesq gas. We substitute (2.48) into the internal energy equation (2.43b), retain only terms containing the factor $e^{i\varphi}$, and multiply both sides of the resulting equation by $N^2 \bar{\rho} (d\bar{\theta}/dz)^{-1} (\epsilon \partial_X + ik)$, thus obtaining

$$\mathcal{N}_U N^2 \bar{\rho} \left(\frac{d\bar{\theta}}{dz} \right)^{-1} (\epsilon \partial_X + ik)A_\theta = -N^2 (\epsilon \partial_X + ik)^2 A_\Psi. \quad (2.52)$$

Applying the operator \mathcal{N}_U to both sides of (2.51) and equating the left-hand side of the

resulting equation with the right-hand side of (2.52) yields a single equation for the evolution of the mass-streamfunction amplitude at all orders in α and ϵ . Explicitly,

$$\begin{aligned} \mathcal{N}_U \left\{ \mathcal{N}_U (\epsilon^2 \nabla^2 + 2i\epsilon \mathbf{k} \cdot \nabla - K^2) - (\epsilon^2 \partial_{ZZ} U + \epsilon \frac{1}{H_\rho} \partial_Z U) (\epsilon \partial_X + ik) \right\} A_\Psi \\ = -N^2 (\epsilon^2 \partial_{XX} + 2i\epsilon k \partial_X - k^2) A_\Psi, \end{aligned} \quad (2.53)$$

in which $\alpha = A_0 k$ is the nondimensional measure of wavepacket amplitude used in the derivations of the wave-induced mean flow and the Boussinesq nonlinear Schrödinger equation. We perform a regular perturbation expansion of the mass-streamfunction amplitude function, written as $A_\Psi = \alpha(B_0 + \alpha B_1 + \alpha^2 B_2 + \dots)$, and of the wave-induced mean flow, written as $U = \alpha^2 \epsilon (V_0 + \alpha V_1 + \dots)$. Substituting these expansions into (2.53) and taking the Boussinesq limit $H_\rho \rightarrow \infty$, we observe that the resulting equation—and hence its $O(\alpha^r \epsilon^s)$ terms—is identical to the Boussinesq nonlinear Schrödinger equation (2.40).

As such we may exactly follow the procedures from the previous section for extracting each $O(\alpha^r \epsilon^s)$ term, and for eliminating the mixed time-space derivative terms appearing at $O(\alpha \epsilon^3)$. We then assume that $\alpha \sim \epsilon$ and recombine all terms up to and including the combined $O(\alpha^4)$. Returning to the fast-scale variables in a fixed frame of reference, the resulting equation finally yields the nonlinear Schrödinger equation for horizontally and vertically localized wavepackets in an anelastic gas,

$$\begin{aligned} \partial_t A_\Psi = -\{\omega_k \partial_x + \omega_m \partial_z\} A_\Psi + \left\{ \frac{1}{2} i \omega_{kk} \partial_{xx} + i \omega_{km} \partial_{xz} + \frac{1}{2} i \omega_{mm} \partial_{zz} \right\} A_\Psi \\ + \left\{ \frac{1}{6} \omega_{kkk} \partial_{xxx} + \frac{1}{2} \omega_{kkm} \partial_{xxz} + \frac{1}{2} \omega_{kmm} \partial_{xzz} + \frac{1}{6} \omega_{mmm} \partial_{zzz} \right\} A_\Psi - ikU A_\Psi, \end{aligned} \quad (2.54)$$

in which the subscripts on ω denote partial derivatives with respect to the horizontal and vertical wavenumbers k and m , respectively. The dispersion relation ω and its derivatives are summarized in Table 2.3.

The nonlinear Schrödinger equation for two-dimensional anelastic wavepackets (2.54) is similar in form to its Boussinesq counterpart, given by (2.42). In particular, the respective sets of braced terms have identical physical interpretations, and in both equations the nonlinear term represents the Doppler-shifting of the waves by their induced mean flow.

The linear part of (2.54) is identical to the linear part of the nonlinear Schrödinger equation derived by Shrira (1981) (c.f. equation 20 in that work). In particular, that equation

Dispersion relation and its derivatives	
$\omega = Nk/K$	$\omega_{kkk} = -3N(K^2 - k^2)(K^2 - 5k^2)/K^7$
$c_{g_x} = \omega_k = N(K^2 - k^2)/K^3$	$\omega_{kkm} = 3Nkm(3K^2 - 5k^2)/K^7$
$c_{g_z} = \omega_m = -Nkm/K^3$	$\omega_{kmm} = -N[K^2(3K^2 - 5k^2) - 5m^2(K^2 - 3k^2)]/K^7$
$\omega_{kk} = -3Nk(K^2 - k^2)/K^5$	$\omega_{mmm} = 3Nkm(3K^2 - 5m^2)/K^7$
$\omega_{km} = -Nm(K^2 - 3k^2)/K^5$	
$\omega_{mm} = -Nk(K^2 - 3m^2)/K^5$	

Table 2.3: Expressions for the linear dispersion relation, ω , and its derivatives up to third-order, for internal gravity waves in an anelastic gas. Here, $K^2 = k^2 + m^2 + 1/(4H_\rho^2)$ in which k and m are the horizontal and vertical wavenumbers, respectively, and H_ρ is the density scale height.

was derived for three-dimensional (horizontally, vertically, and spanwise localized) Boussinesq wavepackets in which dependence on the spanwise coordinate was significantly weaker than on x or z . The principal difference between (2.54) and equation (20) of Shrira is that the nonlinear terms in the latter are proportional to $A(\mathbf{c}_g \cdot \nabla A^*) - |A|^2 \mathbf{c}_g \cdot \nabla A$, in which the star denotes the complex conjugate of A . Conversely, in (2.54) the nonlinear term is proportional to UA , in which $U \propto |A|^2$ is given by (2.29). Tabaei and Akylas (2007) also derived a wavepacket evolution equation for two-dimensional wavepackets which, in the absence of modulations in the x -direction, reduced to a nonlinear Schrödinger equation (c.f. equations 66 and 72 in that work). Our equation (2.54) is similar to those of Tabaei and Akylas in that the nonlinearity arises through interactions between the waves and their induced mean flow. Like Shrira's equation (20), but unlike the nonlinear Schrödinger equation of Tabaei and Akylas, our equation (2.54) remains sensitive to modulations in the x -direction, although their effect is generally weaker than the effect of modulations in the z -direction.

If the horizontal extent of the wavepacket, σ_x , is taken to be arbitrarily large, the wavepacket becomes horizontally uniform and so all terms containing at least one x -derivative in (2.54) vanish. The linear part of the resulting equation is identical to the linear part of the nonlinear Schrödinger equation for one-dimensional anelastic wavepackets derived by DS11, which is reproduced in (1.8). The nonlinear part of (2.54) does not reduce to its one-dimensional analogue because the wave-induced mean flows are qualitatively different (Tabaei and Akylas, 2007; van den Bremer and Sutherland, 2018).

There are three key differences between our two-dimensional nonlinear Schrödinger equa-

tion and the one-dimensional nonlinear Schrödinger equation derived by DS11 for horizontally periodic, vertically localized wavepackets. Two-dimensional wavepackets can disperse in the horizontal and in the vertical, as expressed through terms containing derivatives with respect to x in (2.54), as opposed to dispersing in the vertical only, as is the case for waves strictly localized in the vertical. The wave-induced mean flow is qualitatively different: rather than being unidirectional and horizontally localized with maximum value spatially co-located with the peak in the amplitude function, in two dimensions the induced flow is positive on the leading flank of the wavepacket and negative on the trailing flank. Finally, with U being of $O(\alpha^2\epsilon)$ for two-dimensional wavepackets, the nonlinear (Doppler-shift) term in (2.54) balances dispersion terms with three spatial derivatives. For one-dimensional wavepackets U is of $O(\alpha^2)$, and so the Doppler-shift term in (1.8) balances the leading-order dispersion term, whereas the next-order dispersion term is balanced by the wave-induced mean flow shear term, as expressed through the term involving $\partial_z U$ in (1.8).

The coefficients in the nonlinear Schrödinger equation (2.54) allow us quantitatively to investigate the modulational instability of two-dimensional wavepackets (Whitham, 1974; Phillips, 1981). Mathematically, wavepackets are modulationally unstable if $kU\omega_{mm} < 0$. This condition is derived in Appendix B (see also Sutherland (2010, section 4.2.4) and Whitham (1974)). For one-dimensional wavepackets, $kU > 0$ and so modulational instability occurs only for waves having frequency less than that of waves with the fastest vertical group speed, for which $\omega_{mm} = 0$. For Boussinesq waves, the critical transition frequency is $\omega_* = \sqrt{2/3}N$ occurring at the critical vertical wavenumber $m_* = k/\sqrt{2}$. Two-dimensional wavepackets are always modulationally unstable because kU changes sign over the vertical extent of the wavepacket, consistent with the findings of Tabaei and Akylas (2007). In particular, where $kU\omega_{mm} < 0$, the waves accumulate, leading to relative amplitude growth, and where $kU\omega_{mm} > 0$, the waves spread, leading to relative amplitude decay. Whether the leading or trailing flank exhibits relative growth or decay is determined by the magnitude of the critical transition wavenumber, \tilde{m}_* relative to k , defined by (B.10), which is itself set by the condition $\omega_{mm} = 0$. For reference, (B.10) is

$$\tilde{m}_* = |m_*/k| := \frac{1}{\sqrt{2}} \left[1 + \frac{1}{4k^2 H_\rho^2} \right]^{1/2}.$$

If $|m/k| < \tilde{m}_*$, wave accumulation occurs on the leading flank (where $U(z, t) > 0$), while the trailing flank exhibits amplitude decay and vertical spreading, leading inevitably to the trailing flank running into the leading flank. Conversely, if $|m/k| > \tilde{m}_*$, the leading flank spreads vertically while the trailing flank accumulates.

Although typically weaker than vertical modulations, the wavepacket also exhibits modulational instability in the horizontal if $kU\omega_{kk} < 0$. This condition is derived in Appendix B. However, because $\omega_{kk} < 0 \forall m \in \mathbb{R}$, horizontal narrowing and amplitude growth or broadening and amplitude decay is determined by the sign of U . In particular, on the leading flank, where $U(z, t) > 0$, the wavepacket will narrow and the amplitude will grow, whereas on the trailing flank, where $U(z, t) < 0$, the amplitude will decay and the wavepacket will broaden. These effects are much less pronounced than the effects of vertical modulations. This is confirmed by the results of the weakly and fully nonlinear simulations presented in Chapter 4.

Chapter 3

Numerics

Along with the insights provided through the analysis of the governing equations in the previous chapter, numerical simulation is one of the primary means by which we seek to understand the dynamics of horizontally and vertically localized internal gravity wavepackets. Two types of simulations were conducted: “fully nonlinear” simulations, which solve a modification of the nonlinear equations of motion, and “weakly nonlinear” simulations, which solve the nonlinear Schrödinger equation (2.54). The methods of both types of simulations are detailed herein. The final section in this chapter presents the numerical methods that will be used to analyze quantitatively the results shown in Chapter 4.

The fully nonlinear code was provided by Dr. Bruce Sutherland. The core of this code uses the numerical algorithms of Press et al. (2007). I wrote the section of the code that diagnoses wave overturning for two-dimensional wavepackets (previously this part of the code was valid only for one-dimensional waves). The weakly nonlinear code was originally written by Ms. Hayley Dosser to numerically integrate (1.8) for her study of horizontally periodic, vertically localized weakly nonlinear anelastic wavepackets (Dosser, 2010; Dosser and Sutherland, 2011). I re-wrote each part of this code to numerically integrate (2.54), and I designed and wrote the subroutine that computes the wave-induced mean flow, $u^{(2)}(x, z, t)$. The core of this subroutine uses the fast Fourier transform algorithms of Press et al. (2007). Both the fully and weakly nonlinear codes are written in C. All simulations were run in serial on an Apple iMac using a 2.9 GHz Intel Core i5 processor. The average run time for the fully nonlinear simulations, using the parameters detailed below, was 95 hours; the average run time for the weakly nonlinear simulations, using the parameters detailed below, was 18 hours.

3.1 Fully Nonlinear Anelastic Solver

The fully nonlinear anelastic code solved the coupled momentum equations for vorticity and vertical displacement. For numerical stability, all fields explicitly evolved by the code were scaled to remove anelastic effects. In this way the exponential amplification of numerical noise in the vertical extremes of the domain was avoided. In the present discussion, the subscript s will distinguish the “scaled” fields evolved by the code from the actual anelastic fields. The relationships between the scaled and actual fields are given by

$$(\xi_s, u_s, w_s, \zeta_s) = (\xi, u, w, \zeta)e^{-z/2H_\rho} \quad \text{and} \quad \Psi_s = \Psi e^{z/2H_\rho}. \quad (3.1a,b)$$

Without explicitly separating the mean and fluctuation components of the total vorticity and vertical displacement fields, their respective fully nonlinear evolution equations are given nondimensionally by

$$\frac{\partial \zeta_s}{\partial t} = -e^{z/2H_\rho} \left[\mathbf{u}_s \cdot \nabla \zeta_s + \frac{3}{2H_\rho} w_s \zeta_s \right] + N^2 \frac{\partial \xi_s}{\partial x} + C_\zeta \mathcal{D} \zeta_s; \quad (3.2)$$

$$\frac{\partial \xi_s}{\partial t} = -e^{z/2H_\rho} \left[\mathbf{u}_s \cdot \nabla \xi_s + \frac{1}{H^*} w_s \xi_s \right] + w_s + C_\xi \mathcal{D} \xi_s, \quad (3.3)$$

where we have defined $\frac{1}{H^*} := \frac{1}{2H_\rho} + \frac{1}{H_\theta}$ for notational ease. The effects of viscosity and thermal diffusion are included via the terms $C_\zeta \mathcal{D} \zeta_s$ and $C_\xi \mathcal{D} \xi_s$. Although these terms were excluded in the derivations of the wave-induced mean flow and the nonlinear Schrödinger equations, their purpose here is to assist with numerical stability by damping small-scale noise, while not acting to attenuate the waves. For all simulations, $C_\zeta = C_\xi = 10^{-3} N k^{-2}$. The operator \mathcal{D} applied diffusive effects uniformly at all vertical levels, to all horizontal wavenumbers greater than a specified viscous diffusion threshold wavenumber, k_d . For all simulations, the viscous diffusion threshold wavenumber was set to $k_d = (3/2)k_w = 384$, in which $k_w = 256$ is the specified number of horizontal wavelengths of waves within the wavepacket that can exist in the domain.

3.1.1 Discretization and Grid Generation

The relative scales for time and domain size were set by fixing $N = 1$ and $k = 1$, respectively. The fully nonlinear code solved (3.2) and (3.3) in a vertically real, horizontally spectral do-

main. This domain used no-slip boundary conditions on the lower and upper boundaries, and was horizontally periodic. The vertical domain was set to $-30 \leq kz \leq 15kH_\rho$ for all simulations and was discretized by $n_z = 1024$ grid points for simulations using $H_\rho = 10k^{-1}$, and by $n_z = 512$ grid points for simulations using $H_\rho = 5k^{-1}$. Alternatively, the width of the domain, L_x , was set according to $k_w := L_x/(2\pi/k)$. All simulations were conducted using $k_w = 256$, hence $L_x = 2\pi k_w/k$ and so the horizontal domain in real space was $|kx| \leq 804.3$. In Fourier space this domain was discretized by 8192 horizontal wavenumbers.

Upon horizontally Fourier decomposing (3.2) and (3.3), the partial differential operators involving x are Fourier decomposed according to

$$\frac{\partial}{\partial x} \rightarrow -ik_n, \quad (3.4)$$

with k_n denoting the n -th horizontal wavenumber in the Fourier domain.

3.1.2 Initialization

The horizontal component of the scaled mass-streamfunction, denoted here by the superscript \perp , was initialized in real space according to

$$\Psi_s^\perp(x, 0) = \rho_0 \frac{\omega}{k} A_{\xi_0} e^{-(x-x_0)^2/2\sigma_x^2} \cos(k(x-x_0)), \quad (3.5)$$

where A_{ξ_0} is the initial vertical displacement amplitude, σ_x is the initial horizontal extent of the wavepacket, and the phase has been chosen so that (3.5) is purely real initially. For generality the initial horizontal position of the wavepacket, x_0 , can be offset from the origin. However, for the simulations conducted for this thesis we have always set $x_0 = 0$. The polarization relations from linear theory, given in the centre column of Table 2.1, were used to initialize the mass-streamfunction amplitude, $A_{\Psi_0} = |\rho_0(-\omega/k)A_{\xi_0}|$. As a more physically intuitive quantity, the initial vertical displacement amplitude was specified in favour of the mass-streamfunction amplitude. For all simulations, we set $A_{\xi_0} = 0.05k^{-1}$ so that the wavepackets would be of relatively small amplitude initially, yet be large enough to grow to moderately large amplitude not long after the start of the simulations.

The horizontal component of the scaled mass-streamfunction field, given by (3.5), was then horizontally fast Fourier transformed, with the result being used to initialize the vertical

component of the scaled mass-streamfunction, given by

$$\widehat{\Psi}_s(z, 0) = \widehat{\Psi}_s^\perp e^{-(z-z_0)^2/2\sigma_z^2} e^{im(z-z_0)}, \quad (3.6)$$

where the caret denotes that the field has been horizontally fast Fourier transformed, thus the horizontal component depends on the discrete horizontal wavenumbers k_n . The initial vertical extent of the wavepacket is denoted by σ_z , and the initial vertical position of the wavepacket, z_0 , was always set to $z_0 = 0$. Together, equations (3.5) and (3.6) correspond to the real initial scaled mass-streamfunction

$$\Psi_s(x, z, 0) = A_{\Psi_0} e^{-x^2/2\sigma_x^2 - z^2/2\sigma_z^2} \cos(kx + mz).$$

The scaled vorticity field was initialized through derivatives of the scaled mass-streamfunction using the horizontal Fourier decomposition of relation (2.46), the result of which is

$$\widehat{\zeta}_s(z, 0) = k_n^2 \widehat{\Psi}_s - \frac{\partial^2 \widehat{\Psi}_s}{\partial z^2} - \frac{1}{H_\rho} \frac{\partial \widehat{\Psi}_s}{\partial z}.$$

Finally the scaled vertical displacement field was initialized using the polarization relations from linear theory, given in the centre column of Table 2.1, that is,

$$\widehat{\xi}_s(z, 0) = -\frac{k}{\omega} \frac{\partial \widehat{\Psi}_s}{\partial z}.$$

Uniform stratification was set by the density profile $\bar{\rho} = \rho_0 e^{-z/H_\rho}$. For generality the code was designed such that an arbitrary background flow $u_0(z)$ could be specified. However, in all simulations conducted for this thesis, we set $u_0(z) \equiv 0$.

3.1.2.1 Wave-Induced Mean Flow

Although it is physically realistic to include the initial horizontal wave-induced flow field, $u^{(2)}(x, z, 0)$, when initializing the fully nonlinear simulations, doing so is impractical because very large domains are required in order to accurately compute the induced flow. Despite this, the induced flow begins to develop outwards and downwards from the wavepacket shortly after initialization. Furthermore, the weakly nonlinear evolution of the wavepacket is dominated by the interactions between the waves and their induced mean flow only over the extent of

the wavepacket. We denote by t_σ the time scale over which the induced flow develops over the horizontal extent of the wavepacket. In particular, we predict that t_σ is given by the ratio of the horizontal wavepacket extent, σ_x , and the horizontal group speed, \bar{c}_{g_x} , of the induced long wave. Denoting by over-bars quantities pertaining to long waves, vdBS14 (c.f. section III C in that work) provide the relationships

$$\bar{\omega} = \frac{N\bar{k}}{|\bar{m}|}, \quad |\bar{m}| = \frac{2\pi}{\sigma_z}, \quad \bar{c}_{p_x} = \frac{\bar{\omega}}{\bar{k}} \approx \bar{c}_{g_x}. \quad (3.7a,b,c)$$

Here, $\bar{\omega}$ is the dispersion relation for long waves; $|\bar{m}|$ is the magnitude of the vertical wavenumber, in which we have assumed the vertical wavelength of the long wave corresponds to the vertical extent of the wavepacket; and \bar{c}_{p_x} is the horizontal phase speed for long waves, which is approximately equal to the horizontal group speed for long waves. Hence,

$$t_\sigma = \frac{2\pi}{\bar{c}_{g_x}} = \frac{2\pi\sigma_x}{N\sigma_z}. \quad (3.8)$$

For horizontally and vertically localized wavepackets, for which $\sigma_x \sim \sigma_z$, (3.8) shows that the induced flow became well developed over one buoyancy period. As such, the long-time behaviour of the wavepackets was negligibly affected by the exclusion of the initial wave-induced mean flow upon initializing the simulations.

3.1.3 Advection and Temporal Advancement

For a given $\widehat{\zeta}_s$, the relationship (2.46), in which the operator was horizontally Fourier decomposed according to (3.4), was inverted to obtain the $\widehat{\Psi}_s$ field. From this, the code constructed the scaled horizontal velocity field from

$$\widehat{u} = -\frac{1}{\bar{\rho}} \frac{\partial \widehat{\Psi}}{\partial z} \quad \Rightarrow \quad \widehat{u}_s = -\frac{1}{\rho_0} \left(\frac{\partial \widehat{\Psi}_s}{\partial z} - \frac{1}{2H_\rho} \widehat{\Psi}_s \right).$$

The horizontal vorticity advection term, $u_s \partial_x \zeta_s$ in (3.2), was then computed by horizontally inverse fast Fourier transforming the \widehat{u}_s and $\widehat{\partial_x \zeta}_s$ fields, multiplying the results in real space, and horizontally fast Fourier transforming the product. The vertical vorticity advection term, $w_s \partial_z \zeta_s$, was similarly computed using

$$\widehat{w} = \frac{1}{\bar{\rho}} \frac{\partial \widehat{\Psi}}{\partial x} \quad \Rightarrow \quad \widehat{w}_s = -\frac{1}{\rho_0} i k_n \widehat{\Psi}_s \quad (3.9)$$

and the $\partial_z \widehat{\zeta}_s$ field. The product of vertical velocity and vorticity, $\frac{3}{2H_\rho} w_s \zeta_s$, was likewise computed. The resulting term and the vorticity advection terms were then summed and multiplied by $-e^{z/2H_\rho}$ to construct the bracketed term in equation (3.2). The linear baroclinic term, $N^2 \partial_x \xi_s$, was added to the result using

$$N^2 \frac{\partial \widehat{\xi}_s}{\partial x} = -ik_n N^2 \widehat{\xi}_s.$$

The code proceeded to determine the advection of scaled vertical displacement, $\mathbf{u}_s \cdot \nabla \zeta_s$ in (3.3), using the horizontal fast Fourier transform method described above. The $\frac{1}{H^*} w_s \xi_s$ term was added to the result and the sum of these terms was multiplied by $-e^{z/2H_\rho}$ to construct the bracketed term in equation (3.3). Vertical velocity was added to this using the rightmost relation in (3.9).

Finally the code computed the diffusion terms using

$$\mathcal{D} \widehat{\zeta}_s = -k_n^2 \widehat{\zeta}_s + \frac{\partial^2 \widehat{\zeta}_s}{\partial z^2} \quad \text{and} \quad \mathcal{D} \widehat{\xi}_s = -k_n^2 \widehat{\xi}_s + \frac{\partial^2 \widehat{\xi}_s}{\partial z^2},$$

in which \mathcal{D} applied only to the horizontal wavenumbers $k_n > k_d = 384$. The derivatives with respect to z employed a centred, second-order finite difference scheme.

Time stepping was performed using a leapfrog scheme. Explicitly, the scaled vorticity and vertical displacement fields were advanced according to

$$\begin{aligned} \widehat{\zeta}_s(z, t + \Delta t) &= \widehat{\zeta}_s(z, t - \Delta t) + 2\Delta t \dot{\widehat{\zeta}}_s(z, t); \\ \widehat{\xi}_s(z, t + \Delta t) &= \widehat{\xi}_s(z, t - \Delta t) + 2\Delta t \dot{\widehat{\xi}}_s(z, t), \end{aligned}$$

in which $\dot{\widehat{\zeta}}_s$ and $\dot{\widehat{\xi}}_s$ are the right-hand sides of (3.2) and (3.3), respectively. In order to avoid numerical ‘‘splitting’’ errors, every 20 time steps the vorticity and vertical displacement fields were advanced by $-\Delta t$ and the resulting fields were averaged with those from the previous time step (see also Durran (2010, section 2.4.2)). This procedure is referred to as an ‘‘Euler backstep’’. For all fully nonlinear simulations, time was advanced by a small increment of $\Delta t = 0.0125N^{-1}$.

3.2 Weakly Nonlinear Anelastic Solver

The weakly nonlinear anelastic code solved the nonlinear Schrödinger equation (2.54) for the mass-streamfunction amplitude envelope. Because the anelastic part of the field was removed as a consequence of the derivation (except as it appeared in the wave-induced mean flow), the precautions taken to ensure the numerical stability of the fully nonlinear code are not necessary here.

3.2.1 Grid Generation

Equation (2.54) was solved on a finite difference grid. The horizontal domain was set by integer multiples of the horizontal domain used for the fully nonlinear simulations. In particular, for all weakly nonlinear simulations, the horizontal domain was set to $|kx| \leq 2\pi k_w \approx 1608.6$, with $k_w = 256$ being the number of wavelengths in the horizontal domain of the fully nonlinear simulations. Such a width was necessary to ensure that the long waves induced by the wavepacket were of negligibly small amplitude near the left and right boundaries. Likewise, the vertical domain was chosen to be deep enough that the downward-propagating induced long waves were of negligible amplitude at the lower boundary, yet tall enough that the wavepacket could propagate vertically well above its initial position without interacting with the upper boundary. The need for such a wide, deep domain is illustrated in Fig. 2.1a. In particular, for simulations using $H_\rho = 10k^{-1}$ the vertical domain was set to $-250 \leq kz \leq 150$, and for simulations using $H_\rho = 5k^{-1}$ the vertical domain was set to $-325 \leq kz \leq 75$. The horizontal and vertical domains were discretized by $n_x = 2049$ and $n_z = 513$ grid points, respectively.

As will be detailed in §3.2.4, the induced flow field, $u^{(2)}(x, z, t)$, was computed in a doubly periodic Fourier domain, with only the profile $U(z, t) = u^{(2)}(x = c_{g_x}t, z, t)$ used in (2.54). The horizontal Fourier space domain contained $1 + (n_x - 1)/2 = 1025$ evenly spaced horizontal wavenumbers, $\kappa_n \in [0, \pi n_x/L_x]$, separated by an increment of size $\Delta\kappa = 2\pi/L_x$. The vertical Fourier space domain contained $n_z = 513$ evenly spaced vertical wavenumbers, $\mu_m \in [-\pi n_z/L_z, \pi n_z/L_z]$, separated by an increment of size $\Delta\mu = 2\pi/L_z$. Here, $L_z = 400k^{-1}$ is the total height of the vertical domain.

3.2.2 Initialization

All weakly nonlinear simulations were initialized with a bivariate Gaussian vertical displacement amplitude function, given explicitly by

$$A_\xi(x, z, 0) = A_{\xi_0} e^{-x^2/2\sigma_x^2 - z^2/2\sigma_z^2}, \quad (3.10)$$

in which σ_x and σ_z are the horizontal and vertical wavepacket extents, respectively. In the weakly nonlinear simulations, as in their fully nonlinear counterparts, the initial vertical displacement amplitude was specified in favour of the mass-streamfunction amplitude. The value of $A_{\xi_0} = 0.05k^{-1}$ was chosen so that the results of the weakly nonlinear simulations could be compared to the results of the fully nonlinear simulations. The polarization relations from linear theory, given in the centre column in Table 2.1, were used to convert the initial vertical displacement amplitude to the mass-streamfunction amplitude,

$$A_\Psi(x, z, 0) = -\rho_0 \frac{\omega}{k} A_\xi(x, z, 0).$$

3.2.3 Spatial and Temporal Advancement

All spatial derivatives in (2.54) were approximated by centred second-order finite differences. Expressions for each finite difference scheme, including the associated error terms, were derived by taking linear combinations of the Taylor series of A expanded in x and z , which was truncated at fifth-order. The details of this procedure are included in Appendix C.

For any time step, the linear part of the right-hand side of (2.54) was computed using the finite difference schemes detailed in Appendix C. The nondimensionalized coefficients multiplying each term are included in Table 3.1. Separately, the wave-induced mean flow U was computed using the method described in §3.2.4, and the result was added to the linear part.

The solution was advanced in time using the leapfrog scheme as described in §3.1.3. An Euler backstep was likewise taken every 20 time steps. For all weakly nonlinear simulations using $H_\rho = 10k^{-1}$, time was advanced by a small increment of $\Delta t = 0.005N^{-1}$; for all weakly nonlinear numerical simulations using $H_\rho = 5k^{-1}$, time was advanced by $\Delta t = 0.0025N^{-1}$.

m/k	ω/N	$c_{g_x} \frac{k}{N}$	$c_{g_z} \frac{k}{N}$	$\omega_{kk} \frac{k^2}{N}$	$\omega_{km} \frac{k^2}{N}$
-0.4	0.928	0.130	0.319	-0.335	-0.504
-0.7	0.819	0.270	0.384	-0.543	-0.388
-1.4	0.581	0.385	0.275	-0.390	-0.004
m/k	$\omega_{mm} \frac{k^2}{N}$	$\omega_{kkk} \frac{k^3}{N}$	$\omega_{kkm} \frac{k^3}{N}$	$\omega_{kmm} \frac{k^3}{N}$	$\omega_{mmm} \frac{k^3}{N}$
-0.4	-0.468	1.105	1.072	0.170	-1.904
-0.7	-0.008	1.126	0.270	-0.717	-1.048
-1.4	0.193	0.268	-0.365	-0.266	0.086

Table 3.1: Nondimensional frequency, ω/N , and values of the coefficients in the anelastic nonlinear Schrödinger equation (2.54), using the range of relative vertical wavenumbers, m/k , to be considered in the weakly nonlinear simulations. All values were computed using $H_\rho = 10k^{-1}$.

3.2.4 Computation of the Wave-Induced Mean Flow

For computational convenience, in the weakly nonlinear code the wave-induced mean flow at each time step was computed from a modification of equation (2.27) and the fact that $u^{(2)} = -\frac{1}{\rho} \partial_z \Psi^{(2)}$. Because the amplitude function used in (2.27) was that of vertical displacement, the polarization relations from linear theory, given in the centre column of Table 2.1, were used to re-cast the right-hand side of (2.27) in terms of mass-streamfunction amplitude. Explicitly,

$$\widehat{\rho u^{(2)}} = -\widehat{\partial_z \Psi^{(2)}} = -i\mu \widehat{\Psi^{(2)}} = \frac{1}{2} \rho_0 \frac{k^2 m^2}{NK^3} \frac{\mu^4 |A_\Psi|^2}{2C(\mu)} \left[\frac{1}{\kappa + C(\mu)} - \frac{1}{\kappa - C(\mu)} \right]. \quad (3.11)$$

Here, the function $C(\mu)$ is given by (A.2). When evaluating $C(\mu)$, it was necessary to choose the branch cut corresponding to induced long waves that propagate outwards and downwards from the translating wavepacket (Bretherton, 1969). In (A.2) we deliberately re-express the function Φ as

$$\Phi = \pm \frac{1}{2} \tan^{-1}(1/H_\rho |\mu|) \quad (3.12)$$

in order to give us maximum liberty in choosing the appropriate branch cut. In particular, the branch cut corresponding to outgoing waves is that for which the \pm sign in (3.12) is equal to $\text{sgn}(\mu)$.

During initialization, the fixed complex valued matrix $M(\kappa_n, \mu_m)$ was constructed into which was mapped the κ - and μ -dependent part of the right-hand side of (3.11). Explicitly,

$$M(\kappa_n, \mu_m) = \frac{\mu_m^4}{2C(\mu_m)} \left[\frac{1}{\kappa_n + C(\mu_m)} - \frac{1}{\kappa_n - C(\mu_m)} \right].$$

At any time step t_j , the induced flow field, $u^{(2)}(x, z, t_j)$, was computed by first horizontally and vertically fast Fourier transforming the squared modulus of the mass-streamfunction amplitude. The result was multiplied entry-wise into M , and the product was horizontally and vertically inverse fast Fourier transformed and multiplied by the leading coefficient $\frac{1}{2}\rho_0 k^2 m^2 N^{-1} K^{-3}$, thus obtaining the induced momentum field, that is, the left-hand side of (3.11) in real space. Finally this was multiplied by $1/\bar{\rho}$, from which the wave-induced mean flow followed directly via $U(z, t_j) = u^{(2)}(\tilde{x} = 0, z, t_j)$, which amounts to extracting a vertical profile through the horizontal centre of the translating wavepacket. Linear theory was used to determine the point at which $\tilde{x} = 0$ (equivalently, the point at which $x = c_{gx} t_j$). A simple weighted mean was used to interpolate the actual value of the wave-induced mean flow should x have been situated between two nodes in the discretized domain.

3.3 Quantitative Analysis Methods

In order to gain a more quantitative understanding of the weakly nonlinear evolution of two-dimensional wavepackets, here we introduce the numerical tools used to examine the numerical results presented in the next chapter.

The normalized L^2 -norm of the wave-induced momentum through the horizontal centre of a translating wavepacket is defined by

$$\|\widetilde{M}(t)\| := \frac{\|\bar{\rho}U(z, t)\|_{L^2}}{\|\bar{\rho}U(z, t_*)\|_{L^2}} = \frac{\left[\int_{z_{\min}}^{z_{\max}} \bar{\rho}^2 U^2(z, t) dz \right]^{1/2}}{\left[\int_{z_{\min}}^{z_{\max}} \bar{\rho}^2 U^2(z, t_*) dz \right]^{1/2}}, \quad (3.13)$$

in which $\bar{\rho}U(z, t)$ is the wave-induced momentum. From the profiles of local wave-induced momentum output by the weakly and fully nonlinear simulations, (3.13) will be used to generate time series of wave-induced momentum. The composite Simpson's rule was used to compute the integrals on the right-hand side of (3.13) in practice (e.g. see Allen and Isaacson, 1998). The choices of particular values of t_* used for the normalization factor, $\|\bar{\rho}U(z, t_*)\|_{L^2}$, were based on the type of simulation being examined. For the weakly nonlinear simulations, the normalization factor used the $t_* = 0$ profile of wave-induced mean flow predicted by setting $\tilde{x} = 0$ in (A.16). For the fully nonlinear simulations, the normalization factor used the

resolved wave-induced momentum profile at $t_* = t_\sigma$, with t_σ given by (3.8). This corresponds to the time at which the induced long wave was expected to be fully developed over the horizontal extent of the wavepacket.

To compare the results of our simulations with those of one-dimensional wavepackets, it is useful to estimate the height and time at which weakly nonlinear effects become significant. Following the approach of DS11, we assume weakly nonlinear effects become significant when the magnitude of the weakly nonlinear term in the nonlinear Schrödinger equation (2.54) approximately equals the magnitude of the smallest of the linear advection terms in (2.54). Explicitly, this is the condition

$$|ikUA_\Psi| = \min\{|c_{g_x}\partial_x A_\Psi|, |c_{g_z}\partial_z A_\Psi|\}. \quad (3.14)$$

For one-dimensional wavepackets, $|\partial_z A_\Psi/A_\Psi| \sim 1/\sigma_z$. Similarly, for horizontally and vertically localized wavepackets, for which $\sigma_x \sim \sigma_z$, it follows that $|\partial_x A_\Psi/A_\Psi| \sim 1/\sigma_x$. Hence (3.14) simplifies to the condition $|U| \sim \epsilon \min\{|c_{g_x}|, |c_{g_z}|\}$. Van den Bremer and Sutherland (2018) derived an asymptotic approximation for the maximum horizontal velocity of the long wave induced by a fully three dimensional Boussinesq wavepacket (c.f. equation 3.27 in that work). We somewhat heuristically adapt their result to spanwise-uniform anelastic wavepackets by multiplying their result by $\bar{\rho}/\rho_0 = e^{-z/H_\rho}$, and replacing all instances of $|\mathbf{k}|$ in their result with its anelastic correction, K , to predict

$$\max_{\bar{z}} U \Big|_{\bar{x}=0} = \frac{1}{2} NK A_0^2 \left[1.45 \frac{k^2 |m|}{K^3} \epsilon \frac{\sigma_x^2}{\sigma_z^2} e^{z/H_\rho} \right]. \quad (3.15)$$

The height, z_Δ , at which we expect weakly nonlinear effects to become significant is thus predicted by equating the right-hand side of (3.15) with $\epsilon \min\{|c_{g_x}|, |c_{g_z}|\} = \epsilon \frac{N}{K^3} \min\{K^2 - k^2, |km|\}$, the result of which is re-arranged to read

$$\frac{z_\Delta}{H_\rho} = \ln \left(\frac{1.38\sigma_z^2}{A_0^2 k^2 |m| K \sigma_x^2} \right) + \begin{cases} \ln(K^2 - k^2), & |m| + 1/(4|m|H_\rho^2) < |k|; \\ \ln |km|, & |m| + 1/(4|m|H_\rho^2) > |k|. \end{cases} \quad (3.16)$$

Assuming the vertical phase speed of the induced long wave approximately equals the vertical group speed of the wavepacket, as expressed by (3.7c), the time, t_Δ , at which weakly nonlinear

effects are expected to become significant is approximately

$$t_{\Delta} = \frac{z_{\Delta}}{c_{g_z}}. \quad (3.17)$$

In the fully nonlinear simulations, wave overturning was diagnosed by computing the minimum value of the total squared buoyancy frequency, $N_T^2 = N^2 + \Delta N^2$, in which the fluctuation component, ΔN^2 , is defined by

$$\Delta N^2 := \frac{g}{\bar{\theta}} \frac{\partial \theta}{\partial z} \approx -N^2 \frac{\partial \xi}{\partial z}.$$

Wave overturning occurs where $N_T^2 < 0$. The fully nonlinear simulations computed ΔN^2 at every time step by first horizontally inverse fast Fourier transforming the scaled vertical displacement field, $\widehat{\xi}_s$, and multiplying the result by $e^{z/2H_{\rho}}$ to obtain the actual vertical displacement field, ξ . A second-order centred finite difference scheme was used to approximate $\partial \xi / \partial z$, the result of which was then used to compute N_T^2 . The time of wave overturning, t_b , was taken to be the first time at which $\min N_T^2 < 0$ was satisfied. The corresponding vertical location, z_b , at which $\min N_T^2 < 0$ was taken to be the location of wave overturning.

Using linear anelastic theory, the waves are predicted to overturn where $|\partial \xi / \partial z| = 1$. Explicitly, for a plane wave with vertical displacement field given by $\xi = A_{\xi_0} e^{i(kx + mz - \omega t)} e^{z/2H_{\rho}}$, the linear theory overturning condition corresponds to a predicted overturning height, $z_{b,L}$, given nondimensionally by

$$\frac{z_{b,L}}{H_{\rho}} = 2 \ln \left(\frac{1}{A_{\xi_0} |m|} \left[1 + \frac{1}{4m^2 H_{\rho}^2} \right]^{-1/2} \right). \quad (3.18)$$

Chapter 4

Results and Comparison

In this chapter we compare the results of the weakly and fully nonlinear simulations. In each simulation the buoyancy frequency N and horizontal wavenumber k were fixed. Our primary focus is on bivariate Gaussian wavepackets with horizontal and vertical extents $\sigma_x = 10k^{-1}$ and $\sigma_z = 10k^{-1}$, respectively, in an atmosphere with density scale height $H_\rho = 10k^{-1}$. However, simulations were also performed setting $\sigma_x = 40k^{-1}$ and $H_\rho = 5k^{-1}$, and using combinations of these parameter values. The range of vertical wavenumbers spanning $-0.4k$, $-0.7k$, and $-1.4k$ corresponds to modulationally unstable, marginally unstable, and modulationally stable one-dimensional wavepackets studied by DS11. In two dimensions, the qualitatively different structure of the wave-induced mean flow means that all the vertical wavenumbers in this range correspond to modulationally unstable wavepackets, as shown and discussed below.

4.1 Weakly Nonlinear Simulations

The weakly nonlinear evolution of a Gaussian wavepacket initialized using (3.10) with $A_{\xi_0} = 0.05k^{-1}$, $m = -0.4k$, $\sigma_x = \sigma_z = 10k^{-1}$, and $H_\rho = 10k^{-1}$ is shown at four times in Fig. 4.1. The times shown span the wavepacket's evolution from early to very late times. The leftmost column shows the actual vertical displacement field, ξ ; the centre-left column shows the modulus of the vertical displacement amplitude function, $|A_\xi|$; the centre-right column shows the wave-induced momentum field, $\bar{\rho}u^{(2)}$; and the rightmost column shows vertical profiles of the wave-induced momentum through the horizontal centres of their corresponding wavepackets, $\bar{\rho}U$.

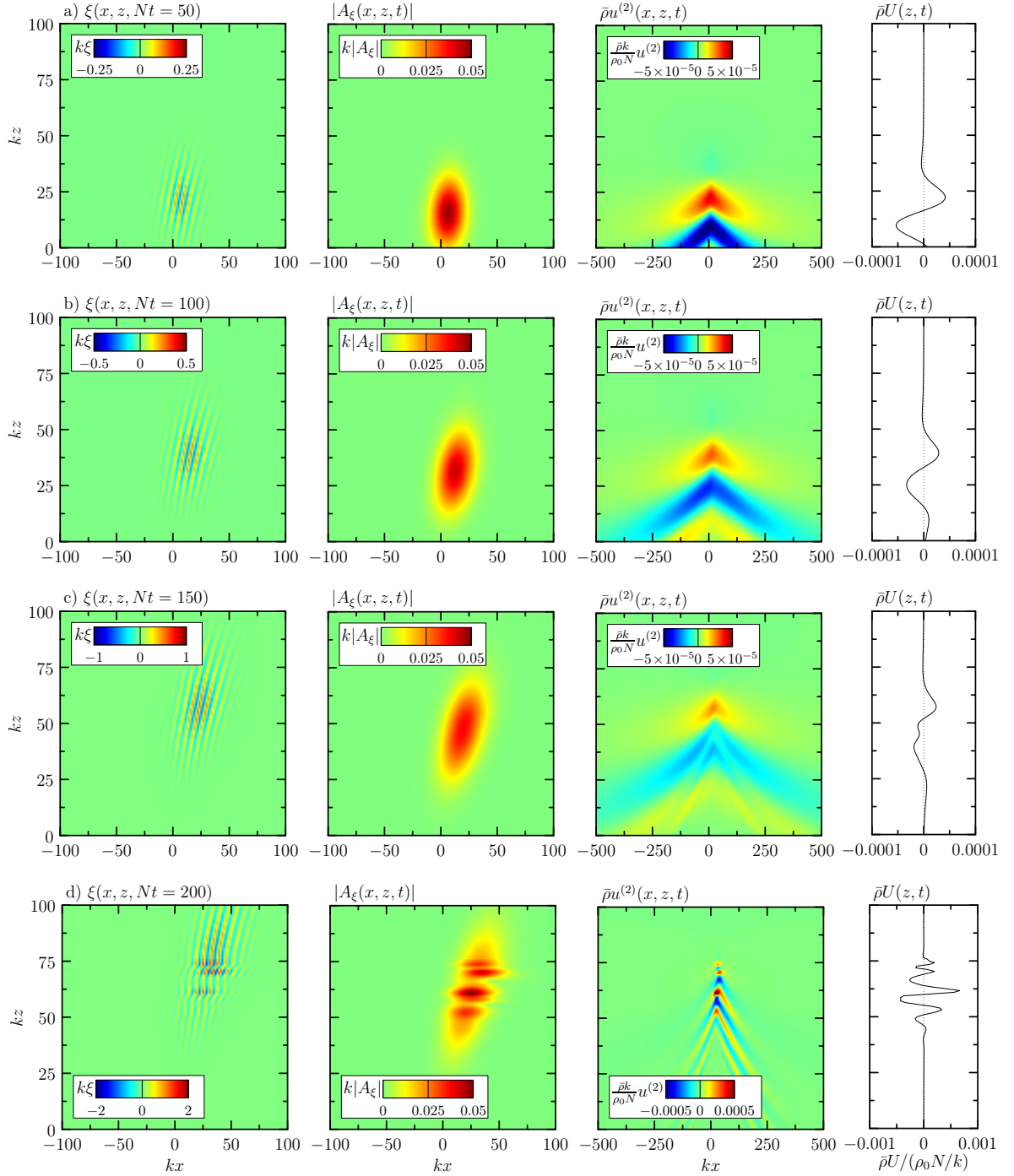


Figure 4.1: Snapshots of the evolution of a weakly nonlinear Gaussian wavepacket initialized using (3.10) with $A_{\xi_0} = 0.05k^{-1}$, $m = -0.4k$, and $\sigma_x = \sigma_z = 10k^{-1}$ as it propagates upward through an atmosphere with density scale height $H_\rho = 10k^{-1}$ at times t equal to (a) $50N^{-1}$, (b) $100N^{-1}$, (c) $150N^{-1}$, and (d) $200N^{-1}$. The leftmost column shows the actual vertical displacement field; the centre-left column shows the modulus of the vertical displacement amplitude envelope; the centre-right column shows the horizontal wave-induced momentum field; and the rightmost column shows vertical profiles of the wave-induced momentum through the horizontal centre of the translating wavepacket. Note that the horizontal axis limits in the rightmost panel of (d) are an order of magnitude larger than those in the corresponding panels in (a) – (c), as is the colour bar in the centre-right panel of (d).

At $t = 50N^{-1}$ (Fig. 4.1a), the amplitude envelope has changed little from its initial Gaussian shape. At this early time in its evolution, the wavepacket has translated upward and rightward according to linear theory. This is evident in part by the small relative discrepancy, δ_c , between the observed and predicted locations of the wavepacket envelope's peak amplitude, defined by

$$\delta_c := \left(\frac{x_{\text{peak}} - c_{g_x} t}{\sigma_x}, \frac{z_{\text{peak}} - c_{g_z} t}{\sigma_z} \right), \quad (4.1)$$

in which $(x_{\text{peak}}, z_{\text{peak}})$ is the location of the observed maximum value of the amplitude envelope. At this time (Fig. 4.1a), $\delta_c|_{t=50N^{-1}} \approx -(0.02, 0.03)$, indicating that the peak amplitude is very slightly below and to the left of the location predicted by linear theory. The induced momentum field, shown in the centre-right panel in Fig. 4.1a, has translated upward and rightward with the wavepacket, and is symmetric about $\tilde{x} = 0$. The profile of induced momentum through the centre of the wavepacket has translated vertically with the wavepacket. The flow is nearly symmetric about the vertical centre of the wavepacket, with positive flow on the leading flank and negative flow on the trailing flank.

Fig. 4.1b shows the wavepacket evolution at $t = 100N^{-1}$. Linear dispersion has caused the wavepacket amplitude envelope to broaden horizontally and vertically, and the peak amplitude has decreased accordingly. The vertical displacement amplitude envelope has 'tilted' clockwise somewhat. This will be shown later to be an effect owing to oblique dispersion terms, that is, those terms in the nonlinear Schrödinger equation (2.54) whose coefficients have mixed k - and m -derivatives of ω . The slight decrease in the peak value of the amplitude envelope is likewise observed in the magnitude of the wave-induced momentum, comparing the rightmost panels of Fig. 4.1b and Fig. 4.1a.

The results at this time suggest that weakly nonlinear effects have not yet begun significantly to affect the wavepacket's evolution, in contrast to the results at this time for one-dimensional anelastic wavepackets (DS11). The relative delay in the onset of nonlinear effects is due to the wave-induced mean flow, which arises at $O(\alpha^2\epsilon)$ for two-dimensional waves, as opposed to at $O(\alpha^2)$ for one-dimensional waves. Thus the waves must grow to relatively larger amplitude, which takes more time as they propagate to correspondingly higher altitudes.

At $t = 150N^{-1}$ (Fig. 4.1c), linear dispersion has caused the wavepacket amplitude to con-

tinue decreasing in peak value, and oblique dispersion in particular has caused the amplitude envelope to continue its clockwise ‘tilt’. Consequently, the maximum vertical displacement at this time (Fig. 4.1c) is $\xi \approx 0.54k^{-1}$, just over 60% of the corresponding value of $\xi \approx 0.85k^{-1}$ for one-dimensional wavepackets (DS11). The vertical displacement field of the two-dimensional wavepacket achieved this value at $t \approx 178N^{-1}$ (not shown), over four buoyancy periods later. Weakly nonlinear effects have begun to affect the wavepacket. This is seen in the wave-induced momentum field, which now exhibits a slight horizontal asymmetry manifesting as slightly larger magnitudes where $\tilde{x} < 0$. A second bow wake-like structure is emerging below the original long wave at a more acute angle to the vertical than the initial long wave. Associated with this is a vertical asymmetry in the centreline wave-induced momentum profile.

At $t = 200N^{-1}$ weakly nonlinear effects dominate the wavepacket evolution, and have altered the waves to a significant degree. Phase lines in the vertical displacement field, shown in the leftmost panel of Fig. 4.1d, have tilted strongly to the vertical, with some phase lines appearing to tilt opposite their initial orientation. The vertical displacement amplitude envelope no longer resembles a Gaussian, being now formed of a group of localized peaks. As a measure of the departure from linear theory of the location of the wavepacket’s peak value, the use of the relative discrepancy, $\delta_c|_{t=200N^{-1}} \approx -(0.08, 0.29)$, is rendered questionable. However, the maximum value of the amplitude has increased to $|A_\xi|_{\max} \approx 0.05k^{-1}$ after a period of steady decrease throughout the earlier times in its evolution (Figs. 4.1a,b,c). Similarly, the peak values of the induced momentum field and centreline wave-induced momentum have grown by an order of magnitude, indicating that weakly nonlinear effects developed rapidly between times $t = 150N^{-1}$ and $t = 200N^{-1}$. The induced long waves are oriented more acutely to the vertical than at previous times, and the induced flow is seen to have degenerated into a series of positive and negative jets. Diagnostics presented later will show that the wavepacket is overturning at this time.

The weakly nonlinear evolution of a Gaussian wavepacket initialized using (3.10) with $A_{\xi_0} = 0.05k^{-1}$, $m = -0.7k$, $\sigma_x = \sigma_z = 10k^{-1}$, and $H_\rho = 10k^{-1}$ is shown at four times in Fig. 4.2. The respective columns in Fig. 4.2 correspond to the columns in Fig. 4.1. Having a relative vertical wavenumber of $m = -0.7k$ means this wavepacket translates vertically at the fastest vertical group speed. Furthermore, waves having this relative vertical wavenumber are

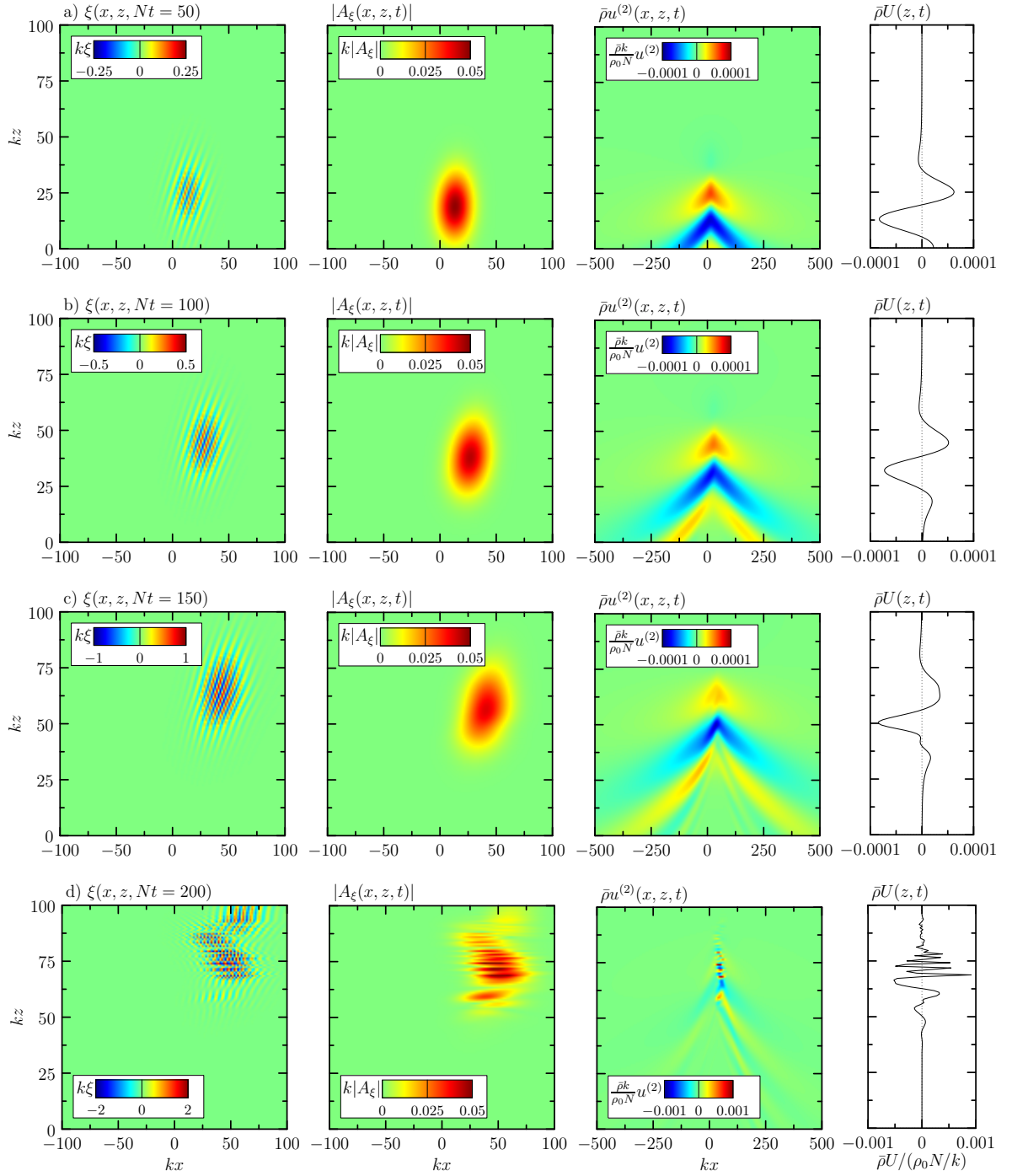


Figure 4.2: As in Fig. 4.1 but for a wavepacket with relative vertical wavenumber $m = -0.7k$. Note that the colour bar limits in the centre-right panels are double the limits of the colour bars in the corresponding panels in Fig. 4.1.

near the margin separating whether modulational instability will cause the leading or trailing flank of the wavepacket to grow in relative amplitude.

At $t = 100N^{-1}$ (Fig. 4.2b), the wavepacket has begun to ‘tilt’ due to oblique dispersion, and its peak amplitude has decreased by 12% of its initial value to $|A_\xi|_{\max} = 0.044k^{-1}$. A slight horizontal asymmetry is developing in the induced long wave, in which the magnitude is mildly enhanced on the left half of the induced flow relative to the right half. However, this feature appears to have no effect on the structure of the wave-induced momentum profile.

At $t = 150N^{-1}$ (Fig. 4.2c), the vertical displacement amplitude envelope exhibits both horizontal and vertical asymmetry due to oblique dispersion. The horizontal asymmetry in the wave-induced momentum field has continued to develop, enhancing the relative flow magnitudes on the left half. The magnitude of the positive induced momentum on the leading flank of the wavepacket at $k\tilde{z} \approx 70$ has ‘flattened’ somewhat, while the negative flow on the trailing flank has grown in magnitude.

At $t = 200N^{-1}$ (Fig. 4.2d), the wavepacket has degenerated to such a degree that it may no longer be justifiably considered quasi-monochromatic. Rather, the ‘wavepacket’ appears as a series of closely spaced peaks, with $|A_\xi|_{\max} = 0.057k^{-1}$. As such, crests and troughs in the vertical displacement field are only vaguely identifiable. The induced long wave has lost most of its horizontal structure, now appearing as a series of jets localized in the vicinity of the wavepacket. The magnitudes of the peaks in the induced mean momentum profiles have accordingly increased by an order of magnitude from earlier times (Figs. 4.2a,b,c). Diagnostics presented later will show that the wavepacket is overturning at this time.

The weakly nonlinear evolution of a Gaussian wavepacket initialized using (3.10) with $A_{\xi_0} = 0.05k^{-1}$, $m = -1.4k$, $\sigma_x = \sigma_z = 10k^{-1}$, and $H_\rho = 10k^{-1}$ is shown at four times in Fig. 4.3. The respective columns in Fig. 4.3 correspond to the columns in Fig. 4.1. Having a relative vertical wavenumber of $m = -1.4k$ means that these waves translate rightward at approximately the fastest horizontal group speed. For this reason the fields of view in the leftmost and centre-left columns of Fig. 4.3 have been shifted rightward. For one-dimensional wavepackets, this vertical wavenumber corresponds to modulationally stable waves. However, when the wavepacket is horizontally and vertically localized, the negative values of the wave-induced mean flow along the trailing flank of the wavepacket lead us to expect that this region

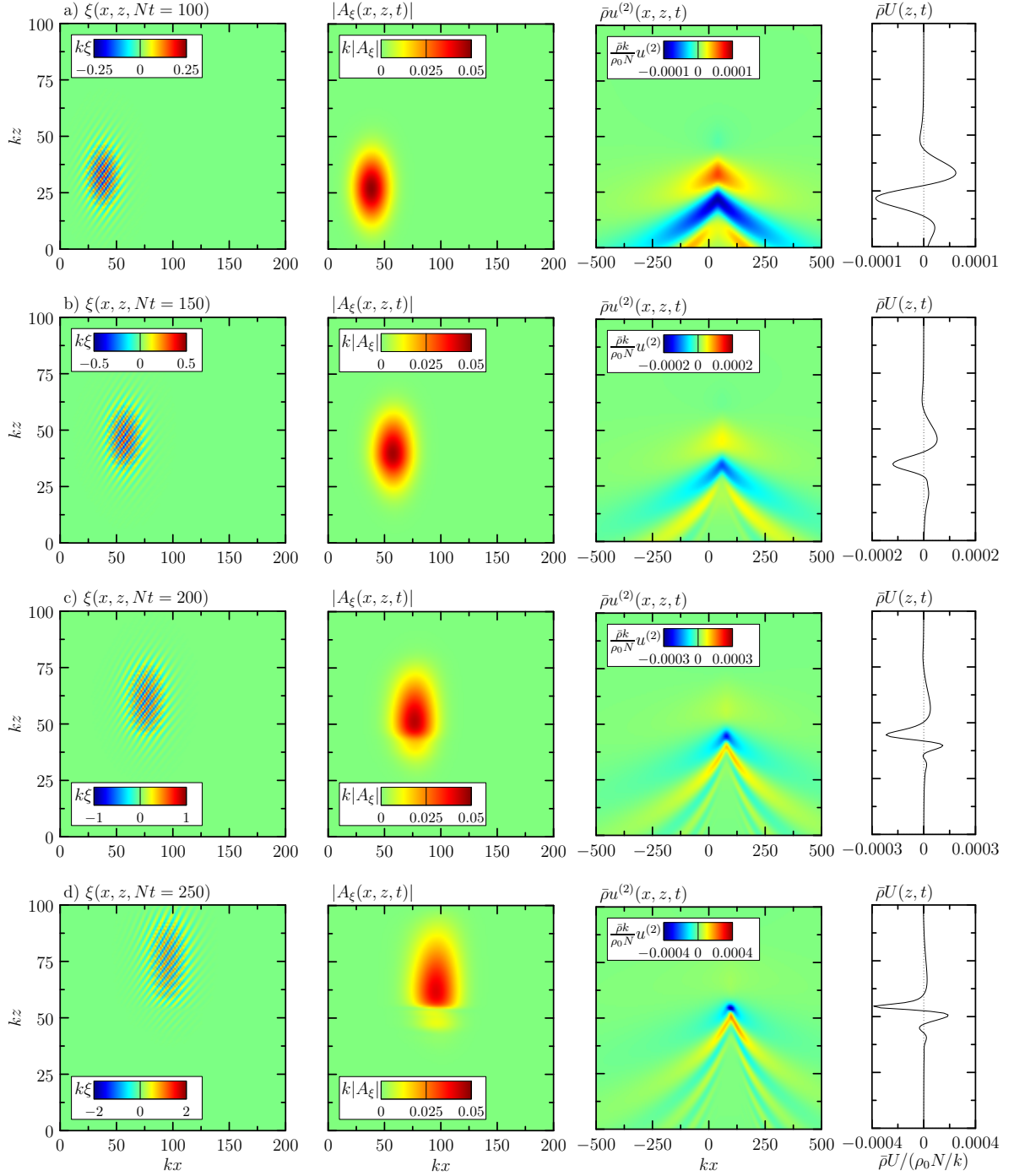


Figure 4.3: As in Fig. 4.1 but for a wavepacket with relative vertical wavenumber $m = -1.4k$. The evolution is shown at times t equal to (a) $100N^{-1}$, (b) $150N^{-1}$, (c) $200N^{-1}$, and (d) $250N^{-1}$. The fields of view in the leftmost and centre-left column have been shifted rightward because the wavepacket translates rightward at approximately the fastest horizontal group speed. Note that the horizontal axis limits in the rightmost panels and the colour bar limits in the centre-right panels each increase linearly in time through (a) – (d).

will exhibit vertical narrowing and relative amplitude growth while the leading flank of the wavepacket is expected to exhibit vertical broadening and relative amplitude decay. Being located in a region of weaker anelastic growth relative to the leading flank, the trailing flank of the wavepacket requires more time to propagate vertically in order to reach an amplitude sufficient for the development of weakly nonlinear effects. Hence we expect the life cycle of a wavepacket with $m = -1.4k$ to be relatively long compared to waves with relative vertical wavenumbers m equal to $-0.4k$ or $-0.7k$. As such, the times shown in Fig. 4.3 are later by $50N^{-1}$ than the corresponding panels shown in Figs. 4.1 and 4.2.

Fig. 4.3a shows the wavepacket evolution at $t = 100N^{-1}$. The wavepacket behaves according to linear theory, evident in part by the small relative discrepancy $\delta_c \approx -(0.08, 0.02)$ and maximum vertical displacement amplitude $|A_\xi|_{\max} = 0.048k^{-1}$. The wave-induced momentum field is horizontally symmetric and the magnitudes of the positive and negative flows on the leading and trailing flanks of the wavepacket, respectively, are of similar magnitude.

Weakly nonlinear effects have begun to manifest at $t = 150N^{-1}$ (Fig. 4.3b). This is most noticeable in the induced momentum field. Modulational instability is focused on the trailing flank of the wavepacket because the induced flow is initially negative there. As such, the trailing flank is prone to wave accumulation and hence relative amplitude growth, which is observed in the slightly increased magnitude of the negative flow in the rightmost panel of Fig. 4.3b. The induced flow on the leading flank of the wavepacket has decreased in magnitude and spread vertically, as expected.

The development of weak nonlinearity continues to affect the evolution of the wavepacket through $t = 200N^{-1}$ (Fig. 4.3c) until it has caused the wavepacket to become vertically asymmetric at $t = 250N^{-1}$ (Fig. 4.3d). The vertical displacement amplitude envelope has broadened significantly on the leading flank of the wavepacket, while the initial centre of the wavepacket has become effectively the trailing edge of the wavepacket. This is partly due to the vertical spreading of the trailing flank of the wavepacket due to the development of a positive peak in the wave-induced momentum on the trailing flank (of approximately half the magnitude of the negative peak) coupled with $\omega_{mm} > 0$. Perhaps counter-intuitively, the peak value of the amplitude envelope has steadily decreased by $\sim 20\%$ of its initial value during the simulation. While the trailing flank of the wavepacket is unstable to vertical modulations,

leading to relative amplitude growth, horizontal modulations are strongest for $m = -1.4k$ because this wavenumber corresponds to waves having approximately the fastest horizontal group speed. This is coupled with the relatively strong (negative) peak value of the induced momentum, so where this peak is located, horizontal modulations act to decrease the peak amplitude.

4.1.1 Effect of Oblique Dispersion Terms

Oblique dispersion terms are those whose coefficients involve mixed k - and m -derivatives of ω in the nonlinear Schrödinger equation (2.54). To determine the qualitative effects of oblique dispersion, three weakly nonlinear simulations were conducted in which the oblique dispersion terms were removed from the nonlinear Schrödinger equation. Each simulation was initialized using (3.10) with $A_{\xi_0} = 0.05k^{-1}$, $\sigma_x = \sigma_z = 10k^{-1}$, $H_\rho = 10k^{-1}$, and either $m = -0.4k$, $-0.7k$, or $-1.4k$. Results from the corresponding simulations with oblique dispersion are shown in the left column of Fig. 4.4, and the results without oblique dispersion are shown in the centre column. The right column shows profiles of the wave-induced momentum from both simulation types. Snapshots at $t = 150N^{-1}$ (Figs. 4.4a,b) and $t = 200N^{-1}$ (Fig. 4.4c) were chosen because the effects of oblique dispersion were deemed to have had sufficient time to develop to a degree that qualitative comparisons would be meaningful.

Fig. 4.4a compares the results of the simulations with and without oblique dispersion for a wavepacket with $m = -0.4k$. The moduli of the vertical displacement amplitude functions from the respective simulations are shown in the left and centre panels. Clockwise ‘tilting’ of the wavepacket with oblique dispersion is absent in the wavepacket without oblique dispersion. Comparing the maximum vertical displacement amplitudes in each case, we find that oblique dispersion accounts for $\sim 13\%$ of the observed amplitude decay. This is also seen qualitatively in the right panel, which compares the wave-induced momentum profiles through the centres of the wavepackets with oblique dispersion (solid curve) and without (dashed curve). The corresponding locations in the horizontal through which the profiles were taken are indicated by the solid and dashed lines in the left and centre panels. The local extrema in the induced momentum profiles are approximately co-located, although the magnitudes are diminished in the presence of oblique dispersion.

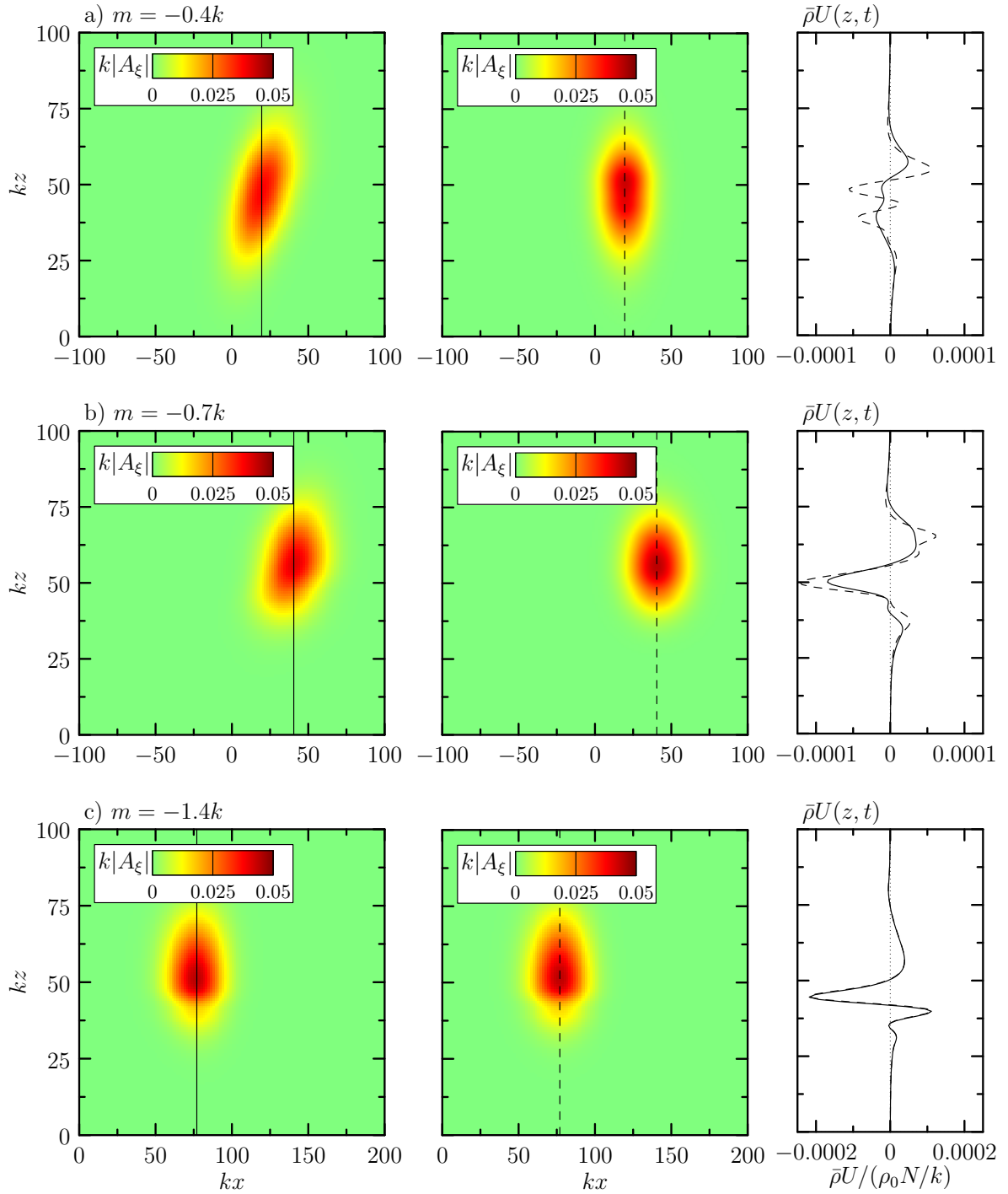


Figure 4.4: Comparison of the moduli of the vertical displacement amplitude envelopes of wavepackets resolved by weakly nonlinear simulations conducted with oblique dispersion terms (left column) and without (centre column). The snapshots shown in panels (a) and (b) were taken at $t = 150N^{-1}$ and the snapshots shown in panel (c) were taken at $t = 200N^{-1}$. The panels in the left column are identical to the leftmost panels shown in Figs. 4.1c, 4.2c, and 4.3c, respectively. In the right panels, the solid curves are vertical profiles of the wave-induced momentum through the horizontal centres of the translating wavepackets shown in the left panels. The dashed curves are the same, but through the horizontal centres of the translating wavepackets shown in the centre panels.

A comparison of the results of simulations with and without oblique dispersion for a wavepacket with $m = -0.7k$ is shown in Fig. 4.4b. The individual panels correspond to those in Fig. 4.4a. In the left panel of Fig. 4.4b, the clockwise ‘tilting’ effect of oblique dispersion is focused on the trailing flank of the wavepacket, whereas the leading flank appears largely unaffected by oblique dispersion. In the right panel, local extrema in the induced momentum profiles below $kz \approx 50$ are approximately co-located, whereas there is a peak at $kz \approx 65$ that was not resolved in the simulation with oblique dispersion.

For a wavepacket with $m = -1.4k$, oblique dispersion terms have negligible effect on the evolution over moderately long time scales, as shown in Fig. 4.4c. Qualitatively, the wavepacket in the simulation with oblique dispersion is indistinguishable from the wavepacket without oblique dispersion, as seen by comparing the left and centre panels. Comparing the maximum vertical displacement amplitudes we find that the amplitude of the wavepacket without oblique dispersion is 99.7% that of the wavepacket with oblique dispersion.

Oblique dispersion appears to be an effect unique to two-dimensional wavepackets. A search of the literature did not reveal any earlier discovery of this or qualitatively similar phenomena. A more detailed exploration of its effects on the evolution and overturning of two-dimensional internal gravity wavepackets was beyond the scope of this thesis.

4.1.2 Wave-Induced Mean Flow

Another method for representing wavepacket evolution is through time series of the density-scaled wave-induced mean flow through the horizontal centre of the translating wavepacket, $\tilde{x} = x - c_{g_x}t = 0$. Such profiles are more succinctly referred to as profiles of the centreline induced momentum. Fig. 4.5 shows time series of the centreline induced momentum profiles from the previously discussed weakly nonlinear simulations. The results in each panel are plotted in a frame of reference translating at the wavepacket’s vertical group speed, $\tilde{z} = z - c_{g_z}t$, and further normalized by the peak initial value of the wave-induced mean flow, $\rho_0 U_0 = \max_z \{\bar{\rho}U(z, 0)\}$, as determined from the numerical output from their respective simulations. The selections in each panel show the evolution only until $t = 250N^{-1}$, less than the duration of the simulations. In each case the wavepacket dynamics were well represented in the selections shown.

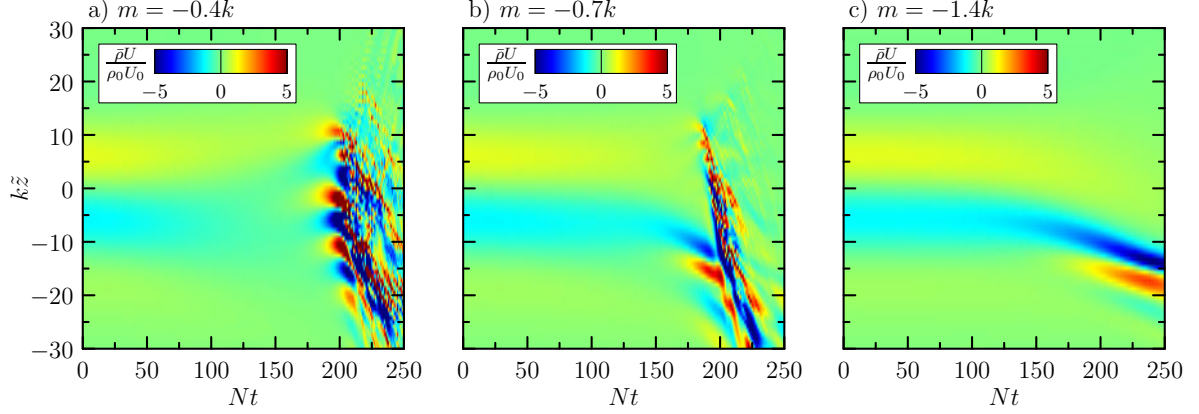


Figure 4.5: Time series of the density-scaled wave-induced mean flow, $\bar{\rho}U(z, t)$, through the horizontal centres of translating wavepackets with relative vertical wavenumbers m equal to (a) $-0.4k$, (b) $-0.7k$, and (c) $-1.4k$, as computed by weakly nonlinear simulations. Each simulation was initialized using (3.10) with $A_{\varepsilon_0} = 0.05k^{-1}$, $\sigma_x = \sigma_z = 10k^{-1}$, and $H_\rho = 10k^{-1}$. The results in each panel are normalized by the peak initial value of the wave-induced mean flow, $\rho_0 U_0$, determined from the output of their respective simulations at $t = 0$, and plotted in a frame of reference translating at the wavepacket’s vertical group speed, $\tilde{z} = z - c_{g_z} t$.

Fig. 4.5a shows the time series of the centreline induced momentum from the weakly nonlinear simulation with $m = -0.4k$ (corresponding to the snapshots shown in Fig. 4.1). The effects of linear dispersion are visible between $t = 100N^{-1}$ and $t = 150N^{-1}$, marked by decreasing magnitudes of both the positive and negative flows along the leading and trailing flanks of the wavepacket, respectively. Shortly thereafter, weakly nonlinear effects cause the induced flow to degenerate into a series of positive and negative jets. A similar phenomenon was observed in the flow induced by the one-dimensional wavepackets studied by DS11. However, in their results the jets developed in time toward the trailing edge of the wavepacket and their flow was unidirectional. Doppler-shifting of the wave frequency by the induced mean flow is responsible for the weakly nonlinear evolution. On the leading flank, where $U > 0$ and $\omega_{mm} < 0$, the wave-induced flow suddenly peaks, forming the positive jet located at $k\tilde{z} \approx 10$. On the trailing flank, where $U < 0$ initially, Doppler-shifting causes an increase in the vertical group speed, which causes the trailing edge of the wavepacket to advance toward the leading edge. After $t \approx 200N^{-1}$, the jets themselves degenerate into small, disorganized structures. Diagnostics shown later will reveal that these structures are present in the solution of the nonlinear Schrödinger equation after wave overturning has commenced. As such, we accord these structures little dynamical significance.

The time series of the centreline induced momentum from the weakly nonlinear simulation

with $m = -1.4k$ (corresponding to the snapshots shown in Fig. 4.3) is shown in Fig. 4.5c. On the leading flank of the wavepacket, where $U > 0$ and $\omega_{mm} > 0$, Doppler-shifting has increased the vertical group speed and the wavepacket has spread accordingly. From $t \approx 150N^{-1}$ onward, the induced momentum is sufficient in magnitude that Doppler-shifting significantly retards the vertical advance of the wavepacket, and the resulting accumulation of waves causes a sustained intensification of the magnitude of the negative induced momentum. At $t \approx 180N^{-1}$ a positive jet develops below the negative jet. This is due to wave spreading from the existing positive flow, hence wave accumulation behind the more slowly translating negative jet. A positive jet does not develop from the existing positive flow on the leading flank because this upward-translating flow experiences increased vertical group speed, thus spreads away from the negative jet, rather than toward it.

Two-dimensional internal gravity wavepackets with relative vertical wavenumber $m = -0.7k$ have frequency $\omega \gtrsim \omega_*$ (hence $\omega_{mm} \lesssim 0$), in which the critical transition frequency ω_* separates frequencies corresponding to narrowing and relative amplitude growth on the leading versus trailing flank of the wavepacket. As such, for wavepackets with $m = -0.7k$ the dynamics of the wave-induced momentum are expected to resemble a combination of the dynamics of the cases using $m = -0.4k$ and $m = -1.4k$. Indeed, this is seen in Fig. 4.5b (which corresponds to the snapshots shown in Fig. 4.2). Until $t \approx 150N^{-1}$ there is minor spreading over the vertical extent of the wavepacket due to linear dispersion. After this time a negative jet develops from the negative flow on the trailing flank of the wavepacket, followed by the development of a positive jet below it at $t \approx 175N^{-1}$. These dynamics are similar to those observed on the trailing flank in the case with $m = -1.4k$. Approximately concurrent with the development of these features is the sudden emergence of short-lived positive and negative jets between $k\tilde{z} = 10$ and $k\tilde{z} = 15$, which rapidly develop in time toward the centre of the wavepacket until $t \approx 200N^{-1}$. These dynamics are similar to those observed on the leading flank in the case with $m = -0.4k$.

The wave-induced momentum profiles just discussed are examined more quantitatively by considering the time series of their L^2 -norms. Fig. 4.6 shows the relative wave-induced momentum, $\|\widetilde{M}(t)\|$, given by (3.13), of the results in Fig. 4.5. Included for reference is the dotted line corresponding to $\|\widetilde{M}(t)\| = 1$, below which linear dispersion dominates the

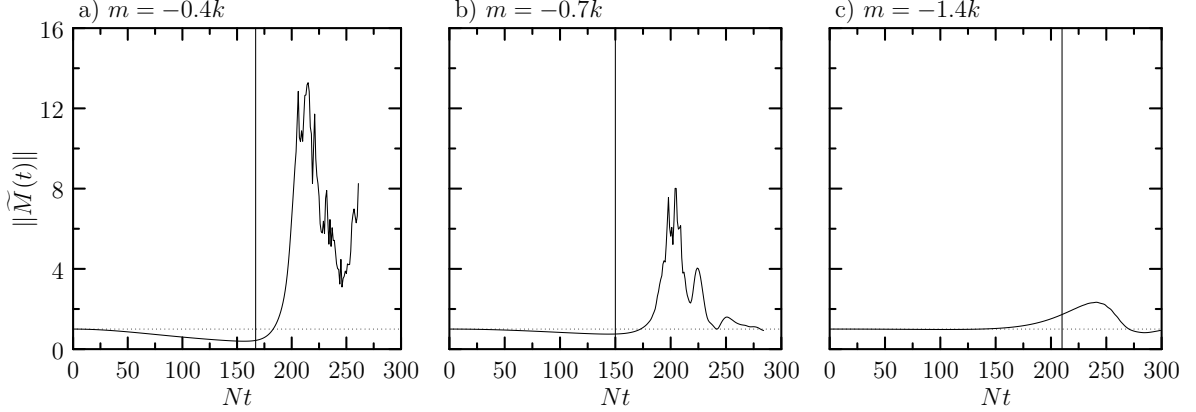


Figure 4.6: Time series of the relative L^2 -norms of the centreline wave-induced momentum profiles, given by (3.13), for weakly nonlinear simulations with relative vertical wavenumbers m equal to (a) $-0.4k$, (b) $-0.7k$, and (c) $-1.4k$. Each panel (a) – (c) corresponds to the time series of density-scaled wave-induced mean flow profiles shown in panels (a) – (c) in Fig. 4.5. The vertical bars correspond to the times, t_Δ , given by (3.17), at which weakly nonlinear effects are predicted to become significant.

wavepacket dynamics, and above which nonlinear effects dominate the wavepacket dynamics.

The relative wave-induced momentum for the simulation with $m = -0.4k$ is shown as the solid black curve in Fig. 4.6a. Until $t \approx 170N^{-1}$, the induced momentum magnitude steadily decreases due to dispersion. Afterward, the magnitude rapidly increases, indicating that weakly nonlinear effects have become significant. This sudden increase is associated with the degeneration of the induced flow into the positive and negative jets seen in Fig. 4.5a. The vertical bar located at $t_\Delta = 167N^{-1}$, with t_Δ given by (3.17), denotes the time at which weakly nonlinear effects are predicted to become significant. That it is located near the minimum value of $\|\widetilde{M}(t)\|$ indicates good agreement between the predicted and actual times at which weakly nonlinear effects became significant.

The time series $\|\widetilde{M}(t)\|$ for the simulation with $m = -1.4k$ is shown in Fig. 4.6c. The induced momentum magnitude does not noticeably decrease below unity as this wavepacket is less dispersive than wavepackets for which $m = -0.4k$. Weakly nonlinear effects become significant at $t \approx 150N^{-1}$, indicated by the increasing magnitude of the induced momentum. However, the vertical bar located at $t_\Delta = 210N^{-1}$ indicates that the time at which weakly nonlinear effects were predicted to become significant was over-estimated by $\sim 40\%$.

The time series $\|\widetilde{M}(t)\|$ for the simulation with $m = -0.7k$ is shown in Fig. 4.6b. The observed evolution of the induced momentum magnitude is a combination of the evolution in Figs. 4.6a,c. In particular, the magnitude decreases slightly below unity, but not by the

amount seen in the case with $m = -0.4k$. This is followed by a sudden increase at $t \approx 170N^{-1}$ to a maximum magnitude of $\|\widetilde{M}(198)\| = 7.56$, which is $\sim 60\%$ of the magnitude of the first peak in the case with $m = -0.4k$, and $\sim 220\%$ greater than the peak magnitude in the case with $m = -1.4k$. The time at which weakly nonlinear effects are predicted to become significant, $t_\Delta = 150N^{-1}$, is somewhat under-estimated.

4.1.3 Effect of Changing σ_x and H_ρ

Here, we discuss the effects of quadrupled horizontal wavepacket extent (i.e. setting $\sigma_x = 40k^{-1}$) and of halved density scale height (i.e. setting $H_\rho = 5k^{-1}$) on the weakly nonlinear wavepacket dynamics. Rather than discussing in detail snapshots of wavepacket evolution, we will discuss time series of centreline wave-induced mean flow and of relative induced momentum, with an emphasis on representative cases of wave evolution using $\sigma_x = 40k^{-1}$ and $H_\rho = 5k^{-1}$, and their comparison with the cases already discussed.

Time series of the density-scaled wave-induced mean flow through the centres of relatively long wavepackets (for which $\sigma_x = 40k^{-1}$) as they propagate through an atmosphere with density scale height $H_\rho = 10k^{-1}$ are shown in Fig. 4.7. Panels (a) – (c) correspond to wavepackets with relative vertical wavenumbers m equal to $-0.4k$, $-0.7k$, and $-1.4k$, respectively. The results in Fig. 4.7 are compared with the corresponding panels in Fig. 4.5, for which $\sigma_x = 10k^{-1}$.

In each panel in Fig. 4.7, weakly nonlinear effects become significant at earlier times than for wavepackets for which $\sigma_x = 10k^{-1}$. This is because, compared to the initial mean flow induced by a wavepacket with $\sigma_x = 10k^{-1}$, the flow induced by a long wavepacket is approximately four times greater in magnitude, as predicted by (A.16). Hence, the long wavepackets achieve an amplitude sufficient for the onset of weakly nonlinear effects at a lower altitude than for their counterparts with $\sigma_x = 10k^{-1}$.

Fig. 4.7a shows the results for a relatively long wavepacket with relative vertical wavenumber $m = -0.4k$. Like its counterpart with $\sigma_x = 10k^{-1}$ (Fig. 4.5a), the mean flow degenerates into a series of positive and negative jets. However, fewer jets were resolved by the simulation of the long wavepacket, and jets were typically of smaller peak magnitude than their counterparts using $\sigma_x = 10k^{-1}$.

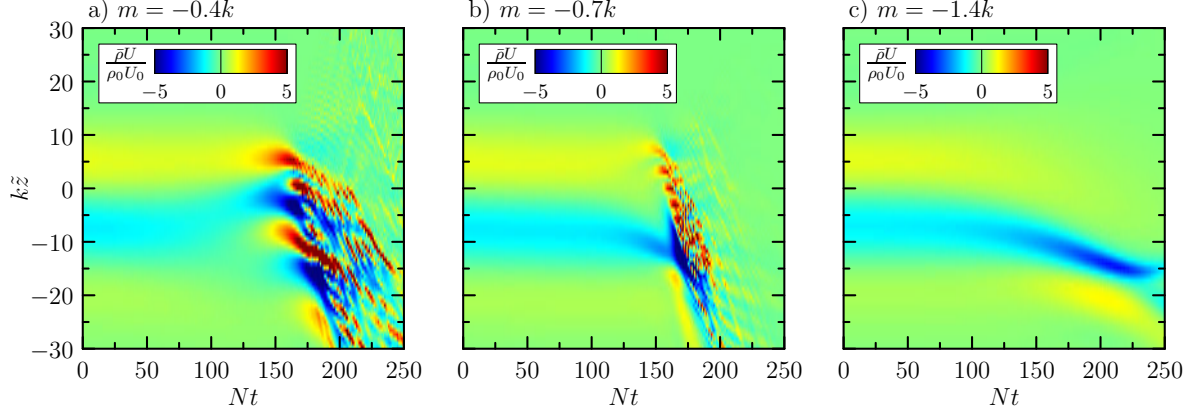


Figure 4.7: Time series of the density-scaled wave-induced mean flow, $\bar{\rho}U(z, t)$, through the horizontal centres of translating wavepackets with relative vertical wavenumbers m equal to (a) $-0.4k$, (b) $-0.7k$, and (c) $-1.4k$, as computed by weakly nonlinear simulations. Each simulation was initialized using (3.10) with $A_{\varepsilon_0} = 0.05k^{-1}$, $\sigma_x = 40k^{-1}$, $\sigma_z = 10k^{-1}$, and $H_\rho = 10k^{-1}$. The results in each panel are normalized by the peak initial value of the wave-induced mean flow, $\rho_0 U_0$, determined from the output of their respective simulations at $t = 0$, and plotted in a frame of reference translating at the wavepacket's vertical group speed, $\tilde{z} = z - c_{gz} t$.

The results of the simulation of the long wavepacket with $m = -1.4k$ is shown in Fig. 4.7c. Like its counterpart using $\sigma_x = 10k^{-1}$ (Fig. 4.5c), the positive flow along the leading flank of the wavepacket decays in magnitude. A negative jet develops at $t \approx 150N^{-1}$ with a region of positive flow below it developing at $t \approx 175N^{-1}$. The negative flow reaches a peak magnitude between $t \approx 175N^{-1}$ and $t \approx 225N^{-1}$. Unlike the wavepacket with $\sigma_x = 10k^{-1}$, the jet then narrows slightly while decaying in magnitude, which is associated with an observed increase in the rate of its vertical translation.

The flow induced by a long wavepacket with $m = -0.7k$ is shown in Fig. 4.7b. Like its counterpart with $\sigma_x = 10k^{-1}$ (Fig. 4.5b), the dynamics resemble a combination of those in the cases with $m = -0.4k$ and $m = -1.4k$ (Figs. 4.7a,c, respectively). The most obvious qualitative similarity between the time series of the flows induced by the wavepackets with $\sigma_x = 10k^{-1}$ and $\sigma_x = 40k^{-1}$ is the development of negative jets from the negative flow on the trailing flank of the wavepackets at $t \approx 150N^{-1}$ and at $t \approx 125N^{-1}$, respectively. However, for the long wavepacket the jet rapidly spreads vertically and grows in magnitude at $t \approx 160N^{-1}$. The short-lived leading edge jets observed in Fig. 4.5b are similarly resolved by the simulation of the long wavepacket, although the jets are positive, as opposed to positive and negative, as was the case for the wavepackets with $\sigma_x = 10k^{-1}$.

A plot comparing the time series of relative induced momentum profiles, $\|\widetilde{M}(t)\|$, of wave-

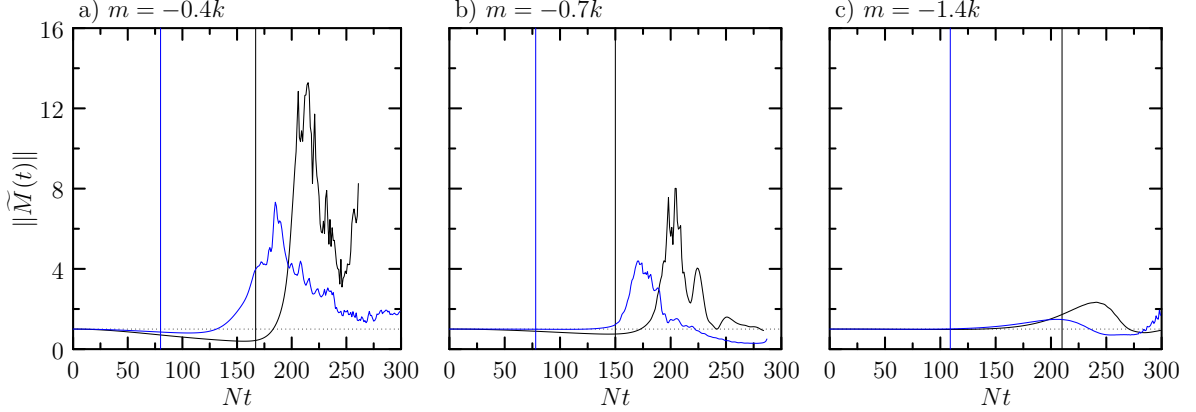


Figure 4.8: Time series of the relative L^2 -norms of the centreline wave-induced momentum profiles, given by (3.13), for weakly nonlinear simulations with relative vertical wavenumbers m equal to (a) $-0.4k$, (b) $-0.7k$, and (c) $-1.4k$, using either $\sigma_x = 10k^{-1}$ (black curves) or $\sigma_x = 40k^{-1}$ (blue curves). The black curves and the black vertical bars are identical to those shown in the corresponding panels in Fig. 4.6. The blue curves in each panel (a) – (c) correspond to the time series of density-scaled wave-induced mean flow profiles shown in panels (a) – (c) in Fig. 4.7. The blue vertical bars correspond to the times, t_Δ , given by (3.17), at which weakly nonlinear effects are predicted to become significant in the simulations using $\sigma_x = 40k^{-1}$.

packets using $\sigma_x = 10k^{-1}$ and $\sigma_x = 40k^{-1}$ is shown in Fig. 4.8. The black curves correspond to wavepackets with $\sigma_x = 10k^{-1}$ and are identical to those shown in Fig. 4.6. The blue curves correspond to long wavepackets, and represent the L^2 -norms of the density-scaled induced flow time series shown in Fig. 4.7. Panels (a) – (c) of Fig. 4.8 correspond to wavepackets with relative vertical wavenumbers m equal to $-0.4k$, $-0.7k$, and $-1.4k$, respectively.

During the early times in the evolution of the long wavepackets, the induced momentum magnitudes do not decay below unity to a degree comparable with their counterparts using $\sigma_x = 10k^{-1}$. In particular, the long wavepackets with $m = -0.7k$ and $m = -1.4k$ do not decay noticeably. This suggests that long wavepackets are less dispersive than their counterparts with $\sigma_x = 10k^{-1}$. The earlier onset of weakly nonlinear effects for long wavepackets is reflected in the departures of the blue curves from the reference value of $\|\widetilde{M}(t)\| = 1$, as seen in Figs. 4.8a,b,c. This observation is in agreement with the fact that longer wavepackets more closely resemble one-dimensional wavepackets, for which the onset of weakly nonlinear effects is earlier than for two-dimensional wavepackets (see DS11). For each relative vertical wavenumber examined, the peak value of the induced momentum for long wavepackets is approximately half the peak value for their counterparts using $\sigma_x = 10k^{-1}$. Finally, the predicted times, t_Δ , given by (3.17), at which weakly nonlinear effects are predicted to become significant, are substantially under-estimated for long wavepackets, as seen in the blue vertical

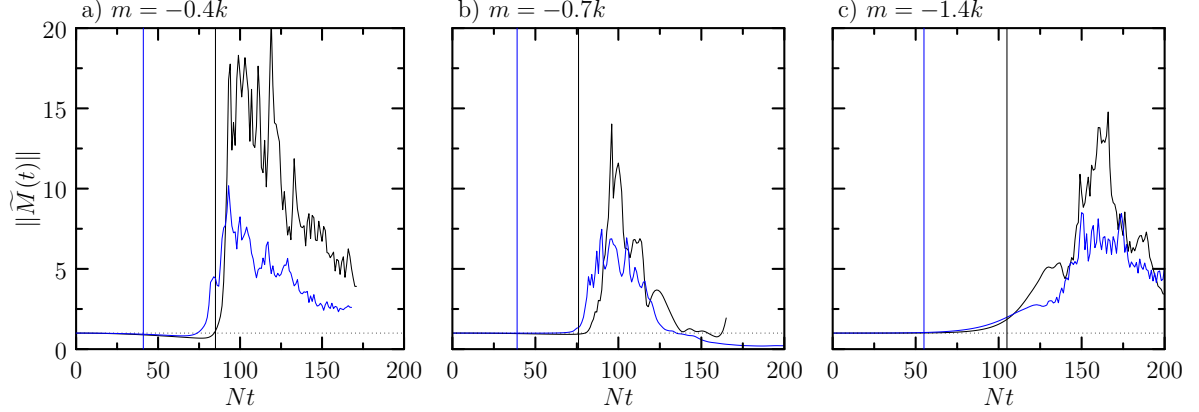


Figure 4.9: Time series of the relative L^2 -norms of the centreline wave-induced momentum profiles, given by (3.13), for weakly nonlinear simulations with a density scale height of $H_\rho = 5k^{-1}$. The relative vertical wavenumbers m are equal to (a) $-0.4k$, (b) $-0.7k$, and (c) $-1.4k$, and the simulations use either $\sigma_x = 10k^{-1}$ (black curves) or $\sigma_x = 40k^{-1}$ (blue curves). The black and blue vertical bars correspond to the times, t_Δ , given by (3.17), at which weakly nonlinear effects are predicted to become significant in the simulations using $\sigma_x = 10k^{-1}$ and $\sigma_x = 40k^{-1}$, respectively.

bars, which are significantly dislocated from the times at which the blue curves begin to grow in magnitude (although less so in the case with $m = -1.4k$).

Finally we compare the effects of quadrupled horizontal wavepacket extent in an atmosphere with density scale height $H_\rho = 5k^{-1}$. Fig. 4.9 shows time series of the relative wave-induced momentum for simulations of wavepackets with $\sigma_x = 10k^{-1}$ (black curves) and $\sigma_x = 40k^{-1}$ (blue curves), in an atmosphere with density scale height $H_\rho = 5k^{-1}$. Panels (a) – (c) of Fig. 4.9 correspond to simulations with relative vertical wavenumbers m equal to $-0.4k$, $-0.7k$, and $-1.4k$, respectively.

For all relative vertical wavenumbers and horizontal wavepacket extents examined, the onset of weakly nonlinear effects is earlier for wavepackets propagating through an atmosphere with density scale height $H_\rho = 5k^{-1}$ than with $H_\rho = 10k^{-1}$. This is because in the atmosphere with $H_\rho = 5k^{-1}$, anelastic growth is more pronounced at any given height. Thus, it is expected that any two-dimensional wavepacket will grow to an amplitude sufficient for the onset of weakly nonlinear effects at a lower altitude than its counterpart in an atmosphere with $H_\rho = 10k^{-1}$. The delay between the onset of weakly nonlinear effects for wavepackets using $\sigma_x = 10k^{-1}$ and $\sigma_x = 40k^{-1}$ is less than the delay in the atmosphere with $H_\rho = 5k^{-1}$. When $H_\rho = 10k^{-1}$ (Fig. 4.8), the peak magnitude of the induced momentum was observed to decrease as the absolute value of the relative vertical wavenumber increases. This tendency

is not observed in the simulations with $H_\rho = 5k^{-1}$ (Fig. 4.9). Rather, the peak magnitudes remain relatively large and the peak magnitudes for long wavepackets are approximately half that of their counterparts using $\sigma_x = 10k^{-1}$, for all relative vertical wavenumbers examined. The times, t_Δ , at which weakly nonlinear effects are predicted to become significant for wavepackets using $\sigma_x = 10k^{-1}$ are in better qualitative agreement for the cases with $H_\rho = 5k^{-1}$ than for those with $H_\rho = 10k^{-1}$. Conversely, the times at which weakly nonlinear effects are predicted to become significant remain substantially under-estimated for long wavepackets, as was the case in the results with $H_\rho = 10k^{-1}$.

4.2 Fully Nonlinear Simulations

Here, we compare the results of the previous section with those of fully nonlinear numerical simulations. In this way we assess the validity of weakly nonlinear theory. In all simulations reported on below, the bivariate Gaussian wavepackets were initialized using (3.10) with $A_{\xi_0} = 0.05k^{-1}$ and $\sigma_z = 10k^{-1}$.

Snapshots from the weakly and fully nonlinear simulations were found to be generally in very good qualitative agreement. As a representative example, Fig. 4.10 compares the vertical displacement fields from weakly (left column) and fully nonlinear (right column) simulations of a wavepacket with horizontal extent $\sigma_x = 10k^{-1}$ and relative vertical wavenumber $m = -0.4k$ at three different times as it propagates upward through an atmosphere with density scale height $H_\rho = 10k^{-1}$. Fig. 4.10b compares the vertical displacement fields at $t = 100N^{-1}$. At this time, the maximum values of the vertical displacement fields for the weakly and fully nonlinear simulations, respectively, are $\xi = 0.249k^{-1}$ and $\xi = 0.255k^{-1}$. The small difference between these maxima confirms that the diffusive terms introduced on the right-hand sides of fully nonlinear equations of motion (3.2) and (3.3) indeed have negligible effect on the wave dynamics.

Fig. 4.10c demonstrates that the qualitative agreement among the vertical displacement fields for the weakly and fully nonlinear simulations extends until at least $t = 187N^{-1}$, the first time wave overturning was recorded by the fully nonlinear simulation. At this time, the maximum vertical displacement for the weakly nonlinear simulation was $\xi = 1.046k^{-1}$, located

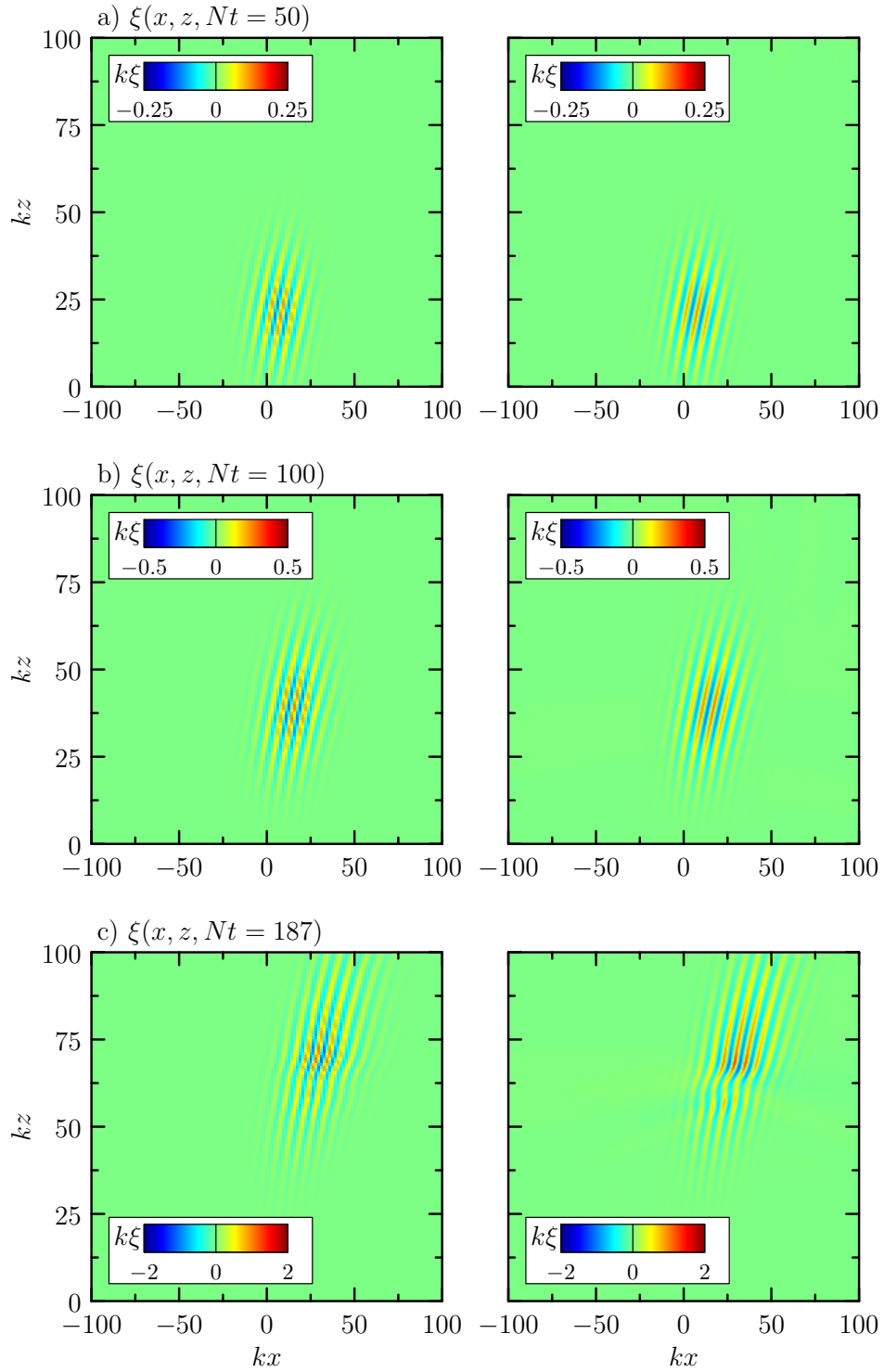


Figure 4.10: Comparison of the vertical displacement fields from weakly (left column) and fully nonlinear (right column) simulations of a wavepacket initialized using (3.10) with relative vertical wavenumber $m = -0.4k$ and horizontal extent $\sigma_x = 10k^{-1}$ as it propagates upward through an atmosphere with density scale height $H_\rho = 10k^{-1}$. The evolution is shown at times t equal to (a) $50N^{-1}$, (b) $100N^{-1}$, and (c) $187N^{-1}$. The left panels in (a) and (b) are identical to the leftmost panels in Figs. 4.1a,b, respectively.

at $z = 69.5k^{-1}$. The corresponding value for the fully nonlinear simulation is $\xi = 1.272k^{-1}$, located at $z = 68k^{-1}$. While the locations of these maxima agree within 3% of the fully nonlinear value, the actual maxima agree only within $\sim 18\%$ of the fully nonlinear value. Alternatively, if the wavepacket had evolved strictly according to linear theory, it would have translated vertically to $z \approx 60k^{-1}$ and its predicted maximum vertical displacement would be $\xi = A_0 e^{60/(2H_\rho k)} \approx 1.00k^{-1}$, owing to anelastic growth alone.

4.2.1 Wave-Induced Mean Flow

For comparison with the time series of centreline wave-induced mean flow profiles from the weakly nonlinear simulations, time series of centreline wave-induced mean flow profiles from fully nonlinear simulations using $\sigma_x = 10k^{-1}$ and $H_\rho = 10k^{-1}$ are shown in the right column of Fig. 4.11. The corresponding time series from the weakly nonlinear simulations shown in Figs. 4.5a,b,c are reproduced in the left panels of Figs. 4.11a,b,c, respectively. In the right panel of Fig. 4.11b, the simulation terminated at $t = 191N^{-1}$, hence the blank area is left in the figure intentionally.

Fig. 4.11a compares the time series of wave-induced mean flow profiles from weakly (left column) and fully nonlinear (right column) simulations with $m = -0.4k$. Qualitatively the results are nearly identical until just beyond $t = 150N^{-1}$, in part because the wavepacket evolves according to linear theory during this time. In the results of both simulations the induced flow degenerates into a series of positive and negative jets. Although fewer such features exist in the fully nonlinear results, stronger velocities developed at earlier times. It is remarkable that both simulations captured the splitting of the uppermost negative jet at $k\tilde{z} \approx 5$ just before $t = 200N^{-1}$, although quantitatively the jet in the fully nonlinear results is of larger magnitude.

The time series of induced flow from weakly and fully nonlinear simulations with $m = -1.4k$ are compared in Fig. 4.11c. Qualitatively, the results are nearly indistinguishable, save for the slightly larger magnitude in the negative induced flow from the nonlinear simulation until $t \approx 125N^{-1}$, during which the wavepacket evolves according to linear theory. The timing and location of the negative and positive jets which develop in succession from the negative part of the negative flow are likewise nearly identical. Diagnostics presented later will reveal that

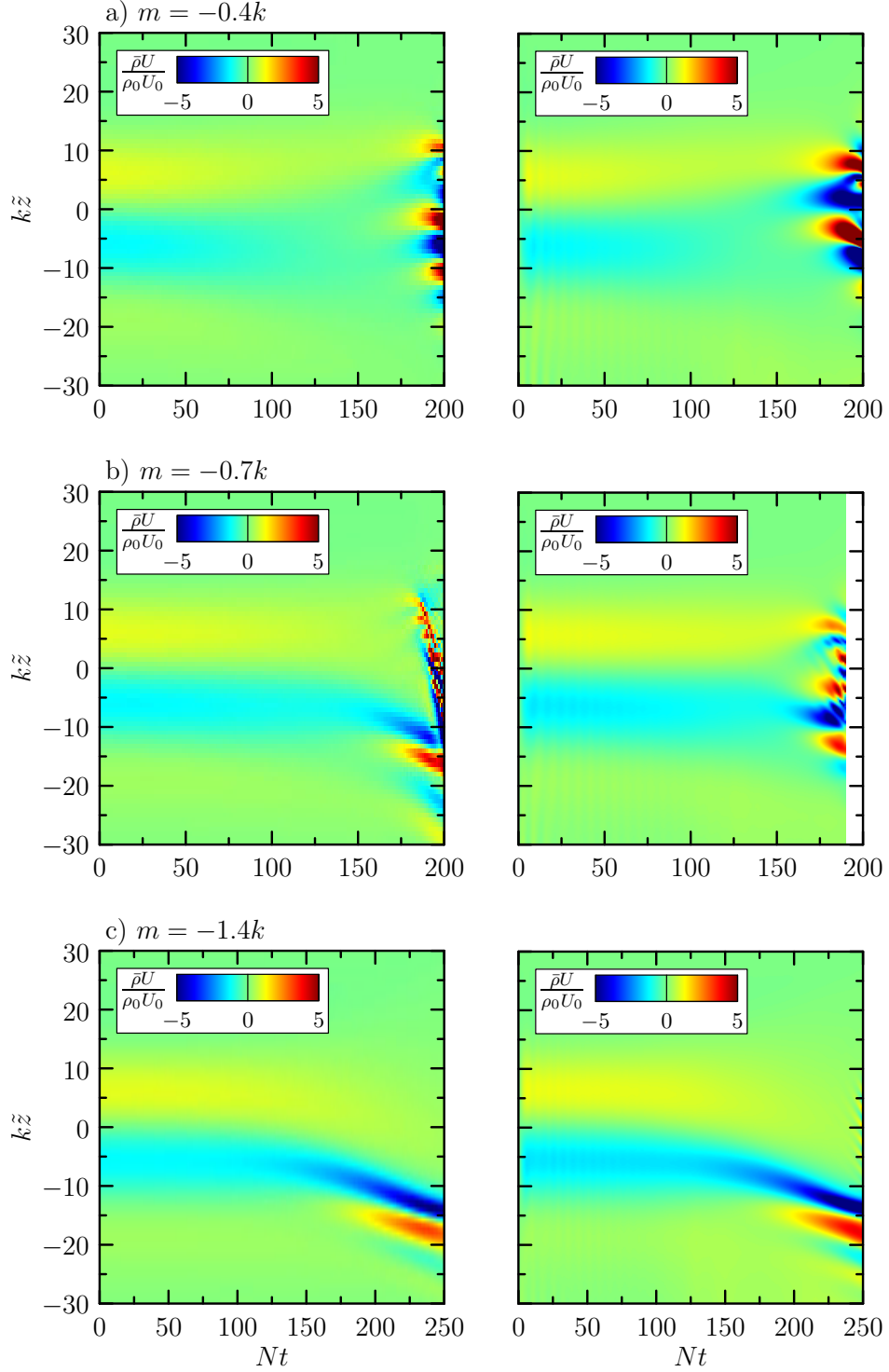


Figure 4.11: Comparison of the time series of vertical profiles of the density-scaled wave-induced mean flow, $\bar{\rho}U(z, t)$, through the horizontal centres of translating wavepackets from weakly (left column) and fully nonlinear (right column) simulations with relative vertical wavenumbers m equal to (a), $-0.4k$, (b), $-0.7k$, and (c) $-1.4k$. All simulations were initialized using (3.10) with $A_{\epsilon_0} = 0.05k^{-1}$, $\sigma_x = \sigma_z = 10k^{-1}$, and $H_\rho = 10k^{-1}$. The results are plotted in a frame of reference translating at the wavepacket's vertical group speed, $\tilde{z} = z - c_{gz}t$. The results in the left column are identical to those shown in Figs. 4.5a,b,c, respectively. In the right column, the results are normalized by the peak value of the induced flow profile predicted by setting $\tilde{x} = 0$ in (A.16).

qualitative agreement among these two simulations persisted for over eight buoyancy periods after wave overturning was first recorded by the fully nonlinear simulation. One qualitative difference between the two simulations is the development of a series of small-magnitude positive and negative jets from the remnants of the positive induced flow at $t \approx 190N^{-1}$ in the fully nonlinear simulation that were not resolved by the weakly nonlinear simulation.

A comparison of the time series of induced flow from the weakly and fully nonlinear simulations with $m = -0.7k$ is shown in Fig. 4.11b. A prominent negative jet develops out of the negative flow on the trailing flank of the wavepacket in both simulations at $t \approx 160N^{-1}$, followed shortly thereafter by the development of a positive jet below it. However, in the weakly nonlinear simulation these retard the vertical advance of the wavepacket, whereas in the results of the fully nonlinear simulation no such consequence is observed. A series of positive and negative jets develop at $t \approx 180N^{-1}$ from the positive wave-induced flow in both simulations, although these are more disorganized and of smaller scale in the weakly nonlinear simulation compared with the fully nonlinear simulation.

Fig. 4.12 compares the time series of the mean flows induced by relatively long wavepackets, for which $\sigma_x = 40k^{-1}$, from weakly (left column) and fully nonlinear (right column) simulations. For wavepackets with $m = -0.4k$ (Fig. 4.12a), the induced flows exhibit qualitative differences after $t \approx 150N^{-1}$. In particular, the positive jet centred at $k\tilde{z} \approx 5$ develops more suddenly in the weakly nonlinear simulation, and the negative jet centred at $k\tilde{z} \approx -15$ is unresolved by the fully nonlinear simulation. The fully nonlinear simulation develops larger magnitudes overall, noticeably, in the negative flow on the trailing edge of the wavepacket until $t \approx 100N^{-1}$. For wavepackets with $m = -1.4k$ (Fig. 4.12c), the qualitative features of the induced flow are well captured by both the weakly and fully nonlinear simulations. In particular, the negative jet decreases in magnitude at $t \approx 225N^{-1}$, and there is an associated increase in the wavepacket's vertical group speed. The fully nonlinear simulation tends to resolve larger magnitudes overall, in particular in the positive jet situated below the negative jet from $t \approx 200N^{-1}$ onward. Finally, for wavepackets with $m = -0.7k$ (Fig. 4.12b), the negative jet which developed from the negative induced flow acts to retard the vertical advance of the wavepacket in both the weakly and fully nonlinear simulations. Both simulations capture the development of positive and negative jets from the positive part of the induced flow on

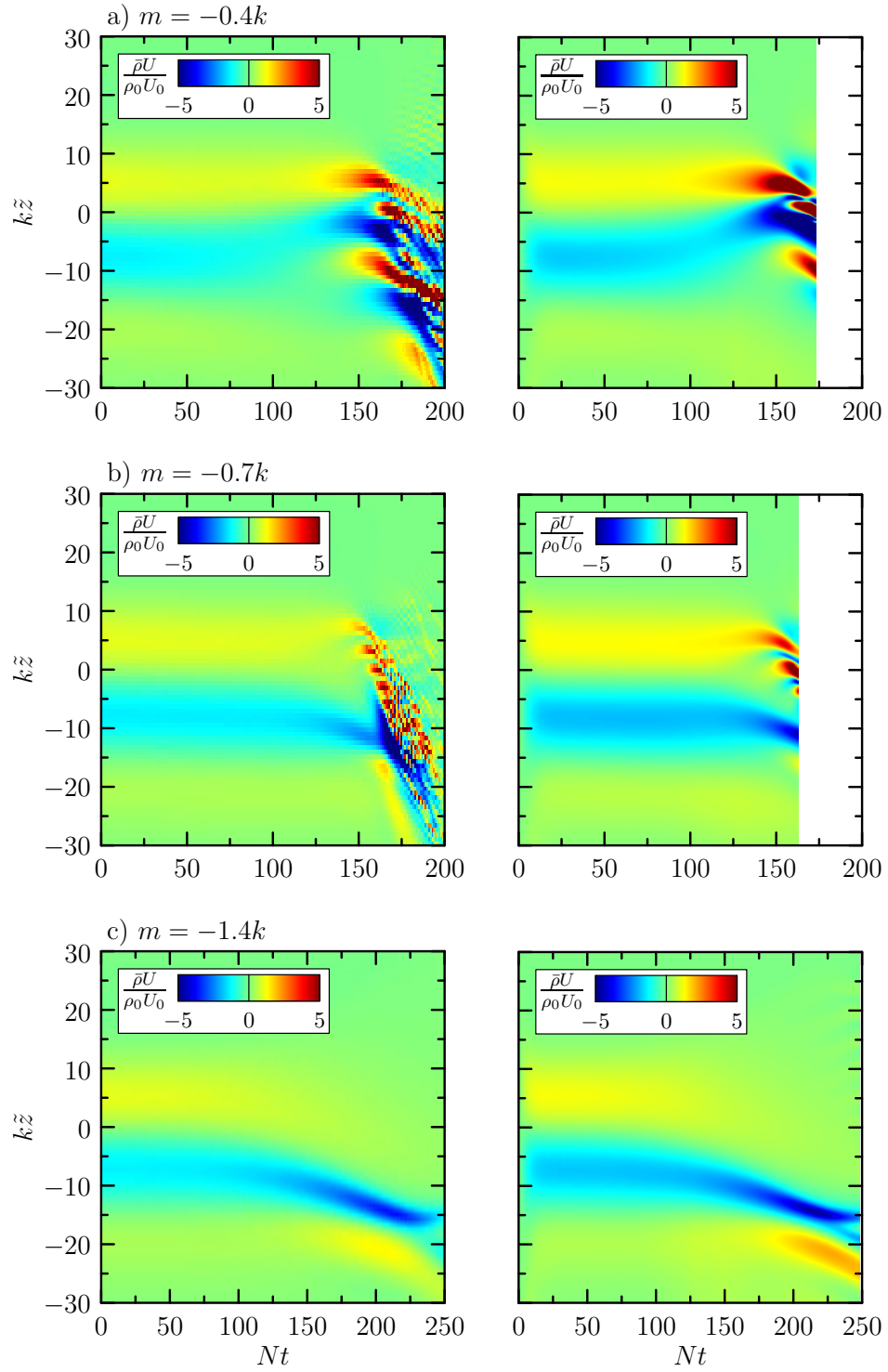


Figure 4.12: As in Fig. 4.11 but for relatively long wavepackets, for which $\sigma_x = 40k^{-1}$. The results in the left column are identical to those shown in Figs. 4.7a,b,c, respectively.

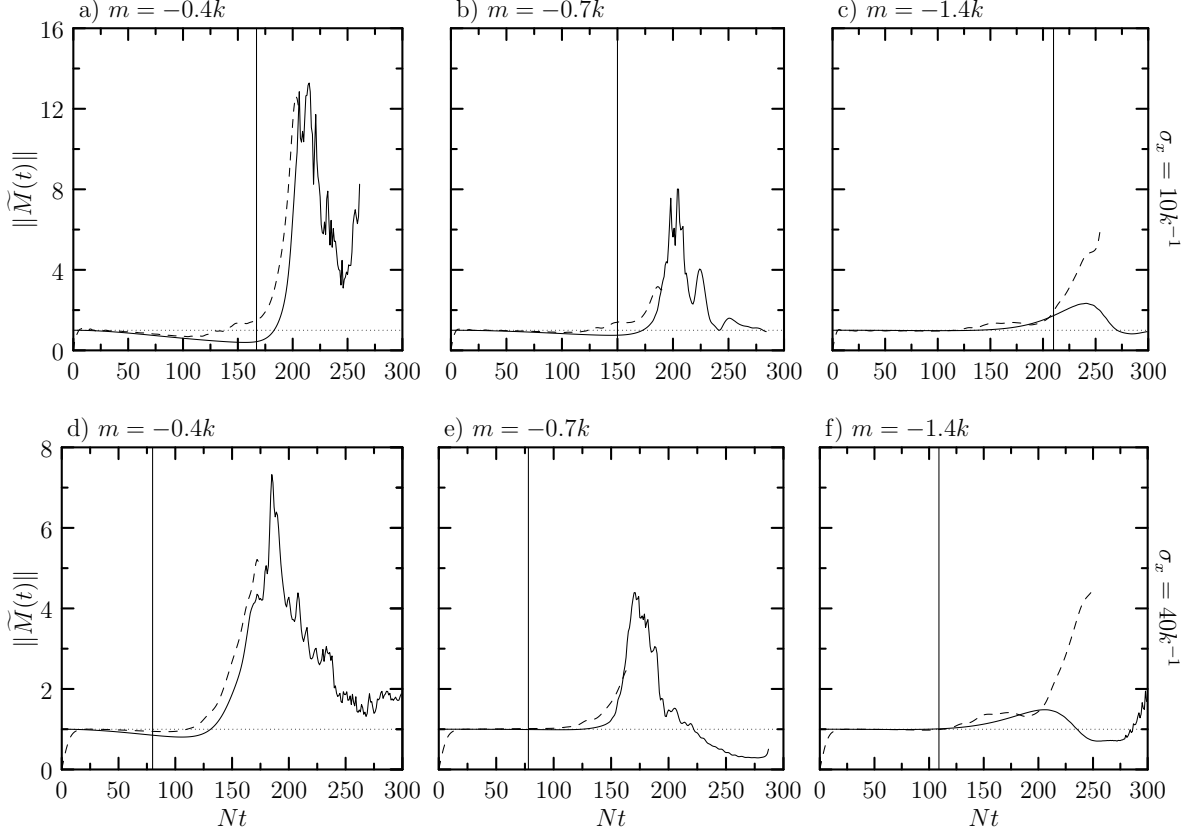


Figure 4.13: Time series of the L^2 -norms of relative wave-induced momentum profiles, given by (3.13), for weakly nonlinear (solid curves) and fully nonlinear (dashed curves) simulations with relative wavenumbers m equal to (a),(d) $-0.4k$, (b),(e) $-0.7k$, (c),(f) $-1.4k$. All simulations were conducted for an atmosphere with density scale height $H_\rho = 10k^{-1}$. Panels (a) – (c) correspond to simulations of wavepackets with horizontal extent $\sigma_x = 10k^{-1}$ and panels (d) – (f) correspond to simulations of relatively long wavepackets with horizontal extent $\sigma_x = 40k^{-1}$. The vertical bars denote the times, t_Δ , given by (3.17), at which weakly nonlinear effects are predicted to become significant. The curves corresponding to the weakly nonlinear simulations are identical to the black and blue curves in Fig. 4.8, for $\sigma_x = 10k^{-1}$ and $\sigma_x = 40k^{-1}$, respectively.

the leading flank of the wavepacket, although in the fully nonlinear simulation these features develop more slowly, and to greater magnitude than those in the weakly nonlinear simulation.

A plot summarizing the time series $\|\widetilde{M}(t)\|$ for all weakly and fully nonlinear simulations with $H_\rho = 10k^{-1}$ is shown in Fig. 4.13. In each panel, solid and dashed curves correspond to weakly and fully nonlinear simulations, respectively. Simulations of wavepackets using $\sigma_x = 10k^{-1}$ and $\sigma_x = 40k^{-1}$ are shown in panels (a) – (c) and (d) – (f), respectively. In each panel in Fig. 4.13, the solid vertical bars denote the times, t_Δ , at which weakly nonlinear effects are predicted to become significant. That the solid and dashed curves overlap in each panel of Fig. 4.13, during which time wavepackets exhibit linear evolution, indicates excellent agreement between the results of the weakly and fully nonlinear simulations until

$t \approx 100N^{-1}$. Thereafter, in each panel the magnitudes of the wave-induced mean flows from the fully nonlinear simulations diverge from those of the weakly nonlinear simulations.

For the wavepackets with $m = -0.4k$ (Figs. 4.13a,d), the L^2 -norms increase until just beyond $t = 187N^{-1}$ (for $\sigma_x = 10k^{-1}$) and $t = 154N^{-1}$ (for $\sigma_x = 40k^{-1}$), the first times at which wave overturning was recorded by the respective fully nonlinear simulations. The corresponding overturning heights are $z_b = 65.92k^{-1}$ and $z_b = 52.09k^{-1}$ for the simulations with $\sigma_x = 10k^{-1}$ and $\sigma_x = 40k^{-1}$, respectively. These values are approximately 17% and 33% lower, respectively, than the overturning height predicted by linear theory, $z_{b,L} = 78.09k^{-1}$, with $z_{b,L}$ given by (3.18). Though overturning, convection develops after another three buoyancy periods in both simulations (see Sutherland, 2001). Unable to resolve the small, fast convective scales, the code terminates the simulations.

For the wavepackets with $m = -1.4k$ (Figs. 4.13c,f), the L^2 -norms from the fully nonlinear simulations exhibit small increases at $t \approx 120N^{-1}$ indicating that weakly nonlinear effects have become significant. Almost simultaneously, the L^2 -norms from the weakly nonlinear simulations exhibit increases, although the rates of increase and the maximum magnitudes are less than those in the fully nonlinear results. At $t \approx 200N^{-1}$, the weakly and fully nonlinear simulations cease to agree quantitatively, as indicated by the rapid divergence in their respective L^2 -norms at this time. In particular, upon termination of the fully nonlinear simulation using $\sigma_x = 10k^{-1}$ at $t = 254N^{-1}$, we find that $\|\widetilde{M}(254)\| = 5.86$, which is greater than the weakly nonlinear value at this time by $\sim 195\%$. For the fully nonlinear simulation using $\sigma_x = 40k^{-1}$, we find that $\|\widetilde{M}(248)\| = 4.39$, about 500% greater than the corresponding weakly nonlinear value. Overturning was first recorded by the simulations using $\sigma_x = 10k^{-1}$ and $\sigma_x = 40k^{-1}$ at $z_b = 59.65k^{-1}$ and $z_b = 55.78k^{-1}$, respectively. These values are approximately 12% and 5% higher, respectively, than the height predicted by linear theory, $z_{b,L} = 53.17k^{-1}$.

For the wavepackets with $m = -0.7k$ (Figs. 4.13b,e), weakly nonlinear effects become significant at earlier times in the fully nonlinear simulations than the weakly nonlinear simulations. It is remarkable that the L^2 -norm of the induced momentum at the final time step, $t = 190N^{-1}$, of the fully nonlinear simulation using $\sigma_x = 10k^{-1}$ (Fig. 4.13b) is almost identical to the value at this time step in the weakly nonlinear simulation. In particular, the fully nonlinear value of $\|\widetilde{M}(190)\| = 3.01$ is $\sim 94\%$ that of the corresponding weakly nonlinear value.

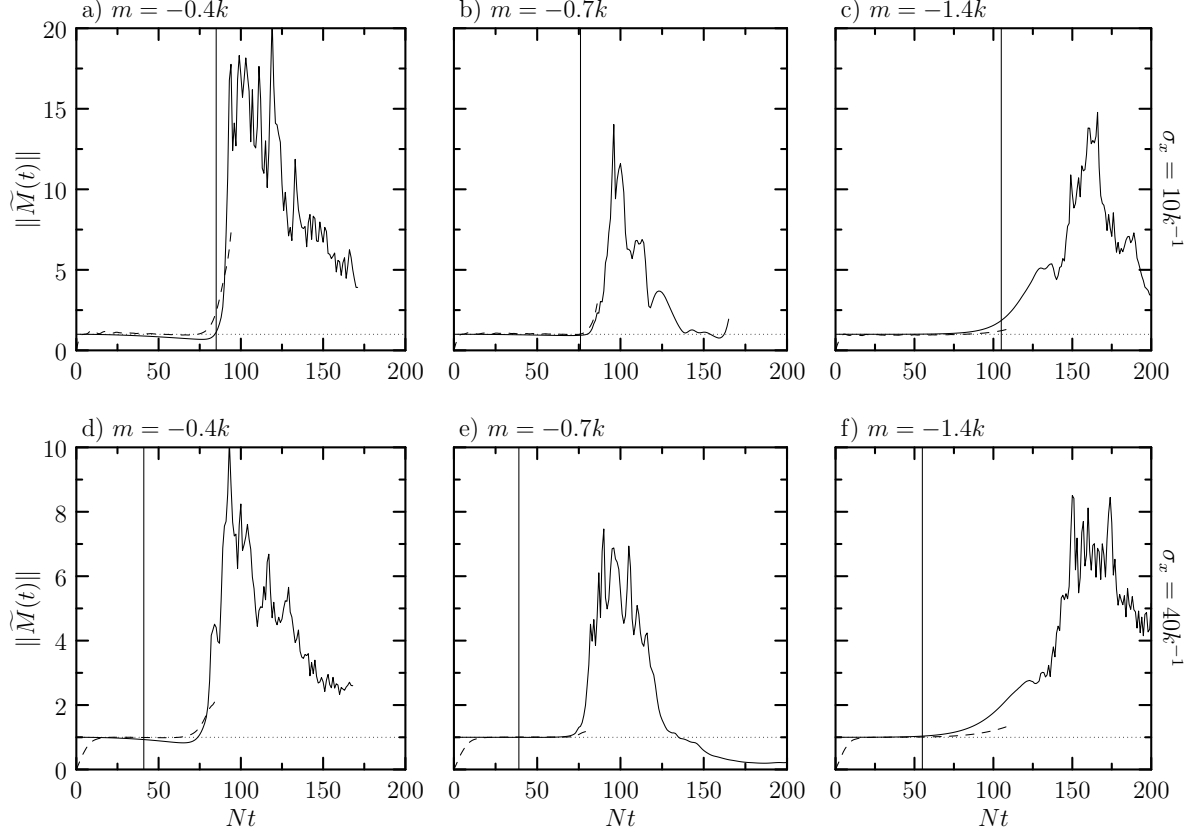


Figure 4.14: As in Fig. 4.13, but for an atmosphere with density scale height $H_\rho = 5k^{-1}$. The solid curves and solid vertical bars corresponding to the weakly nonlinear simulations are identical to those in Fig. 4.9.

Such agreement is likewise observed in the simulations of long wavepackets at $t = 163N^{-1}$ (the fully nonlinear value of $\|\widetilde{M}(163)\| = 2.45$ is $\sim 88\%$ that of the corresponding weakly nonlinear simulation). Overturning was first recorded by the simulations using $\sigma_x = 10k^{-1}$ and $\sigma_x = 40k^{-1}$ at $z_b = 67.38k^{-1}$ and $z_b = 58.07k^{-1}$, respectively. These values are approximately $\sim 0.5\%$ higher and $\sim 13\%$ lower, respectively, than the overturning height predicted by linear theory, $z_b = 67.00k^{-1}$.

A plot summarizing the time series $\|\widetilde{M}(t)\|$ for all weakly and fully nonlinear simulations for which $H_\rho = 5k^{-1}$ is shown in Fig. 4.14. Compared with the corresponding time series for wavepackets with $H_\rho = 10k^{-1}$, the L^2 -norms from the weakly and fully nonlinear simulations with $H_\rho = 5k^{-1}$ tend to more closely overlap at the times during which the respective wavepackets evolve nonlinearly. For wavepackets with $m = -1.4k$ (Figs. 4.14c,f), weakly nonlinear effects become significant in the weakly nonlinear results at earlier times than in the fully nonlinear results, and the L^2 -norms from the weakly nonlinear simulations diverge rapidly

from those of the fully nonlinear simulations. This is opposite the behaviour of the L^2 -norms from the simulations with $H_\rho = 10k^{-1}$ (Figs. 4.13c,f).

For the simulations with $H_\rho = 10k^{-1}$ (Fig. 4.13), in all but the case of the long wavepacket with $m = -1.4k$ (Fig. 4.13f) the times, t_Δ , at which weakly nonlinear effects were predicted to become significant, were severely under-estimated. Agreement between the predicted and actual times at which weakly nonlinear effects became significant was improved in the simulations with $H_\rho = 5k^{-1}$ (Fig. 4.14). In particular, improved agreement is seen in the cases of wavepackets with $m = -0.4k$ and $m = -0.7k$ using $\sigma_x = 10k^{-1}$ (Figs. 4.14a,b, respectively), while good agreement persisted for long wavepackets with $m = -1.4k$ (Fig. 4.14f).

Like the heights at which weakly nonlinear effects became significant, agreement between the predicted and simulated overturning heights for simulations with $H_\rho = 5k^{-1}$ generally improved from the simulations with $H_\rho = 10k^{-1}$. In particular, the overturning heights, z_b , recorded by the simulations with $m = -0.4k$ were 11% lower (for $\sigma_x = 10k^{-1}$) and 21% lower (for $\sigma_x = 40k^{-1}$), respectively, than the height predicted by linear theory, $z_{b,L}$. The overturning heights recorded by the fully nonlinear simulations with $m = -0.7k$ were within 2% higher than $z_{b,L}$. Conversely, agreement between the predicted and simulated overturning heights deteriorated in the results with $m = -1.4k$, with z_b approximately 20% higher than $z_{b,L}$ for wavepackets with horizontal extents $\sigma_x = 10k^{-1}$ and $\sigma_x = 40k^{-1}$.

4.3 Overturning Heights

The results of the fully nonlinear simulations presented in the previous section revealed that nonlinear processes significantly affect wave overturning heights. In particular, waves whose leading flank was prone to narrow and grow in amplitude tended to overturn at a height somewhat below the height predicted by linear theory, while a wavepacket whose trailing flank was prone to narrow and grow acted to retard anelastic growth, causing the wave to overturn at a height just above that predicted by linear theory.

Here, we further investigate how relative vertical wavenumber, density scale height, and horizontal wavepacket extent affect the locations at which waves overturn. The overturning heights recorded by fully nonlinear simulations using a range of relative vertical wavenum-

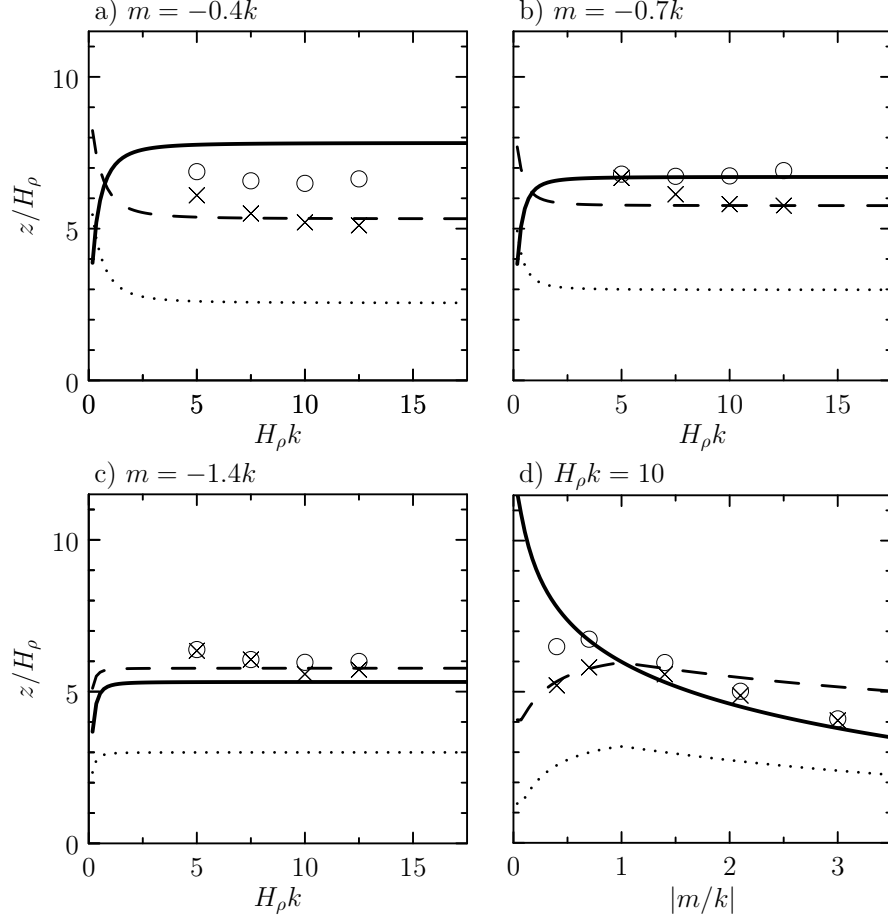


Figure 4.15: Simulated heights at which waves begin to overturn, as computed by the fully nonlinear simulations for wavepackets using a range of horizontal wavepacket extents, density scale heights, and relative vertical wavenumbers m equal to (a) $-0.4k$, (b) $-0.7k$, and (c) $-1.4k$. In (d), the density scale height $H_\rho = 10k^{-1}$ is held fixed and the relative vertical wavenumber is varied. Each simulation was initialized using (3.10) with $A_{\xi_0} = 0.05k^{-1}$ and $\sigma_z = 10k^{-1}$. In each panel, open circles and crosses denote the overturning heights of wavepackets with horizontal extents $\sigma_x = 10k^{-1}$ and $\sigma_x = 40k^{-1}$, respectively. The overturning heights predicted by linear theory, $z_{b,L}$, given by (3.18), are indicated by the solid curves; the heights at which weakly nonlinear effects are predicted to become significant, z_Δ , for $\sigma_x = 10k^{-1}$ and $\sigma_x = 40k^{-1}$ are indicated by the dashed and dotted curves, respectively, with z_Δ given by (3.16).

bers, density scale heights, and horizontal wavepacket extents are shown in Fig. 4.15. Each simulation was initialized using (3.10) with amplitude $A_{\xi_0} = 0.05k^{-1}$ and vertical wavepacket extent $\sigma_z = 10k^{-1}$. The horizontal extent of the wavepacket was set to either $\sigma_x = 10k^{-1}$ (open circles) or $\sigma_x = 40k^{-1}$ (crosses). In Figs. 4.15a,b,c, the relative vertical wavenumbers m are set to $-0.4k$, $-0.7k$, and $-1.4k$, respectively, while the density scale height, H_ρ , is varied. Fig. 4.15d combines the results from Figs. 4.15a,b,c for the fixed density scale height $H_\rho = 10k^{-1}$. In each panel of Fig. 4.15, the solid curves indicate the overturning heights, $z_{b,L}$, predicted by linear theory as given in (3.18); the dashed curves indicate the heights, z_Δ ,

at which weakly nonlinear effects are predicted to become significant for wavepackets with $\sigma_x = 10k^{-1}$; and the dotted curves are the same, but for relatively long wavepackets, for which $\sigma_x = 40k^{-1}$, with z_Δ given by (3.16).

As anticipated for wavepackets with $m = -0.4k$ (Fig. 4.15a), modulational instability along the leading flank of the wavepacket, enhanced by anelastic growth, causes the wavepackets to overturn at a height somewhat below that predicted by linear theory. Relatively long wavepackets overturn at lower heights than those for which $\sigma_x = 10k^{-1}$, in part due to the earlier onset of weakly nonlinear effects owing to their initial wave-induced mean flow being approximately four times greater in magnitude, as predicted by (A.16).

Conversely, wavepackets with $m = -1.4k$ (Fig. 4.15c) overturn just above the heights predicted by linear theory. Here, the effects of modulational instability are focused along the trailing flank and enhanced by anelastic growth. Simultaneously, anelastic growth on the leading flank is comparatively stronger, but is partially inhibited by spreading due to modulational stability on the leading flank. Hence we find that the trailing flank of the wavepacket grows to an overturning amplitude at earlier times than the leading flank (which may not necessarily overturn at all).

For wavepackets with $m = -0.7k$ (Fig. 4.15b), the wavepackets with $\sigma_x = 10k^{-1}$ overturn at almost exactly the height predicted by linear theory, and long wavepackets overturn at or below the predicted heights. Having relative vertical wavenumber $|m/k| \lesssim \tilde{m}_*$ means that modulational instability favours growth on the leading flank of the wavepackets, but only just.

Combining the results, Fig. 4.15d shows that as the absolute value of the relative vertical wavenumber increases, the simulated overturning heights for wavepackets using $\sigma_x = 10k^{-1}$ and $\sigma_x = 40k^{-1}$ tend toward the overturning heights predicted by linear theory. This is opposite the results of DS11 for one-dimensional wavepackets, who showed that as the relative vertical wavenumber increased in absolute value, the simulated overturning heights became progressively higher than the overturning heights predicted by linear theory. We also see that for relative vertical wavenumbers $|m/k| \gtrsim 1.6$ the simulated overturning heights are below the heights at which weakly nonlinear effects are predicted to become significant (for wavepackets with $\sigma_x = 10k^{-1}$), suggesting that these linear theory predictions are particularly poor for such wavenumbers.

Chapter 5

Discussion and Conclusion

In this thesis, I have derived the expression for the horizontal mean flow induced by horizontally and vertically localized internal gravity wavepackets in an anelastic gas, and derived the nonlinear Schrödinger equations for the weakly nonlinear evolution of such waves in both a Boussinesq and an anelastic gas. I described the weakly nonlinear code I developed to solve the anelastic nonlinear Schrödinger equation, and I compared its results to those of fully nonlinear simulations using a range of wavepacket and atmospheric parameters. I elucidated the effects of weakly nonlinear dynamics on wave overturning height, and I compared the overturning heights recorded by the fully nonlinear simulations to those predicted through the use of linear anelastic theory.

It has been shown that two-dimensional wavepackets are modulationally unstable for any relative vertical wavenumber. This is because the wave-induced mean flow for two-dimensional wavepackets changes sign from the leading flank to the trailing flank of the wavepacket. As such, whether narrowing and relative amplitude growth is focused on the leading flank or the trailing flank is determined by a combination of the relative vertical wavenumber (and hence the waves' frequency) and the sign of the wave-induced mean flow. In particular, waves whose initial frequency was greater than the critical frequency ω_* exhibited wave accumulation on the leading flank of the wavepacket, which, combined with anelastic growth, caused the waves to overturn at a height somewhat below that predicted by linear theory. Conversely, waves with initial frequency lower than ω_* exhibited wave accumulation on the trailing flank, causing the waves to overturn at a height just above that predicted by linear theory. The boundary separating these regimes was set by the critical “transition vertical wavenumber”, m_* . Waves

with relative vertical wavenumber equal to m_* in absolute value correspond to waves having the fastest vertical group speed. As such, for $kH_\rho \gg 1$, we find that $|m_*| \approx |k|/\sqrt{2}$ and the corresponding critical frequency is $\omega_* \approx \sqrt{2/3}N \approx 0.8N$.

It was also shown that two-dimensional waves are unstable to horizontal modulations. Unlike modulations in the vertical, the sign of the wave-induced mean flow alone determined whether the leading flank or the trailing flank of the wavepacket was prone to horizontal narrowing and relative amplitude growth or horizontal spreading and relative amplitude decay. In particular, on the leading flank where $U(z, t) > 0$, the waves exhibited accumulation, and on the trailing flank where $U(z, t) < 0$, the waves exhibited spreading. These effects tended to be significantly less pronounced than the effects of vertical modulations, except at late times in the evolution of a wavepacket with relative vertical wavenumber $m = -1.4k$ (e.g. Fig. 4.3d).

Two-dimensional wavepackets exhibit a phenomenon I have named “oblique dispersion”, in which a wavepacket appears to ‘tilt’ in the clockwise direction as it propagates. It was shown that this behaviour is caused by the terms in the nonlinear Schrödinger equation containing mixed x - and z -derivatives of the amplitude function. The dynamical effect of such terms was suspected intuitively, knowing that the terms containing derivatives purely in either x or z represent dispersion in their respective directions. Conversely, the existence of oblique dispersion is not suspected from such a cursory examination of the fully nonlinear equations of motion. Weakly nonlinear simulations revealed that oblique dispersion was most pronounced for wavepackets with relative vertical wavenumber $m = -0.4k$, and became progressively less pronounced as the waves became more hydrostatic (Fig. 4.4). Taken together, these results re-iterate the value of weakly nonlinear theory and simulations.

Through comparisons of the numerically integrated solutions of the nonlinear Schrödinger equation with those of the fully nonlinear equations of motion, it was shown that the weakly nonlinear evolution of horizontally and vertically localized wavepackets in an anelastic gas was well captured by a nonlinear Schrödinger equation describing only the translation and dispersion of wavepackets, and their interactions with their induced mean flow. Qualitative and quantitative similarities among time series of the centreline wave-induced mean flow profiles from weakly and fully nonlinear simulations revealed that weakly nonlinear theory

well captures the dynamics of internal gravity wavepackets during their early- to mid-life evolution, during which their amplitude grows from relatively small to moderately large. It was found that as the relative vertical wavenumber increased in absolute value, qualitative agreement between the weakly and fully nonlinear results persisted to progressively later times in the wavepackets' evolution. In particular, in a pair of simulations of a wavepacket with $m = -1.4k$ (Fig. 4.11c), such qualitative agreement endured for over eight buoyancy periods after wave overturning was first recorded by the fully nonlinear simulation. This duration represents over 20% of the total duration of the fully nonlinear simulation. However, quantitative agreement became questionable (Fig. 4.13c).

For comparison of our results with those for a one-dimensional anelastic wavepacket, let us re-visit the example considered by DS11. We consider a model atmosphere with density scale height $H_\rho = 10$ km. Setting $kH_\rho = 10$ yields a horizontal wavelength of $\lambda_x \approx 6.28$ km. Choosing a relative vertical wavenumber of $m = -3.0k$ yields a vertical wavelength of $\lambda_z \approx 2.09$ km. An initial vertical displacement amplitude of $A_{\xi_0} = 0.05k^{-1}$ corresponds to an actual peak displacement of 50 m near the source of wavepacket generation. The results of DS11 suggest that if the wavepacket is horizontally periodic and vertically localized, the waves should overturn after propagating upward approximately 11 density scale heights, nearly 190% higher than the height predicted by linear theory. Conversely, if the wavepacket is horizontally and vertically localized, our results suggest the waves should overturn after propagating upward only 4 density scale heights. This overturning height is $\sim 5\%$ higher than that predicted by linear theory, which corresponds to a difference in overturning heights of ~ 530 m in our model atmosphere. Alternatively, suppose the relative vertical wavenumber is $m = -0.4k$. This corresponds to a vertical wavelength of $\lambda_z \approx 15.7$ km, and the overturning height predicted by linear theory is higher than our simulated overturning height by ~ 12.8 km.

The results presented in Chapter 4 and the illustrative example considered above demonstrate that the overturning heights predicted by linear theory can be unreliable. Furthermore, it was found that in the majority of cases, the times at which weakly nonlinear effects were predicted to become significant (which were likewise derived using linear theory) were generally poor predictors of the actual times at which weakly nonlinear effects became significant.

In some physically suspect cases, waves were predicted to overturn *earlier than* the predicted onset of weakly nonlinear effects (Fig. 4.15d). This re-iterates the possible dangers of relying on predictions based on linear theory.

In agreement with previous studies of Boussinesq wavepackets (Bretherton, 1969; Sutherland, 2001; Tabaei and Akylas, 2007; van den Bremer and Sutherland, 2014), the qualitative behaviour of two-dimensional anelastic wavepackets is different than that of one-dimensional anelastic wavepackets. Recent studies (Tabaei and Akylas, 2007; van den Bremer and Sutherland, 2018) have revealed that fully three-dimensional (horizontally, vertically, and spanwise localized) Boussinesq wavepackets behave differently again. In order to gain a more complete understanding of atmospheric internal gravity waves, much work remains to be done. In particular, fully and weakly nonlinear three-dimensional models of internal gravity waves should be developed to include the effects of Coriolis forces, non-uniform stratification, and background wind shear. This is the goal of doctoral research I have recently begun. The anticipated resulting models will thus include a more realistic range of features present in the actual atmosphere. Incorporating these features into models will enable a more comprehensive understanding of the processes affecting internal gravity wave dynamics, with the intent ultimately to develop more realistic internal gravity wave drag parameterization schemes.

Bibliography

- Acheson, D. J., 1976: On over-reflexion. *J. Fluid Mech.*, **77**, 433–472.
- Akylas, T. R., and A. Tabaei, 2005: Resonant self-acceleration and instability of nonlinear internal gravity wavetrains. *Frontiers of Nonlinear Physics*, A. Litvak, Ed., Institute of Applied Physics, 129–135.
- Allen, M. B., and E. L. Isaacson, 1998: *Numerical Analysis for Applied Science*. Wiley-Interscience, New York, USA, 492 pp.
- Beck, M., G. Marchesi, D. Pixton, and L. Sabalka, 2014: A first course in complex analysis version 1.41. n.p., accessed: 2015-01-06, 128 pp., <http://www.math.binghamton.edu/dennis/complex.pdf>.
- Benjamin, T. B., and J. E. Feir, 1967: The disintegration of wavetrains on deep water. Part 1. Theory. *J. Fluid Mech.*, **27**, 417–430.
- Bretherton, F. P., 1966: The propagation of groups of internal gravity waves in a shear flow. *Quart. J. Roy. Meteorol. Soc.*, **92**, 466–480.
- Bretherton, F. P., 1969: On the mean motion induced by gravity waves. *J. Fluid Mech.*, **36** (4), 785–803.
- Cauchy, A. L., 1827: Mémoire sur les intégrales définies. *Mémoires Présentés par Divers Savans a l'Académie des Sciences de l'Institut de France*, **1**, 599–799, lu à l'Institut le 22 août, 1814.
- Churchill, R. V., and J. W. Brown, 1984: *Complex Variables and Applications*. 4th ed., McGraw-Hill, New York, USA, 339 pp.

- Dosser, H. V., 2010: Propagation of nonlinear internal gravity waves. M.S. thesis, Dept. of Physics, University of Alberta, 99 pp.
- Dosser, H. V., and B. R. Sutherland, 2011: Anelastic internal wavepacket evolution and stability. *J. Atmos. Sci.*, **68**, 2844–2859.
- Dunkerton, T. J., 1981: Wave transience in a compressible atmosphere. Part I: Transient internal wave, mean-flow interaction. *J. Atmos. Sci.*, **38**, 281–297.
- Durran, D. R., 2010: *Numerical Methods for Fluid Dynamics*. 2nd ed., Springer-Verlag, New York, USA, 516 pp.
- Dutton, J. A., and G. H. Fichtl, 1969: Approximate equations of motion for gases and liquids. *J. Atmos. Sci.*, **26**, 241–254.
- Eliassen, A., and E. Palm, 1961: On the transfer of energy in stationary mountain waves. *Geofys. Publ.*, **22**, 1–23.
- Fermi, E., J. Pasta, and S. Ulam, 1974: Studies of nonlinear problems I, Los Alamos Report LA 1940, 1955. reproduced in *Nonlinear Wave Motion*, A. C. Newell, Ed., Amer. Math. Soc., Providence, RI, 143–156.
- Fritts, D. C., 1982: Shear excitation of atmospheric gravity waves. *J. Atmos. Sci.*, **39**, 1936–1952.
- Fritts, D. C., and T. J. Dunkerton, 1984: A quasi-linear study of gravity-wave saturation and self-acceleration. *J. Atmos. Sci.*, **41**, 3272–3289.
- Grimshaw, R. H. J., 1975: Nonlinear internal gravity waves and their interaction with the mean wind. *J. Atmos. Sci.*, **32**, 1779–1793.
- Holton, J. R., and G. J. Hakim, 2013: *An Introduction to Dynamic Meteorology*. 5th ed., Academic Press, Waltham, USA, 532 pp.
- Jones, W. L., and D. D. Houghton, 1971: The coupling of momentum between internal gravity waves and mean flow: A numerical study. *J. Atmos. Sci.*, **28**, 604–608.

- Klein, R., 2009: Asymptotics, structure, and integration of sound-proof atmospheric flow equations. *Theo. Comp. Fluid Dyn.*, **23**, 161–195, doi:10.1007/s00162-009-0104-y.
- Kundu, P. K., I. M. Cohen, D. R. Dowling, and G. Tryggvason, 2016: *Fluid Mechanics*. 6th ed., Academic Press, London, UK, 921 pp.
- Lake, B. M., H. C. Yuen, H. Rundgaldier, and W. E. Ferguson, 1977: Nonlinear deep-water waves: Theory and experiment, Part 2, Evolution of a continuous wave train. *J. Fluid Mech.*, **83**, 49–74.
- Lindzen, R. S., 1981: Turbulence and stress owing to gravity wave and tidal breakdown. *J. Geophys. Res.*, **86**, 9707–9714.
- Lipps, F. B., and R. S. Hemler, 1982: A scale analysis of deep moist convection and some related numerical calculations. *J. Atmos. Sci.*, **39** (10), 2192–2210.
- McFarlane, N. A., 1987: The effect of orographically excited gravity wave drag on the general circulation of the lower stratosphere and troposphere. *J. Atmos. Sci.*, **44**, 1775–1800.
- McLandress, C., 1998: On the importance of gravity waves in the middle atmosphere and their parameterization in general circulation models. *J. Atmos. Sol.-Terr. Phys.*, **60**, 1357–1383.
- Ogura, Y., and N. A. Phillips, 1962: Scale analysis of deep and shallow convection in the atmosphere. *J. Atmos. Sci.*, **19**, 173–179.
- Palmer, T. N., G. J. Shutts, and R. Swinbank, 1986: Alleviation of a systematic westerly bias in general circulation and numerical weather prediction models through an orographic gravity wave drag parametrization. *Quart. J. Roy. Meteor. Soc.*, **112**, 1001–1039.
- Phillips, O. M., 1981: Wave interactions – the evolution of an idea. *J. Fluid Mech.*, **106**, 215–227.
- Press, W. H., S. A. Teukolsky, W. T. Vetterling, and B. P. Flannery, 2007: *Numerical Recipes: The Art of Scientific Computing*. 3rd ed., Cambridge University Press, New York, USA, 1235 pp.

- Scinocca, J. F., and N. A. McFarlane, 2000: The parameterization of drag induced by stratified flow of anisotropic orography. *Quart. J. Roy. Meteor. Soc.*, **126**, 2353–2393.
- Scinocca, J. F., and T. G. Shepherd, 1992: Nonlinear wave-activity conservation laws and Hamiltonian structure for the two-dimensional anelastic equations. *J. Atmos. Sci.*, **49**, 5–27.
- Shrira, V. I., 1981: On the propagation of a three-dimensional packet of weakly non-linear internal gravity waves. *Int. J. Non-Linear Mechanics*, **16**, 129–138.
- Stokes, G. G., 1847: On the theory of oscillatory waves. *Trans. Camb. Philos. Soc.*, **8**, 441–455.
- Sutherland, B. R., 2001: Finite-amplitude internal wavepacket dispersion and breaking. *J. Fluid Mech.*, **429**, 343–380.
- Sutherland, B. R., 2006a: Internal wave instability: Wave-wave vs wave-induced mean flow interactions. *Phys. Fluids.*, **18**, 074 107:1–8, doi:10.1063/1.2219102.
- Sutherland, B. R., 2006b: Weakly nonlinear internal gravity wavepackets. *J. Fluid Mech.*, **569**, 249–258.
- Sutherland, B. R., 2010: *Internal Gravity Waves*. Cambridge University Press, Cambridge, UK, 378 pp.
- Tabaei, A., and T. R. Akylas, 2007: Resonant long-short wave interactions in an unbounded rotating stratified fluid. *Stud. Appl. Maths*, **119**, 271–296.
- Vallis, G. K., 2006: *Atmospheric and Oceanic Fluid Dynamics*. Cambridge University Press, Cambridge, England, 745 pp.
- van den Bremer, T. S., and B. R. Sutherland, 2014: The mean flow and long waves induced by two-dimensional internal gravity wavepackets. *Phys. Fluids*, **26**, 106 601:1–23, doi:10.1063/1.4899262.
- van den Bremer, T. S., and B. R. Sutherland, 2018: The wave-induced flow of wide three-dimensional internal gravity wavepackets. *J. Fluid Mech.*, **834**, 385–408, doi:10.1017/jfm.2017.745.

Whitham, G. B., 1974: *Linear and Nonlinear Waves*. John Wiley and Sons, Inc., New York, USA, 636 pp.

Appendix A

Residue Theory Details

Presented here are the detailed computations and intermediate steps involved in integrating (2.26) with respect to κ using residue theory. The task involves expressing the integral in a way that is amenable to integration using residue theory, performing the integration, and demonstrating that the imaginary parts of the results vanish. Also included is an example to illustrate the functionality of the method.

A.1 Problem Set-Up and Integration

For reference let us define the integrand of (2.26) as

$$G(\kappa; \mu) := \frac{-1}{\kappa^2 - \frac{c_{g_z}^2}{N^2} \left[\mu^4 - i \frac{1}{H_\rho} \mu^3 \right]}. \quad (\text{A.1})$$

We observe that $G(\kappa; \mu)$, and hence (2.26), has complex singularities along the two curves defined by the right-hand side of

$$\kappa = \pm \frac{|c_{g_z}|}{N} \left[\mu^4 - i \frac{1}{H_\rho} \mu^3 \right]^{1/2} := \pm C(\mu).$$

It is necessary to determine the intervals on which the imaginary part of $C(\mu)$ is positive or negative to ensure the inverse transform of (2.26) will remain bounded. We begin by analyzing the square root term in $C(\mu)$, which may be written as $\sqrt{re^{i\Phi'}} = \sqrt{r}e^{i\Phi'/2}$, in which

$$r(\mu) = \left| \mu^4 - i \frac{1}{H_\rho} \mu^3 \right| = \sqrt{\mu^8 + \mu^6/H_\rho^2};$$

$$\frac{1}{2}\Phi'(\mu) = \frac{1}{2} \tan^{-1} \left(-\frac{\mu^3}{H_\rho} \frac{1}{\mu^4} \right) = -\frac{1}{2} \tan^{-1}(1/H_\rho\mu) := \Phi,$$

using standard methods from complex analysis. Taken together we have

$$C(\mu) = \frac{|c_{gz}|}{N} \left[\mu^8 + \frac{1}{H_\rho^2} \mu^6 \right]^{1/4} (\cos \Phi + i \sin \Phi) = C_R + iC_I, \quad (\text{A.2})$$

in which the subscripts R and I respectively denote the real and imaginary parts of $C(\mu)$. From the range of arctangent it is clear that $-\frac{\pi}{4} < \Phi < \frac{\pi}{4}$ and $\Phi \neq 0$. Whether each curve of singularities is located in the upper or lower half of the complex plane follows from these facts according to the sign of $\sin \Phi$, and hence the sign of μ . Indeed,

$$\mu < 0 \Rightarrow \sin \Phi > 0;$$

$$\mu > 0 \Rightarrow \sin \Phi < 0.$$

Using (A.2) we decompose the denominator in $G(\kappa; \mu)$, given by (A.1), allowing us to express (2.26) as

$$\Psi^{(2)} = \frac{i}{4} \rho_0 \frac{Nk^2 m^2}{K^5} A_0^2 \int_{\mathbb{R}} \frac{\mu^3 e^{i\mu\bar{z}}}{C(\mu)} \left[\underbrace{\int_{\mathbb{R}} |\mathcal{A}|^2 e^{i\kappa\bar{x}} \left[\frac{1}{\kappa + C(\mu)} - \frac{1}{\kappa - C(\mu)} \right] d\kappa}_{:=I(\kappa; \mu)} \right] d\mu. \quad (\text{A.3})$$

In order to apply residue theory when integrating with respect to κ , we first make a change of variables $\kappa \rightarrow \mathfrak{z} = \mathfrak{z}_R + i\mathfrak{z}_I \in \mathbb{C}$, where \mathfrak{z} is necessary for constructing contours around each curve of singularities. Let $\Gamma_{+,+}$ be the positively oriented, piecewise-smooth semicircular curve of radius R in the upper half-plane such that the line segment from $-R$ to R lies on the κ axis and is centred at the origin. Let $\Gamma_{+,-}$ be analogous to $\Gamma_{+,+}$ but in the lower half-plane, and negatively oriented. Let $\Gamma_{-,-}$ be the negatively oriented analogue of $\Gamma_{+,+}$ and let $\Gamma_{-,+}$ be the positively oriented analogue of $\Gamma_{+,-}$. Explicitly,

$$\Gamma_{+,+} = \{-R \leq \kappa \leq R\} \cup \{\mathfrak{z} = Re^{i\tau}, 0 \leq \tau \leq \pi\} = \{-R \leq \kappa \leq R\} \cup \gamma_{+,+}; \quad (\text{A.4a})$$

$$\Gamma_{+,-} = \{-R \leq \kappa \leq R\} \cup \{\mathfrak{z} = Re^{-i\tau}, 0 \leq \tau \leq \pi\} = \{-R \leq \kappa \leq R\} \cup \gamma_{+,-}; \quad (\text{A.4b})$$

$$\Gamma_{-,-} = \{-R \leq \kappa \leq R\} \cup \{\mathfrak{z} = -Re^{i\tau}, 0 \leq \tau \leq \pi\} = \{-R \leq \kappa \leq R\} \cup \gamma_{-,-}; \quad (\text{A.4c})$$

$$\Gamma_{-,+} = \{-R \leq \kappa \leq R\} \cup \{\mathfrak{z} = -Re^{-i\tau}, 0 \leq \tau \leq \pi\} = \{-R \leq \kappa \leq R\} \cup \gamma_{-,+}. \quad (\text{A.4d})$$

In order to integrate over \mathbb{R} we will let $R \rightarrow \infty$. Decomposing the denominator in (2.26),

making the change of variables $\kappa \rightarrow \mathfrak{z}$, and explicitly separating the integrals with respect to \mathfrak{z} and μ , we have

$$\Psi^{(2)} = \frac{i}{4} \rho_0 \frac{Nk^2 m^2}{K^5} A_0^2 \int_{\mathbb{R}} \frac{\mu^3 e^{i\mu\tilde{x}}}{C(\mu)} \left[\oint_{\Gamma_{\pm,\pm}} |\widehat{\mathcal{A}}|^2 e^{i\mathfrak{z}\tilde{x}} \left[\frac{1}{\mathfrak{z} + C(\mu)} - \frac{1}{\mathfrak{z} - C(\mu)} \right] d\mathfrak{z} \right] d\mu. \quad (\text{A.5})$$

Factors of the form $e^{\pm iC(\mu)\tilde{x}}$ will appear in the μ -dependent integrand following the application of residue theory. The boundedness of these terms (and hence the boundedness of the inverse Fourier transform with respect to κ) depends on the choice of $\Gamma_{\pm,\pm}$, a choice which must take into consideration the signs of \tilde{x} and μ . It was found that the convergence of the integral over $[-R, R]$ is determined by the choice of the second \pm sign in $\Gamma_{\pm,\pm}$, and the integral over the arc, γ , is determined by the choice of the first \pm sign in $\Gamma_{\pm,\pm}$.

For reference, denote the contour integral in (A.5) by

$$I_{\kappa}(\mathfrak{z}; \mu) := \oint_{\Gamma_{\pm,\pm}} |\widehat{\mathcal{A}}|^2 e^{i\mathfrak{z}\tilde{x}} \left[\frac{1}{\mathfrak{z} + C(\mu)} - \frac{1}{\mathfrak{z} - C(\mu)} \right] d\mathfrak{z}.$$

For the time being, let $h(\mathfrak{z}; \mu)$ denote either of the two terms obtained by distributing the factor $|\widehat{\mathcal{A}}|^2 e^{i\mathfrak{z}\tilde{x}}$ into the bracketed terms in $I_{\kappa}(\mathfrak{z}; \mu)$. Since the $\Gamma_{\pm,\pm}$ are constructed as the union of two curves, the integral of $h(\mathfrak{z}; \mu)$ may be written as either

$$\oint_{\Gamma_{+,\pm}} h(\mathfrak{z}; \mu) d\mathfrak{z} = \int_{-R}^R h(\kappa; \mu) d\kappa + \int_{\gamma_{+,\pm}} h(\mathfrak{z}; \mu) d\mathfrak{z} = b_{\Gamma} 2\pi i \text{Res}(h(\mathfrak{z}; \mu)); \quad (\text{A.6a})$$

$$\oint_{\Gamma_{-,\pm}} h(\mathfrak{z}; \mu) d\mathfrak{z} = - \int_{-R}^R h(\kappa; \mu) d\kappa + \int_{\gamma_{-,\pm}} h(\mathfrak{z}; \mu) d\mathfrak{z} = b_{\Gamma} 2\pi i \text{Res}(h(\mathfrak{z}; \mu)), \quad (\text{A.6b})$$

where b_{Γ} takes a fixed value of 1 or -1 according to the orientation of $\Gamma_{\pm,\pm}$. The presence of the negative sign leading the integral over $[-R, R]$ in (A.6b) is due to the orientation of $\Gamma_{-,\pm}$, which causes the part of the curve along the real axis to begin at R and end at $-R$. The negative sign arises upon reversing the bounds of integration.

If the singularity is a pole, the general formula for computing its residue (Cauchy, 1827; Beck et al., 2014) is

$$\text{Res}_{\mathfrak{z}=\mathfrak{z}_0}(h(\mathfrak{z}; \mu)) = \frac{1}{(n-1)!} \lim_{\mathfrak{z} \rightarrow \mathfrak{z}_0} \frac{d^{n-1}}{d\mathfrak{z}^{n-1}} ((\mathfrak{z} - \mathfrak{z}_0)^n h(\mathfrak{z}; \mu)), \quad (\text{A.7})$$

where n is the order of the pole and \mathfrak{z}_0 is the value of the singularity. Crucially, we consider

$\pm C(\mu)$ to behave like poles of order 1, so (A.7) simplifies to

$$\operatorname{Res}(h(\mathfrak{z}; \mu)) = \lim_{\mathfrak{z} \rightarrow \mathfrak{z}_0} ((\mathfrak{z} - \mathfrak{z}_0)h(\mathfrak{z}; \mu)). \quad (\text{A.8})$$

Use of (A.8) will be partly justified *a posteriori*, as this residue-theoretical approach will be shown via example in §A.3 to produce results consistent with the numerical methods described in §3.2.4. On the right-hand side of (A.8), multiplication by $\mathfrak{z} - \mathfrak{z}_0$ has the effect of eliminating the singularity from the denominator of $h(\mathfrak{z}; \mu)$. Taking the limit of the resulting function as $\mathfrak{z} \rightarrow \mathfrak{z}_0$ results in replacing functional dependence on \mathfrak{z} with dependence on $\mathfrak{z}_0 = \pm C(\mu)$. With this in mind we now determine which contour will be used to integrate over each singularity taking into consideration the signs of μ and \tilde{x} as per the following analysis.

1. Consider the singularity $\mathfrak{z} + C(\mu) = 0 \Leftrightarrow \mathfrak{z} = -C(\mu)$:

(a) $\mu < 0 \Rightarrow -C_I < 0$:

- i. If $\tilde{x} > 0$, then $\operatorname{Re}\{e^{i\mathfrak{z}\tilde{x}}\} = e^{C_I\tilde{x}} \rightarrow \infty$. Avoid this by integrating over $\Gamma_{+,+}$.
- ii. If $\tilde{x} < 0$, then $\operatorname{Re}\{e^{i\mathfrak{z}\tilde{x}}\} = e^{C_I\tilde{x}} < 1$. Achieve this by integrating over $\Gamma_{+,-}$.

(b) $\mu > 0 \Rightarrow -C_I > 0$

- i. If $\tilde{x} > 0$, then $\operatorname{Re}\{e^{i\mathfrak{z}\tilde{x}}\} = e^{C_I\tilde{x}} < 1$. Achieve this by integrating over $\Gamma_{+,+}$.
- ii. If $\tilde{x} < 0$, then $\operatorname{Re}\{e^{i\mathfrak{z}\tilde{x}}\} = e^{C_I\tilde{x}} \rightarrow \infty$. Avoid this by integrating over $\Gamma_{+,-}$.

2. Consider the singularity $\mathfrak{z} - C(\mu) = 0 \Leftrightarrow \mathfrak{z} = C(\mu)$:

(a) $\mu < 0 \Rightarrow C_I > 0$:

- i. If $\tilde{x} > 0$, then $\operatorname{Re}\{e^{i\mathfrak{z}\tilde{x}}\} = e^{-C_I\tilde{x}} < 1$. Achieve this by integrating over $\Gamma_{-,-}$.
- ii. If $\tilde{x} < 0$, then $\operatorname{Re}\{e^{i\mathfrak{z}\tilde{x}}\} = e^{-C_I\tilde{x}} \rightarrow \infty$. Avoid this by integrating over $\Gamma_{-,+}$.

(b) $\mu > 0 \Rightarrow C_I < 0$

- i. If $\tilde{x} > 0$, then $\operatorname{Re}\{e^{i\mathfrak{z}\tilde{x}}\} = e^{-C_I\tilde{x}} \rightarrow \infty$. Avoid this by integrating over $\Gamma_{-,-}$.
- ii. If $\tilde{x} < 0$, then $\operatorname{Re}\{e^{i\mathfrak{z}\tilde{x}}\} = e^{-C_I\tilde{x}} < 1$. Achieve this by integrating over $\Gamma_{-,+}$.

This analysis motivates a clarification of our notation: henceforth let

$$h_1(\mathfrak{z}; \mu) = \frac{|\widehat{\mathcal{A}}|^2 e^{i\mathfrak{z}\tilde{x}}}{\mathfrak{z} + C(\mu)} \quad \text{and} \quad h_2(\mathfrak{z}; \mu) = \frac{|\widehat{\mathcal{A}}|^2 e^{i\mathfrak{z}\tilde{x}}}{\mathfrak{z} - C(\mu)}.$$

Here, the subscripts 1 and 2 refer respectively to the first and second terms in the bracketed part of $I_\kappa(\mathfrak{z}; \mu)$. The integral of $I(\kappa; \mu)$ with respect to κ , defined in the right-hand side of (A.3), follows upon rearrangement of (A.6a) and (A.6b). For $\mu < 0$ we have

$$\int_{\mathbb{R}} h_1(\kappa; \mu) d\kappa = \begin{cases} - \int_{\gamma_{+,+}} h_1(\mathfrak{z}; \mu) d\mathfrak{z}, & \tilde{x} > 0; \\ -2\pi i \operatorname{Res}_{\mathfrak{z}=-C(\mu)}(h_1(\mathfrak{z}; \mu)) - \int_{\gamma_{+,-}} h_1(\mathfrak{z}; \mu) d\mathfrak{z}, & \tilde{x} < 0, \end{cases} \quad (\text{A.9a})$$

$$\int_{\mathbb{R}} h_2(\kappa; \mu) d\kappa = \begin{cases} 2\pi i \operatorname{Res}_{\mathfrak{z}=C(\mu)}(h_2(\mathfrak{z}; \mu)) + \int_{\gamma_{-,-}} h_2(\mathfrak{z}; \mu) d\mathfrak{z}, & \tilde{x} > 0; \\ \int_{\gamma_{-,+}} h_2(\mathfrak{z}; \mu) d\mathfrak{z}, & \tilde{x} < 0. \end{cases} \quad (\text{A.9b})$$

Similarly, for $\mu > 0$ we have

$$\int_{\mathbb{R}} h_1(\kappa; \mu) d\kappa = \begin{cases} 2\pi i \operatorname{Res}_{\mathfrak{z}=-C(\mu)}(h_1(\mathfrak{z}; \mu)) - \int_{\gamma_{+,+}} h_1(\mathfrak{z}; \mu) d\mathfrak{z}, & \tilde{x} > 0; \\ - \int_{\gamma_{+,-}} h_1(\mathfrak{z}; \mu) d\mathfrak{z}, & \tilde{x} < 0, \end{cases} \quad (\text{A.9c})$$

$$\int_{\mathbb{R}} h_2(\kappa; \mu) d\kappa = \begin{cases} \int_{\gamma_{-,-}} h_2(\mathfrak{z}; \mu) d\mathfrak{z}, & \tilde{x} > 0; \\ -2\pi i \operatorname{Res}_{\mathfrak{z}=C(\mu)}(h_2(\mathfrak{z}; \mu)) - \int_{\gamma_{-,+}} h_2(\mathfrak{z}; \mu) d\mathfrak{z}, & \tilde{x} < 0, \end{cases} \quad (\text{A.9d})$$

in which we have explicitly omitted residues evaluating to zero. It is shown in §A.2 that the integrals over the arcs, $\gamma_{\pm,\pm}$, in (A.9a) – (A.9d) vanish as $R \rightarrow \infty$, given that the correct contour $\Gamma_{\pm,\pm}$ was chosen as per the analysis presented above. Accordingly the results of the integrations for $\mu < 0$ are

$$\int_{\mathbb{R}} I(\kappa; \mu) d\kappa = -2\pi i \times \begin{cases} e^{iC(\mu)\tilde{x}} \widehat{|\mathcal{A}|^2} \Big|_{\mathfrak{z}=C(\mu)}, & \tilde{x} > 0; \\ e^{-iC(\mu)\tilde{x}} \widehat{|\mathcal{A}|^2} \Big|_{\mathfrak{z}=-C(\mu)}, & \tilde{x} < 0, \end{cases} \quad (\text{A.10a})$$

which are obtained by combining (A.9a) and (A.9b). Similarly, the results of the integrations for $\mu > 0$ are

$$\int_{\mathbb{R}} I(\kappa; \mu) d\kappa = 2\pi i \times \begin{cases} e^{-iC(\mu)\tilde{x}} \widehat{|\mathcal{A}|^2} \Big|_{\mathfrak{z}=-C(\mu)}, & \tilde{x} > 0; \\ e^{iC(\mu)\tilde{x}} \widehat{|\mathcal{A}|^2} \Big|_{\mathfrak{z}=C(\mu)}, & \tilde{x} < 0, \end{cases} \quad (\text{A.10b})$$

which are obtained by combining (A.9c) and (A.9d). Substituting (A.10a) and (A.10b) into

the right-hand side of (A.3), then expressing both regions in μ under a single integral sign, yields the following integral expression for the induced mass-streamfunction in real space:

$$\Psi^{(2)} = \frac{\pi}{2} \rho_0 \frac{N^2 k^2 m^2}{|c_{gz}| K^5} A_0^2 \int_0^\infty \mathcal{I}(\mu; \tilde{x}, \tilde{z}) d\mu,$$

where the integrand is given by

$$\mathcal{I}(\mu; \tilde{x}, \tilde{z}) = \frac{\mu e^{C_I |\tilde{x}|} \{ e^{-i[\mu \tilde{z} - C_R |\tilde{x}| - \Phi]} |\widehat{\mathcal{A}}|^2|_{\mathfrak{z}=C^*} + e^{i[\mu \tilde{z} - C_R |\tilde{x}| - \Phi]} |\widehat{\mathcal{A}}|^2|_{\mathfrak{z}=-C} \}}{[1 + \frac{1}{H_\rho^2 \mu^2}]^{1/4}},$$

in which C^* is the complex conjugate of $C(\mu)$. Finally, the expression for the induced flow field, $u^{(2)}(\tilde{x}, \tilde{z})$, follows immediately via the relation (2.13a). Explicitly,

$$u^{(2)} = -\frac{1}{\rho} \partial_{\tilde{z}} \Psi^{(2)} = \frac{i\pi}{2} \frac{N^2 k^2 m^2}{|c_{gz}| K^5} A_0^2 e^{z/H_\rho} \int_0^\infty \frac{\partial \mathcal{I}}{\partial \tilde{z}} d\mu, \quad (\text{A.11})$$

where the integrand is given by

$$\frac{\partial \mathcal{I}}{\partial \tilde{z}} = \frac{\mu^2 e^{C_I |\tilde{x}|} \{ e^{-i[\mu \tilde{z} - C_R |\tilde{x}| - \Phi]} |\widehat{\mathcal{A}}|^2|_{\mathfrak{z}=C^*} - e^{i[\mu \tilde{z} - C_R |\tilde{x}| - \Phi]} |\widehat{\mathcal{A}}|^2|_{\mathfrak{z}=-C} \}}{[1 + \frac{1}{H_\rho^2 \mu^2}]^{1/4}}.$$

A.2 Proof of Vanishing Arcs

We now prove that the integrals over the arcs defined by $\gamma_{\pm, \pm}$ in (A.9a) – (A.9d) vanish as $R \rightarrow \infty$, making use of the Jordan Lemma. The procedure is adapted from Churchill and Brown (1984, pp. 172–174). The convergence of eight separate integrals is reduced to the following two generalized cases, in which we assume $R > |\pm C(\mu)|$ can be chosen for any choice of $\mu \in \mathbb{R}$:

Case 1: The singularity $\mathfrak{z} + C(\mu) = 0$ is handled with $\Gamma_{+, \pm}$. In these cases, \pm corresponds to the sign of $\tilde{x} \neq 0$. Let $h_1(\mathfrak{z}; \mu) = e^{i\mathfrak{z}\tilde{x}} g_1(\mathfrak{z}; \mu)$. We have

$$\begin{aligned} \left| \int_{\gamma_{+, \pm}} h_1(\mathfrak{z}; \mu) d\mathfrak{z} \right| &\leq \int_0^\pi |g_1(Re^{\pm i\tau}; \mu) e^{iR\tilde{x}(\cos \tau \pm i \sin \tau)} (\pm i) Re^{\pm i\tau}| d\tau \\ &= R \int_0^\pi |g_1(Re^{\pm i\tau}; \mu)| e^{\mp R\tilde{x} \sin \tau} d\tau \\ &\leq RM \int_0^\pi e^{-R|\tilde{x}| \sin \tau} d\tau \\ &= 2RM \int_0^{\pi/2} e^{-R|\tilde{x}| \sin \tau} d\tau, \end{aligned}$$

where $M := \max_{\tau \in [0, \pi]} |g_1(Re^{\pm i\tau}; \mu)|$. The last equality holds by the symmetry $\sin \tau = \sin(\pi - \tau)$. Since $\sin \tau \geq 2\tau/\pi \forall \tau \in [0, \pi/2]$, it follows that

$$\begin{aligned} \left| \int_{\gamma_{+, \pm}} h_1(\mathfrak{z}; \mu) d\mathfrak{z} \right| &\leq \dots \leq 2RM \int_0^{\pi/2} e^{-2R|\tilde{x}|\tau/\pi} d\tau \\ &= \frac{2RM}{-2|\tilde{x}|R/\pi} e^{-2R|\tilde{x}|\tau/\pi} \Big|_0^{\pi/2} \\ &= \frac{\pi}{|\tilde{x}|} M (1 - e^{-R|\tilde{x}|}) \\ &\leq \frac{\pi}{|\tilde{x}|} M, \end{aligned}$$

where

$$M = \max_{\tau \in [0, \pi]} \left| \frac{\mathcal{A}}{Re^{\pm i\tau} + C(\mu)} \right| \leq \frac{|\mathcal{A}|}{R - |C(\mu)|} \rightarrow 0, \quad (\text{A.12})$$

as $R \rightarrow \infty$. In (A.12), we have denoted by $\mathcal{A} = \widehat{|\mathcal{A}|^2} \Big|_{Re^{\pm i\tau}}$ the Fourier transformed squared modulus of the amplitude function whose functional dependence on the variable \mathfrak{z} has been replaced by dependence on $Re^{\pm i\tau}$.

Case 2: The singularity $\mathfrak{z} - C(\mu) = 0$ is handled with $\Gamma_{-, \pm}$. In these cases, \pm corresponds to the sign of $-\tilde{x} \neq 0$. Let $h_2(\mathfrak{z}; \mu) = e^{i\mathfrak{z}\tilde{x}} g_2(\mathfrak{z}; \mu)$. We have

$$\begin{aligned} \left| \int_{\gamma_{-, \pm}} h_2(\mathfrak{z}; \mu) d\mathfrak{z} \right| &\leq \int_0^\pi |g_2(-Re^{\pm i\tau}; \mu) e^{-iR\tilde{x}(\cos \tau \pm i \sin \tau)} (\mp i) Re^{\pm i\tau}| d\tau \\ &= R \int_0^\pi |g_2(-Re^{\pm i\tau}; \mu)| e^{\pm R\tilde{x} \sin \tau} d\tau \\ &\leq RM \int_0^\pi e^{-R|\tilde{x}| \sin \tau} d\tau \\ &\leq \frac{\pi}{|\tilde{x}|} M, \end{aligned}$$

by an argument identical to that of case 1. Here,

$$\begin{aligned} M &:= \max_{\tau \in [0, \pi]} |g_2(-Re^{\pm i\tau}; \mu)| = \max_{\tau \in [0, \pi]} \left| \frac{\mathcal{A}}{-Re^{\pm i\tau} - C(\mu)} \right| = \max_{\tau \in [0, \pi]} \left| \frac{\mathcal{A}}{Re^{\pm i\tau} + C(\mu)} \right| \\ &\leq \frac{|\mathcal{A}|}{R - |C(\mu)|} \rightarrow 0, \end{aligned} \quad (\text{A.13})$$

as $R \rightarrow \infty$. In a similar manner as that shown in case 1, in (A.13) we have similarly let $\mathcal{A} = \widehat{|\mathcal{A}|^2} \Big|_{\mathfrak{z} = -Re^{\pm i\tau}}$. In taking the limits in (A.12) and (A.13), we have relied (somewhat heuristically) on the property that \mathcal{A} , and hence $\widehat{|\mathcal{A}|^2}$, are localized, becoming vanishingly small away from the wavepacket despite arbitrarily large R .

A.3 Example: Bivariate Gaussian Amplitude Function

As an example, suppose the wavepacket is a bivariate Gaussian whose initial vertical displacement amplitude is given by $\mathcal{A}(\tilde{x}, \tilde{z}) = e^{-(\tilde{x}^2/2\sigma_x + \tilde{z}^2/2\sigma_z)}$, in which σ_x and σ_z are the horizontal and vertical extents of the wavepacket, respectively. It is straightforward to explicitly evaluate (A.11). The Fourier transform of $|\mathcal{A}|^2$ is

$$\widehat{|\mathcal{A}|^2} = \frac{1}{4\pi} \sigma_x \sigma_z e^{-(\kappa^2 \sigma_x^2 + \mu^2 \sigma_z^2)/4}. \quad (\text{A.14})$$

Evaluating the right-hand side of (A.14) along $\mathfrak{z} = C^*(\mu)$ and $\mathfrak{z} = -C(\mu)$, respectively, gives

$$\widehat{|\mathcal{A}|^2} \Big|_{\mathfrak{z}=C^*(\mu)} = \frac{1}{4\pi} \sigma_x \sigma_z \exp \left\{ -\mu^2 \sigma_z^2/4 - (C_R^2 - C_I^2) \sigma_x^2/4 \right\} e^{iC_R C_I \sigma_x^2/2}, \quad (\text{A.15a})$$

$$\widehat{|\mathcal{A}|^2} \Big|_{\mathfrak{z}=-C(\mu)} = \frac{1}{4\pi} \sigma_x \sigma_z \exp \left\{ -\mu^2 \sigma_z^2/4 - (C_R^2 - C_I^2) \sigma_x^2/4 \right\} e^{-iC_R C_I \sigma_x^2/2}. \quad (\text{A.15b})$$

By inspection it is clear that $e^{-\mu^2 \sigma_z^2/4} < \infty \forall \mu \in \mathbb{R}$. It is likewise readily shown that $e^{-(C_R^2 - C_I^2) \sigma_x^2/4}$ remains bounded. Indeed,

$$C_R^2 - C_I^2 = \frac{k^2 m^2}{K^6} \left[\mu^8 + \frac{1}{H_\rho^2} \mu^6 \right]^{1/2} \cos(2\Phi) > 0,$$

because $\cos(2\Phi) > 0 \forall \Phi \in (-\pi/4, \pi/4)$. Substituting (A.15a,b) into (A.11) finally yields the explicit integral expression for the horizontal flow field induced by a horizontally and vertically localized wavepacket,

$$u^{(2)}(\tilde{x}, \tilde{z}) = \frac{1}{4} \frac{N^2 k^2 m^2}{|c_{gz}| K^5} A_0^2 \sigma_x \sigma_z e^{z/H_\rho} \int_0^\infty \frac{\partial \mathcal{I}}{\partial \tilde{z}}(\mu; \tilde{x}, \tilde{z}) d\mu, \quad (\text{A.16})$$

in which the integrand is given by

$$\frac{\partial \mathcal{I}}{\partial \tilde{z}} = \frac{\mu^2 e^{C_I |\tilde{x}|} e^{-[\mu^2 \sigma_z^2/4 + (C_R^2 - C_I^2) \sigma_x^2/4]} \sin(\mu \tilde{z} - C_R |\tilde{x}| - C_R C_I \sigma_x^2/2 - \Phi)}{\left[1 + \frac{1}{H_\rho^2 \mu^2} \right]^{1/4}} d\mu. \quad (\text{A.17})$$

When evaluating (A.16), it is necessary to choose the branch cut corresponding to outward- and downward-propagating long waves induced by the translating wavepacket (Bretherton, 1969), as was done in §3.2.4. In particular, Φ is deliberately re-defined using (3.12), which is reproduced here for reference:

$$\Phi = \pm \frac{1}{2} \tan^{-1}(1/H_\rho |\mu|).$$

The branch cut corresponding to the induced long waves we wish to capture is that for which the \pm sign in Φ is equal to $\text{sgn}(\mu)$. In implementing the choice of branch cut, we find it is also necessary to set $-C_R|\tilde{x}| \rightarrow C_R|\tilde{x}|$ in (A.17). The resulting expression for the induced flow field, $u^{(2)}(x, z, t)$, is found to be not uniformly valid in space, in agreement with the findings of previous studies of Boussinesq wavepackets (Bretherton, 1969; Tabaei and Akylas, 2007). However, we only require profiles of the induced mean flow through the centre of a translating wavepacket, which is found by setting $\tilde{x} = 0$ in (A.16) after taking the described branch cut. The resulting vertical profile of the wave-induced mean flow, $U(z, t) = u^{(2)}(\tilde{x} = 0, z, t)$, is found to be in excellent agreement with the results of the fast Fourier transform method described in §3.2.4.

Finally it is important to note that, although (A.11) is generally valid for all time up to the occurrence of wave overturning, (A.16) is valid only when an analytically tractable expression is known for the amplitude function. In the current example, the amplitude function is exactly known only at $t = 0$. For any $t > 0$, a wavepacket experiences weakly nonlinear effects to some degree, which alter its initial Gaussian structure. Therefore, in practice, the wave-induced mean flow is computed using the fast Fourier transform method detailed in §3.2.4.

Appendix B

Derivation of the Transition Vertical Wavenumber

Here, we derive the critical “transition vertical wavenumber”, \tilde{m}_* , using the approach of Sutherland (2010), which is based on the results of the variational method of Whitham (1974) for one-dimensional waves. Here, we apply Sutherland’s method for waves in two dimensions. For waves propagating in the x - z plane, the phase is given by $\varphi = kx + mz - \omega t$. From this we have

$$k = \frac{\partial \varphi}{\partial x}, \quad m = \frac{\partial \varphi}{\partial z}, \quad \omega = \frac{\partial \varphi}{\partial t}. \quad (\text{B.1a,b,c})$$

Dependence on φ is eliminated from (B.1a,b) by taking the time derivatives of (B.1a,b) and assuming mixed partial derivatives are equal, the results of which are the following advection equations for the horizontal and vertical wavenumber components:

$$\frac{\partial k}{\partial t} = -\frac{\partial \omega}{\partial x} = -c_{g_x} \frac{\partial k}{\partial x}; \quad (\text{B.2})$$

$$\frac{\partial m}{\partial t} = -\frac{\partial \omega}{\partial z} = -c_{g_z} \frac{\partial m}{\partial z}, \quad (\text{B.3})$$

where we have used the definitions of the horizontal and vertical group speeds, $c_{g_x} = \partial_k \omega$ and $c_{g_z} = \partial_m \omega$, respectively, given by (1.2b).

Separately we develop an equation for the evolution of the wave-induced mean flow, $U \propto |A|^2$. Adapting the argument of Sutherland (2010, c.f. sections 4.2.4, 2.2.6, and 3.4.2) for

small-amplitude one-dimensional waves to two dimensions

$$\frac{\partial U}{\partial t} = -\frac{\partial}{\partial x}(c_{g_x}U); \quad \frac{\partial U}{\partial t} = -\frac{\partial}{\partial z}(c_{g_z}U). \quad (\text{B.4a,b})$$

For finite amplitude waves, the left-hand sides of (B.2) and (B.3) are related to (B.4a,b) through the weakly nonlinear dispersion relation (Whitham, 1974; Sutherland, 2010) of the form

$$\omega \approx \omega_0(k, m) + U\omega_2(k, m), \quad (\text{B.5})$$

in which ω_2 is the real part of the coefficient on the nonlinear term in the nonlinear Schrödinger equation (2.54). Specifically, $\omega_2 = k$. Furthermore, we have explicitly used U in (B.5), rather than $|A|^2$ as was the case in the weakly nonlinear dispersion relations derived by Whitham (1974) and Sutherland (2010). Substituting (B.5) into the right-hand sides of (B.2), (B.3), and (B.4a,b), and retaining only the leading terms of the latter, we obtain two coupled matrix equations for k , m , and U :

$$\begin{aligned} \frac{\partial}{\partial t} \begin{pmatrix} k \\ U \end{pmatrix} &= - \begin{bmatrix} (\nabla_{\mathbf{k}}\omega_0) \cdot & \omega_2 \\ U(\partial_k \nabla_{\mathbf{k}}\omega_0) \cdot & \partial_k \omega_0 \end{bmatrix} \frac{\partial}{\partial x} \begin{pmatrix} \mathbf{k} \\ 0 \end{pmatrix}; \\ \frac{\partial}{\partial t} \begin{pmatrix} m \\ U \end{pmatrix} &= - \begin{bmatrix} (\nabla_{\mathbf{k}}\omega_0) \cdot & \omega_2 \\ U(\partial_m \nabla_{\mathbf{k}}\omega_0) \cdot & \partial_m \omega_0 \end{bmatrix} \frac{\partial}{\partial z} \begin{pmatrix} \mathbf{k} \\ U \end{pmatrix}, \end{aligned}$$

where $\nabla_{\mathbf{k}} = (\partial_k, \partial_m)$ and the matrices are understood to act as operators. These are readily uncoupled and simplified if we assume $k = k(x, t)$ and $m = m(z, t)$, the result of which is

$$\frac{\partial}{\partial t} \begin{pmatrix} k \\ U \end{pmatrix} = - \begin{bmatrix} \partial_k \omega_0 & \omega_2 \\ U \partial_{kk} \omega_0 & \partial_k \omega_0 \end{bmatrix} \frac{\partial}{\partial x} \begin{pmatrix} k \\ 0 \end{pmatrix}; \quad (\text{B.6})$$

$$\frac{\partial}{\partial t} \begin{pmatrix} m \\ U \end{pmatrix} = - \begin{bmatrix} \partial_m \omega_0 & \omega_2 \\ U \partial_{mm} \omega_0 & \partial_m \omega_0 \end{bmatrix} \frac{\partial}{\partial z} \begin{pmatrix} m \\ U \end{pmatrix}. \quad (\text{B.7})$$

The eigenvalues of (B.6) and (B.7) represent the leading-order correction to the horizontal

and vertical group speeds, respectively. Explicitly, the leading-order corrections are

$$c_{g_x}^A = c_{g_x} \pm \sqrt{U\omega_2\partial_{kk}\omega_0}; \quad (\text{B.8})$$

$$c_{g_z}^A = c_{g_z} \pm \sqrt{U\omega_2\partial_{mm}\omega_0}, \quad (\text{B.9})$$

in which we have adopted Sutherland's notation on the left-hand sides.

For assessing the modulational stability properties of the nonlinear Schrödinger equation (2.54), we consider the term under the square root of (B.9). If $U\partial_{mm}\omega > 0$, the wavepacket is prone to vertically broaden and decay in amplitude. Conversely, if $U\partial_{mm}\omega < 0$, the wavepacket is prone to narrow and grow in amplitude. Modulational instability in the vertical is more dynamically important than in the horizontal because atmospheric density decreases with height. The critical “transition vertical wavenumber”, \tilde{m}_* , separates the growth and decay regimes. By setting $Uk\partial_{mm}\omega = 0$ and rearranging the result, we find that

$$\tilde{m}_* = |m_*/k| := \frac{1}{\sqrt{2}} \left[1 + \frac{1}{4k^2 H_\rho^2} \right]^{1/2}. \quad (\text{B.10})$$

Hence we find that wavepackets with $|m/k| < \tilde{m}_*$ are prone to narrow and grow on their leading flank, whereas wavepackets with $|m/k| > \tilde{m}_*$ are prone to narrow and grow on their trailing flank.

Two-dimensional wavepackets also exhibit modulational instability in the horizontal. In this case the instability condition is $U\partial_{kk}\omega < 0$. Because $\partial_{kk}\omega < 0 \forall m \in \mathbb{R}$, the instability condition is satisfied where $U > 0$. In particular, this occurs on the leading flank of the wavepacket, hence we find that the leading flank of any two-dimensional wavepacket is prone to horizontal narrowing and amplitude growth, while its trailing flank is prone to horizontal spreading and relative amplitude decay. However, in most cases these effects are much less significant than the effects of vertical modulations.

Appendix C

Discretization of Partial Derivatives

In order to numerically integrate the nonlinear Schrödinger equation for horizontally and vertically localized internal gravity wavepackets, (2.54), centred finite difference schemes were developed to approximate each of the partial derivative terms. Here, we present the schemes for all such terms, including their associated error terms.

For indexing purposes, let $(x, z) = (x_1, x_2)$, $h_1 = \Delta x_1$ and $h_2 = \Delta x_2$. For an amplitude function at any fixed time step, denoted here by $A(x_1, x_2)$, let

$$A_{i\pm\alpha_1, j\pm\alpha_2} = A(x_1 \pm \alpha_1 h_1, x_2 \pm \alpha_2 h_2),$$

where $\alpha_1, \alpha_2 \in \mathbb{N}$. Terms such as $(\partial_x A)_{i,j}$, etc., are similarly defined, in which subscripts on ∂ denote partial derivatives with respect to that variable in the original (x, z) notation.

To approximate pure and mixed partial derivatives of up to third-order in x_1 and x_2 , while maintaining $O(h_1^2, h_2^2)$ accuracy, we take linear combinations of the two-variable Taylor expansion truncated at fifth-order, given by

$$A(x_1 \pm \alpha_1 h_1, x_2 \pm \alpha_2 h_2) \approx \sum_{q=0}^5 \left[\frac{1}{q!} \sum_{\ell_1=1}^2 \cdots \sum_{\ell_q=1}^2 \frac{\partial^q A(x_1, x_2)}{\partial x_{\ell_1} \cdots \partial x_{\ell_q}} (\pm \alpha_{\ell_1} h_{\ell_1}) \cdots (\pm \alpha_{\ell_q} h_{\ell_q}) \right],$$

assuming the equality of mixed partial derivatives of any particular order.

Henceforth using the usual method of linear combinations of Taylor series, the advection terms, including their respective leading-order error terms, are approximated as

$$(\partial_x A)_{i,j} = \frac{1}{2h_1} [A_{i+1,j} - A_{i-1,j}] + \frac{1}{6} h_1^2 \partial_{xxx} A(\xi, z); \quad (\text{C.1a})$$

$$(\partial_z A)_{i,j} = \frac{1}{2h_2} [A_{i,j+1} - A_{i,j-1}] + \frac{1}{6} h_2^2 \partial_{zzz} A(x, \eta), \quad (\text{C.1b})$$

where $\xi \in (x - h_1, x + h_1)$ and $\eta \in (z - h_2, z + h_2)$.

The leading-order linear dispersion terms, including their respective leading-order error terms, are approximated as

$$(\partial_{xx} A)_{i,j} = \frac{1}{h_1^2} [A_{i+1,j} - 2A_{i,j} + A_{i-1,j}] + \frac{1}{12} h_1^2 \partial_{xxxx} A(\xi, z); \quad (\text{C.2a})$$

$$(\partial_{zz} A)_{i,j} = \frac{1}{h_2^2} [A_{i,j+1} - 2A_{i,j} + A_{i,j-1}] + \frac{1}{12} h_2^2 \partial_{zzzz} A(x, \eta), \quad (\text{C.2b})$$

where $\xi \in (x - h_1, x + h_1)$ and $\eta \in (z - h_2, z + h_2)$. Similarly, the leading-order oblique dispersion term and its leading-order error term is approximated as

$$\begin{aligned} (\partial_{xz} A)_{i,j} &= \frac{1}{4h_1 h_2} [A_{i+1,j+1} - A_{i+1,j-1} - A_{i-1,j+1} + A_{i-1,j-1}] \\ &\quad + \frac{1}{6} [h_1^2 \partial_{xxxz} A(\xi_1, \eta_1) + h_2^2 \partial_{xzzz} A(\xi_2, \eta_2)], \end{aligned} \quad (\text{C.3})$$

where $\xi_1, \xi_2 \in (x - h_1, x + h_1)$ and $\eta_1, \eta_2 \in (z - h_2, z + h_2)$.

The pure second-order linear dispersion terms, including their leading-order error terms, are approximated as

$$(\partial_{xxx} A)_{i,j} = \frac{1}{2h_1^3} [A_{i+2,j} - 2(A_{i+1,j} - A_{i-1,j}) - A_{i-2,j}] + \frac{1}{4} h_1^2 \partial_{xxxxx} A(\xi, z); \quad (\text{C.4a})$$

$$(\partial_{zzz} A)_{i,j} = \frac{1}{2h_2^3} [A_{i,j+2} - 2(A_{i,j+1} - A_{i,j-1}) - A_{i,j-2}] + \frac{1}{4} h_2^2 \partial_{zzzzz} A(x, \eta), \quad (\text{C.4b})$$

where $\xi \in (x - 2h_1, x + 2h_1)$ and $\eta \in (z - 2h_2, z + 2h_2)$. Similarly, the second-order oblique dispersion terms, including their respective leading-order error terms, are approximated as

$$\begin{aligned} (\partial_{xxz} A)_{i,j} &= \frac{1}{2h_1^2 h_2} [A_{i+1,j+1} - A_{i+1,j-1} - 2(A_{i,j+1} - A_{i,j-1}) + A_{i-1,j+1} - A_{i-1,j-1}] \\ &\quad + \frac{1}{3} \left[\frac{1}{2} h_1^2 \partial_{xxxz} A(\xi_1, \eta_1) + h_2^2 \partial_{xzzz} A(\xi_2, \eta_2) \right]; \end{aligned} \quad (\text{C.5a})$$

$$\begin{aligned} (\partial_{xzz} A)_{i,j} &= \frac{1}{2h_1 h_2^2} [A_{i+1,j+1} - A_{i-1,j+1} - 2(A_{i+1,j} - A_{i-1,j}) + A_{i+1,j-1} - A_{i-1,j-1}] \\ &\quad + \frac{1}{3} \left[h_1^2 \partial_{xxxz} A(\xi_1, \eta_1) + \frac{1}{2} h_2^2 \partial_{xzzz} A(\xi_2, \eta_2) \right], \end{aligned} \quad (\text{C.5b})$$

where $\xi_1, \xi_2 \in (x - h_1, x + h_1)$ and $\eta_1, \eta_2 \in (z - h_2, z + h_2)$.

It is worth noting that, in general, partial derivatives do not have unique finite difference approximations. In particular, it is possible to derive second-order accurate centred difference

approximations of the pure second- and third-order partial derivatives of A by composing a first-order difference equation with itself once (for the pure second-order derivative approximations) or twice (for the pure third-order derivative approximations). While the arithmetic involved in this method is simpler, it does not provide the leading-order error terms.

Without loss of generality, as an example we consider the second- and third-order partial derivatives with respect to x , derived using the described method of composition. This approach yields an identical expression for the second-order derivative approximation, however the third-order derivative approximation is

$$(\partial_{xxx}A)_{i,j} = \frac{1}{8h_1^3} \left[A_{i+3,j} - 3(A_{i+1,j} - A_{i-1,j}) - A_{i-3,j} \right]. \quad (\text{C.6})$$

This scheme can alternatively be derived using the method of linear combinations of Taylor series, which reveals that its leading-order error term is

$$\frac{1}{2}h_1^2\partial_{xxxx}A(\xi, z),$$

where $\xi \in (x - 3h_1, x + 3h_1)$. While both schemes (C.4a) and (C.6) possess the desired property of consistency, we immediately note that the error term for scheme (C.6) is twice as large as that of scheme (C.4a), for a given fixed ξ and z . Moreover, the maximum truncation error associated with scheme (C.6) is potentially larger than that associated with scheme (C.4a) due to the larger domain $(x - 3h_1, x + 3h_1)$ from which the maximizing value of ξ may be drawn.

The insight provided by this analysis has immediate consequences on our choice of numerical methods: the weakly nonlinear code used by Dosser (2010) to numerically integrate the nonlinear Schrödinger equation for horizontally periodic anelastic internal gravity waves employed the z -equivalent of scheme (C.6) to approximate the third-order derivative with respect to z . Because the weakly nonlinear code used for this thesis is adapted from that of Dosser, it was re-written to employ scheme (C.4a) and its z -equivalent to approximate the pure third-order derivatives.